Methodical and Applied Research

INSTRUMENT BASE OF SYSTEMS FOR DIAGNOSTICS AND TRANSPORTATION OF PROTON AND NEUTRON BEAMS FOR RADIATION TESTING OF ELECTRONICS AT THE 1 GeV SYNCHROCYCLOTRON OF PNPI

D.A. Amerkanov, S.A. Artamonov, A.S. Vorobyov, G.I. Gorkin, E.M. Ivanov, S.V. Kosyanenko, O.V. Lobanov, V.G. Muratov, V.V. Pashuk, O.A. Shcherbakov, V.A. Tonkikh;
V.S. Anashin, A.E. Kozyukov, P.A. Chubunov – United Rocket and Space Corporation –
Scientific Research Institute of Space Instrumentation, Moscow

1. Introduction

The widespread use of semiconductor products of microelectronics as an element base of space electronic systems has made the problem of assessing and predicting the levels of failures of elements and assemblies to the radiation effects of outer space relevant. The requirements for these tests are due to the fact that in modern devices manufactured using micron and submicron technologies, new effects of radiation exposure have arisen associated with ionization effects and structural damage to products under the action of individual high-energy particles, the so-called single radiation effects, or single event effects.

Over the past 20 years, failures and breakdowns under the action of individual protons and neutrons have been studied at PNPI in the operation of various highly integrated products: memory elements, transistors, charge coupled devices (CCD) matrices. In this direction, PNPI actively cooperates with many organizations and enterprises in Russia.

Below is given a description of the instrumental base of the systems for diagnostics and transportation of proton and neutron beams, which are part of the stands for radiation tests, developed at PNPI in cooperation with the Institute of Space Instrumentation (Roscosmos), a branch of the United Rocket and Space Corporation [1].

2. Transportation system

The transportation system ensures the delivery of the proton beam from the output window of the accelerator to the workstations. The transportation system includes:

- Dispensing magnet SP-40 – for output to the required path;
- Correction magnets – to shift the proton beam vertically and horizontally;
- Collimators – to change the beam emittance;
- Magnetic lenses – for focusing and defocusing the proton beam;
- Absorber of variable thickness (0–530 mm) – for changing the beam energy in the range of 60–1 000 MeV [2].

The diagram of the proton beam transportation paths to the irradiation workstations is shown in Fig. 1.

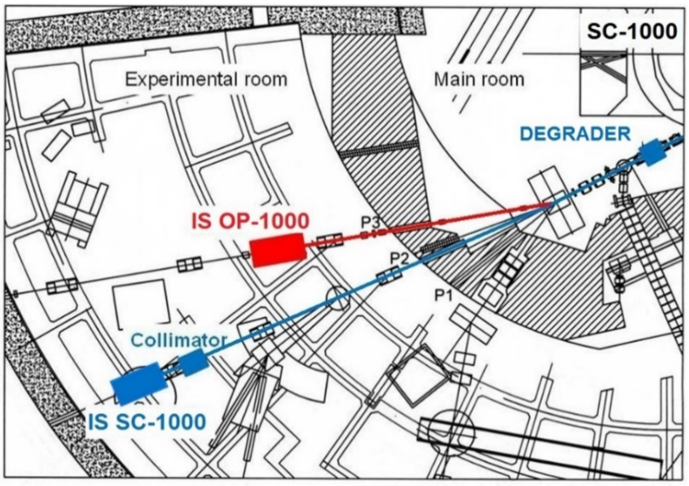

Fig. 1. Diagram of proton beam transport paths: P2 – protons with an energy of 1 000 MeV; P3 – protons with a variable energy of 60–1 000 MeV

The automated control system for setting and stabilizing the current in the magnetic elements is responsible for regulating the current in the magnets (Fig. 2). For output to the working path, an appropriate magnetic field is installed in the distributing magnet SP-40, which is located at the output wall of the "Main Hall".

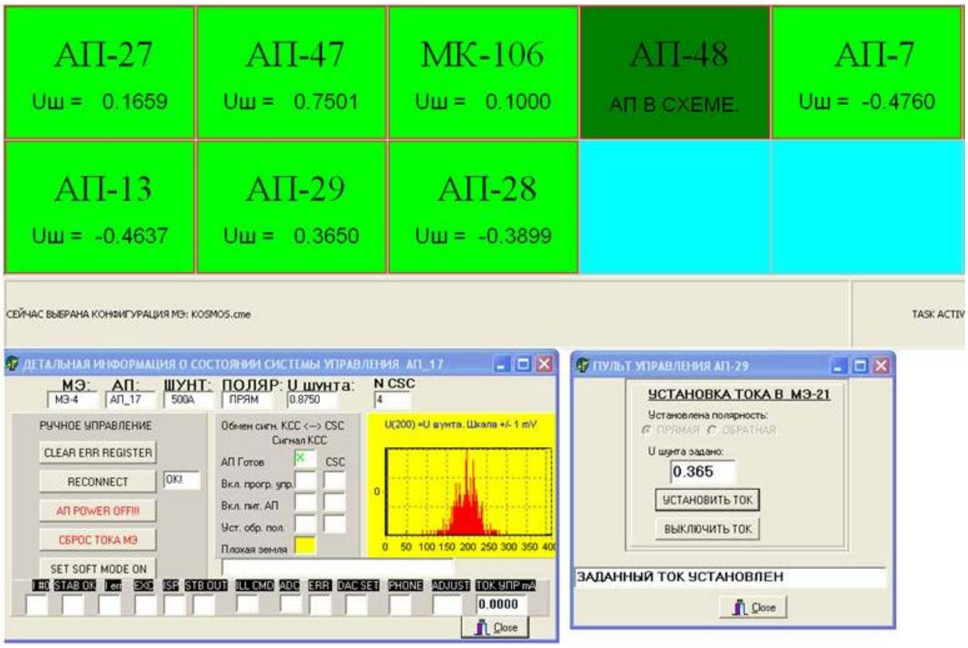
АП-27 Uш = 0.1659
АП-47 Uш = 0.7501
МК-106 Uш = 0.1000
АП-48 АП В СХЕМЕ
АП-7 Uш = -0.4760
АП-13 Uш = -0.4637
АП-29 Uш = 0.3650
АП-28 Uш = -0.3899

СЕЙЧАС ВЫБРАНА КОНФИГУРАЦИЯ МЭ: KOSMOS.cme

МЭ: МЭ-4
АП: АП_17
ШУНТ: 500A
ПОЛЯР: ПРЯМ
U шунта: 0.8750
N CSC: 4
ТОК УПР mA: 0.0000

U шунта задано: 0.365

ЗАДАННЫЙ ТОК УСТАНОВЛЕН

Fig. 2. Interface of the automated control system of the current in the magnetic elements

The fields in the main magnet E-9 of the synchrocyclotron and in the distributing magnet SP-40 are set and controlled by nuclear magnetic resonance (NMR) magnetometers, which makes it possible to reproduce the beam output with good accuracy (Fig. 3).

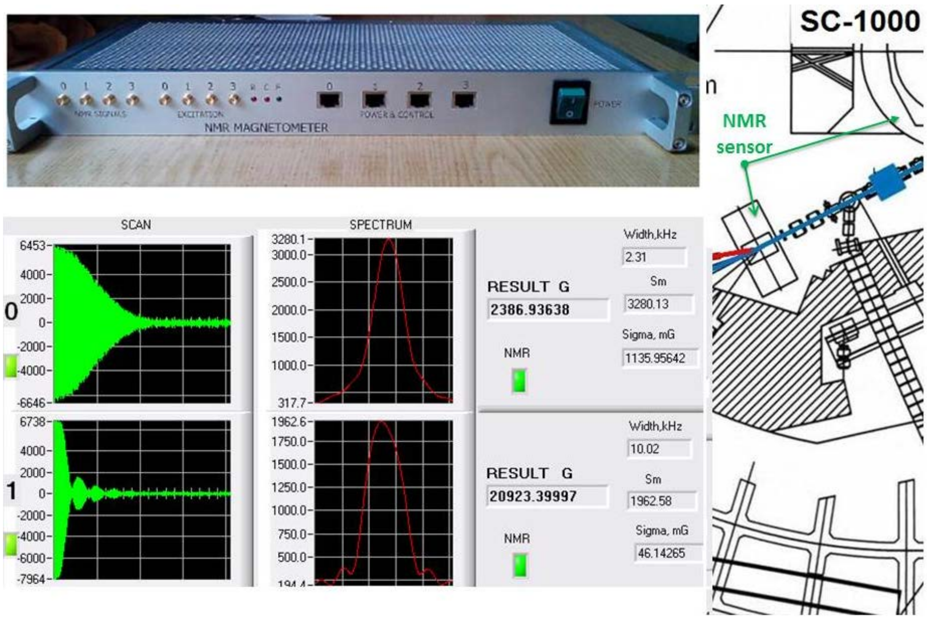
0: RESULT G 2386.93638; Width,kHz 2.31; Sm 3280.13; Sigma, mG 1135.95642

1: RESULT G 20923.39997; Width,kHz 10.02; Sm 1962.58; Sigma, mG 46.14265

Fig. 3. Nuclear magnetic resonance magnetometer, its interface and location

The variable thickness absorber allows remote adjustment of the absorber thickness by placing a set of copper cylinders in the beam path (Fig. 4).

Fig. 4. The variable thickness absorber

3. Diagnostic system

The diagnostic system provides control of beam parameters and consists of the following tools:

- Two-channel semiconductor profilometer to determine the width of the beam and its centre of gravity;
- Scintillation profilometer with CCD-matrix – to obtain a proton beam profile with a resolution of 512 × 512 points;
- Two-section ionization chamber for online monitoring of the intensity of the proton flux [3];
- Fission ionization chamber to determine the intensity of the neutron flux;
- Two-axis position-sensitive multiwire proportional counter to obtain the distribution of neutrons in the beam.

A two-section ionization chamber design is shown in Fig. 5.

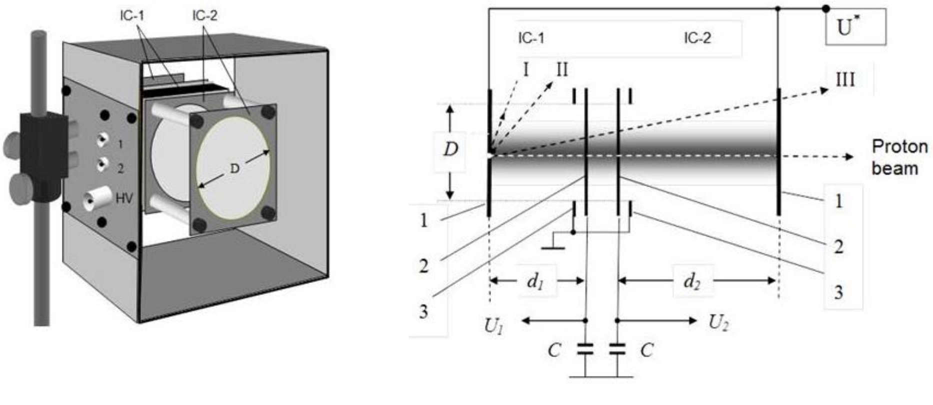

Effective range
$10^6 – 10^9$ p·sec^{-1}

1. High-voltage electrodes
2. Signal electrodes
3. Aperture electrodes

U* – High-voltage source

Fig. 5. Two-section ionization chamber design

The results of measuring the beam width and particle distribution density are shown in Fig. 6.

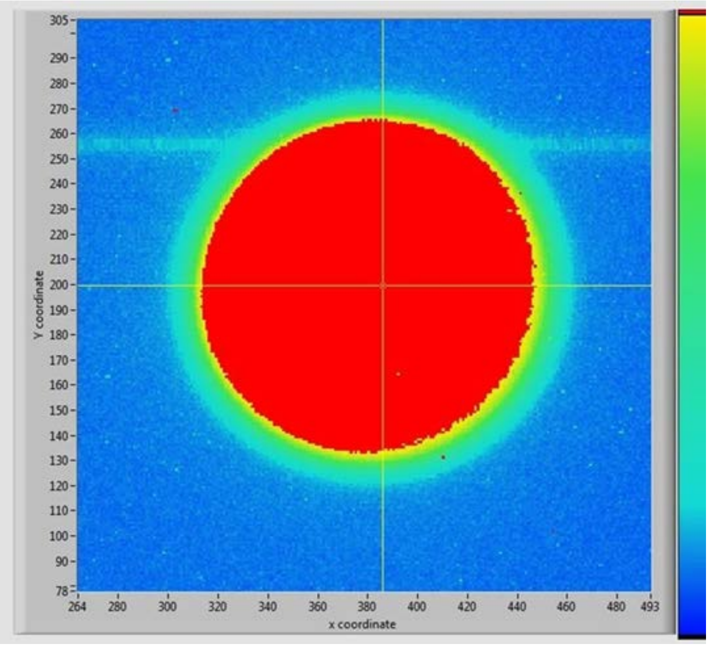

Fig. 6. The result of the work of a scintillation profilometer with a CCD-matrix to find the particle distribution density in the beam

4. Conclusion

The PNPI centre is equipped with all necessary systems of beams diagnostics and transportation to a target. These systems allow changing the shape, energy and direction of the proton beam, as well as measuring the profile and intensity of proton and neutron beams. There is also an instrument to vary the temperature of exemplars in a wide range.

The combination of these systems provides the necessary beam parameters for testing electronic components in proton beams with a variable energy of 60–1 000 MeV and in an atmospheric neutron beam with a wide energy range (1–1 000 MeV).

References

1. D.A. Amerkanov, S.A. Artamonov, E.M. Ivanov *et al.*, in *XXV Rus. Conf. on Particle Accelerators RUPAC 2016*, THCAMH01 Report, 105 (2016).
2. E.M. Ivanov, G.F. Mikheev, V.S. Anashin, An Automated Moderator of the Proton Beam of the Synchrocyclotron – a Degrader: Utility Model Patent No. 181147; Priority 03.30.2018.
3. D.A. Amerkanov, G.I. Gorkin, E.M. Ivanov *et al.*, PTE **3**, 11 (2016).

ABSOLUTE PROTON BEAM MONITOR BASED ON AN IONIZATION CHAMBER WITH A TRANSVERSE ELECTRIC FIELD

D.A. Amerkanov, E.M. Ivanov, N.A. Ivanov, O.V. Lobanov, V.V. Pashuk

1. Introduction

The physical properties of an absolute proton beam monitor operating in real time are investigated. The monitor detector consists of two air-filled ionization chambers (IC) combined into one module with a transverse electric field relative to the beam path. In the chambers, the signal electrodes have different lengths along the beam. High-voltage electrodes are located from the signal electrodes at a distance equal to or proportional to the length of the signal electrode. The ability to vary the length of the electrode allows one to quickly change the measured range of the proton fluxes.

2. Ionization chamber with a transverse electric field

When conducting radiation research at the PNPI synchrocyclotron, absolute monitors are used based on a plane-parallel dual-section ionization chamber (DIC) [1, 2] through which a beam of protons with energies of 50–1 000 MeV passes perpendicular to electrodes made of thin aluminium foils (10–20 μm). In order to expand the measured range towards higher values of proton fluxes, in this paper, we considered an ionization chamber monitor with a transverse electric field relative to the beam direction and, consequently, with no foils in the beam path, but designed in such a way as to preserve the method for determining the quantitative characteristics of the flux and the total number of protons, previously developed for the DIC monitor.

A beam detector with a transverse electric field relative to the beam path [3] consists of two ICs combined into one module with plane-parallel high-voltage and signal electrodes. The chambers differ in the lengths of the signal electrodes and are arranged in series along the beam path. In each IC, the distances between the high-voltage and signal electrodes are different in magnitude, and the lengths of the signal electrodes along the beam direction are equal or proportional to the inter-electrode distances of the corresponding ICs. Equal-rated capacitors are connected to each signal electrode, which are charged by induction currents of external circuits equal to the ion currents of the chambers. The number of protons passing through these chambers is calculated from the voltage measured simultaneously on the capacitors using a developed algorithm [1]. A technical drawing of a dual-chamber ionization detector (DID) is shown in the Figure.

The number of ion pairs n', formed by N beam protons passing in the inter-electrode space IC_1 and IC_2 during the integration time T is

$$n'_{1(2)} = N\left[-\frac{dE}{dx}\right] L_{1(2)}\omega^{-1}, \qquad (1)$$

where $[-dE/dx]$ is the specific ionization loss of a proton in air at normal pressure; $L_{1(2)}$ is the total length of the electrode ($L'' + L'$); ω is the energy spent by the proton on the formation of one pair of ions.

If $\left[\frac{L_{1(2)}}{d_{1(2)}}\right] = k$, then

$$n_{1(2)} = N\left[-\frac{dE}{dx}\right] d_{1(2)} k\omega^{-1}\lambda_{1(2)}. \qquad (2)$$

The voltage $U_{C1(2)}$ on the capacitor $C_{1(2)}$ in the signal electrode circuit of each IC with inter-electrode distance $d_{1(2)}$ is equal to

$$U_{C1(2)} = \frac{n_{1(2)}e}{C}. \qquad (3)$$

The number N of beam protons passing through the chambers can be determined as

$$N = \frac{U_{C1(2)}C}{\left[-\frac{dE}{dx}\right] d_{1(2)} ke\omega^{-1}\lambda_{1(2)}}. \qquad (4)$$

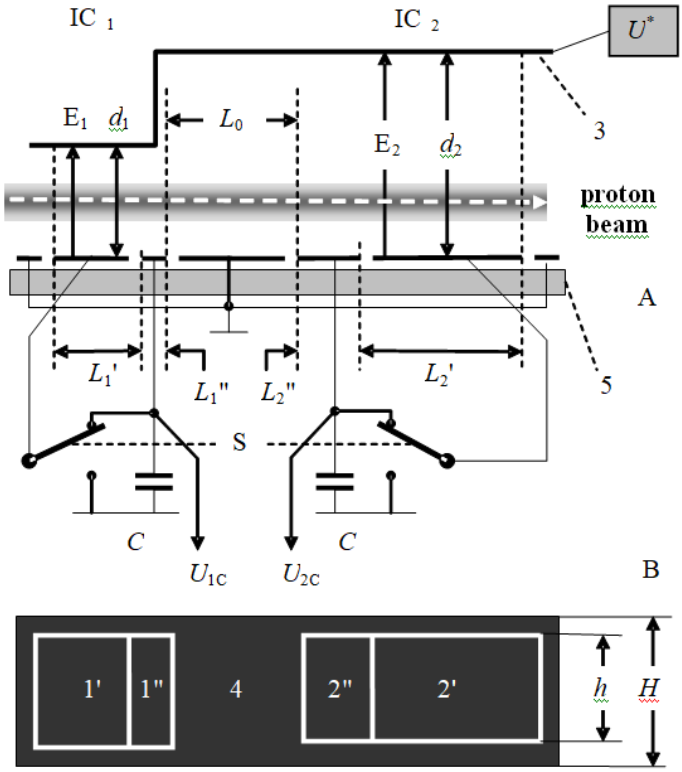

Technical drawing of a dual-chamber ionization detector: *A* – frontal projection; *B* – top view of the board with the signal electrodes. IC_1 and IC_2 – the first and second ionization chambers; 1', 1" – signal electrodes of length L_1', L_1'' along the path of the beam in IC_1; 2′, 2″ – signal electrodes of length L_2', L_2'' along the path of the beam in IC_2; *3* – high voltage electrode; *4* – grounded electrode; *5* – printed circuit board with electrodes; d_1 and d_2 are the inter-electrode distances between the signal and high voltage electrodes in IC_1 and IC_2, respectively; E_1 and E_2 are the electric field strength vectors in IC_1 and IC_2; L_0 is the distance between the signal electrodes; U_{1C} and U_{2C} – the measured voltages on capacitors *C*; *S* – the key for switching the proton flux measurement range; *h* – width of the signal electrodes; *H* – width of the panel with signal electrodes

3. Results and conclusion

The operation of a DID with a transverse electric field with respect to the beam path and the principles for calculating the absolute value of the number of particles in a beam were tested at the PNPI synchrocyclotron using a collimated proton beam. It was shown that the experimental values of the proton flux measured using a two-chamber ionization detector and using a two-section ionization chamber at a constant current of a relative monitor located in the main hall of the accelerator coincide within 10%. Note that there are no physical restrictions for measuring large flows. By changing the length of the signal electrodes, as well as changing the capacitance of the capacitors and the integration time, it is possible to measure the proton flux over a wide range during the experiment.

An ionization detector of this design can be used in heavy particle accelerators, where the problems of correct measurements of fluxes are necessary and important, as well as in the cases where beam broadening is unacceptable (for example, in proton therapy, ophthalmology).

References

1. N.A. Ivanov, O.V. Lobanov, V.V. Pashuk, PTE **6**, 5 (2009).
2. D.A. Amerkanov, G.I. Gorkin, E.M. Ivanov *et al.*, PTE **3**, 11 (2016).
3. N.A. Ivanov, O.V. Lobanov, V.V. Pashuk, Two-Chamber Ionization Detector, Message No. 3012, 12 (2017).

IMPORTANT FOCUSING PROPERTIES OF THE MAGNETIC STRUCTURE OF ISOCHRONOUS CYCLOTRONS WITH HIGH SPIRALING ANGLE OF THE POLE TIPS

D.A. Amerkanov, S.A. Artamonov, E.M. Ivanov, G.A. Riabov, V.A. Tonkikh

1. Introduction

Magnetic structures with a large spirality angle of pole tips were investigated in a number of works and are used in superconducting cyclotrons, H^- ion cyclotrons, *etc*. With the design and construction of an 80 MeV isochronous H^- cyclotron, such studies were continued and extended. In this work, a relatively simple approach for analysing the spiral structure is proposed.

The magnetic structure with a large spirality angle of the pole tips is used in cases when vertical focusing from the flutter (field difference in the valley and the sector) is insufficient and it is necessary to add the angle focusing. This situation is typical for superconducting cyclotrons and for cyclotrons that accelerate negative hydrogen ions. Moreover, at Joint Institute for Nuclear Research (JINR) in Dubna, such structures were investigated and a cyclotron and a synchrocyclotron with sectors in the form of an Archimedes spiral with a maximum spirality angle of up to 70 degrees were built. Numerical calculations of the magnetic field for an isochronous superconducting cyclotron with spiral sectors in the approximation of their uniform magnetization were carried out [1].

Two effects were noted: a decrease in the flutter in the central region with the introduction of spirality and a mismatch between the spirality of the sector iron and the magnetic field. However, calculations made for a specific geometry are not applicable in the case of a different design. With the construction of an isochronous cyclotron for accelerating H^- ions up to 40–80 MeV [2, 3], studies of the focusing properties of spiral structures were continued and expanded. Modern 3*D* software codes simplify the design of the magnetic field of any configuration by using trial and error. However, to speed up the procedure and to reduce the number of options for a 3*D* analysis, it is useful to first perform a simplified and visual analysis of the system and estimate the importance of various parameters in the framework of a simpler 2*D* approximation.

2. Development of two-dimensional approximation

2.1. Optimization of the magnet gaps

As a first approximation, the hill ($2g_h$) and valley ($2g_v$) gaps for each fixed sector thickness (h_s) were selected using 2*D* POISCR calculations based on the proposed new fill factor method. In this method, a 3*D* problem is reduced to a 2*D* one. The iron rings or the so-called shims mounted on the magnet poles and providing an isochronous rise in the field are calculated using a 2*D* program with a reduced value of the magnetic permeability $\mu_{\text{new}}(B) = \mu(B) \cdot C$. The permeability is reduced by a factor $C(r)$ – the so-called filling factor equal to the ratio of the azimuthal length of the sector to the length of the periodicity element at each radius *r*. The gap of the magnet obtained in this way corresponds to the gap of the hill, and there is no additional shim in the valley. Thus, two variants of the gaps of the main magnet and the gaps of the hills and the valleys were analysed. The parameters of these variants are presented in the caption to Fig. 1.

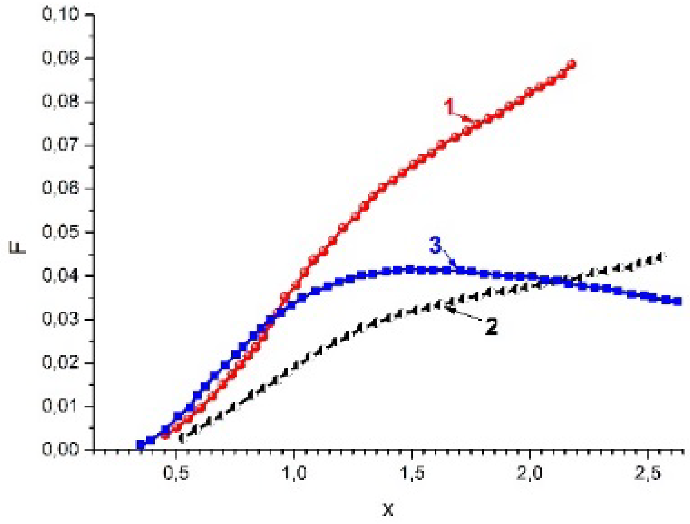

Fig. 1. The dependence of the flutter on the dimensionless parameter $x = r / N \cdot g_h$, where $N = 4$, for two options: *1* – $2g_v = 386$ mm, $2g_h = 170$ mm, $h_s = 108$ mm; *2* – $2g_v = 284$ mm, $2g_h = 145$ mm, $h_s = 69$ mm; *3* – a variant of uniform magnetization for the case of the geometry of the first variant

2.2. Flutter problem

The azimuthal variation of the magnetic field [1] is determined by the so-called flutter $F(r)$:

$$F(r) = <(B - <B>)^2> / <B>^2, \quad <\ldots> = (2\pi)^{-1}\int_0^{2\pi}\ldots d\theta.$$

The flutter can be represented as a Fourier harmonics expansion of the azimuthal variation of the magnetic field. The fundamental contribution to the expansion is made by the general focusing harmonic associated with the number of sectors and periodicity elements (in our case, $N = 4$). If we denote the value of the fundamental focusing harmonic $f = B_N / <B>$, then $F = f^2/2$.

An analytical calculation of the flutter is a complex and practically impossible problem, therefore, approximate methods were used. In particular, in Ref. [4], an expression was obtained for the general harmonic of the magnetic field variation in an isochronous cyclotron in the approximation of uniform magnetization of the sectors of the magnet,

$$B_N = 8M \sin(2\pi a/d) \exp(-2\pi g_h/d),$$

where $2a$ is the length of the sector along the azimuth for a given radius r; $2g_h$ is the gap in the hill; d is the period of the structure, equal to the total length of the hill and valley, $4\pi M = 21$ kG. It follows from this expression that for an isochronous cyclotron with a period of the magnetic field structure equal to $d = 2\pi r / N$, where N is the number of sectors, the flutter grows with increasing radius according to the law

$$F \sim \frac{B_N^2}{2} \sim \exp(-2/x), \quad x = r/N \cdot g_h. \tag{1}$$

Although this approximation is insufficient for obtaining accurate quantitative estimates, it allows, in a unified manner, to get an idea of the relationship between different parameters of the magnetic structure. Moreover, the introduction of the dimensionless parameter x enables the comparison of different variants of the structures. In particular, the flutter rises as the gap in the hill decreases and falls as the number of sectors increases.

The maximum flutter value corresponds to the case when the azimuthal extent of the sector and the valley are equal. In this case, $a = 0.25d$ and $\sin(\pi/2) = 1$. For the case when the parameter x becomes less than 0.5, the flutter drops very sharply, *i. e.*, at radii $r \leq 0.5Ng_h$, the azimuthal variation becomes ineffective, and focusing tends to zero. The results of these calculations are shown with curve *3* in Fig. 1.

The dependence of the flutter on the radius can be calculated using 3*D* programs. However, they are usually a commercial product. Therefore, in our case, to speed up and simplify the calculations, we used 2*D* approximate calculations. The flutter can be estimated using a 2*D* program if we replace the calculation of the edge effect along the azimuth with the calculation of the edge effect along the radius of the two-dimensional magnet with a gap in the form of teeth and valleys along the radius. In this case, the gap variation of a 2*D*-

magnet along the radius corresponds to the length and gaps of the sector and valley along the azimuth of the investigated 3*D* magnet.

Simple estimates carried out for the C-80 cyclotron show that the structure with straight sectors does not provide the necessary vertical focusing; therefore, it is necessary to use the following effect.

2.3. Influence of the spirality effect

As it is well known, the frequency of vertical oscillations, which determines the vertical focusing, can be expressed using the following approximation:

$$\nu_z^2 \approx -k + F \cdot S(r,\gamma), \quad S(r,\gamma) = 1 + 2tg^2\gamma, \tag{2}$$

where k is the rate index of the average magnetic field growth along the radius,

$$k = \left(\frac{r}{< B >}\right)\left(\frac{d < B >}{dr}\right) \approx \frac{2W}{E_0}.$$

Here W is the kinetic energy, E_0 = 938 MeV is the rest mass of the proton, γ is the spirality angle. The frequency of axial oscillations is determined by two oppositely acting terms – the defocusing of the isochronous rise of the mean field and the focusing action of the azimuthal variation of the field. The task is to select F and γ for each value of the energy W so that ν_z^2 remains greater than zero during acceleration. At the same time, to limit the dissociation of negative ions, it is necessary to strive for the lowest possible value of the magnetic field in the hill, *i. e.* to the minimum flutter value. The spiraling sector provides an increase in focusing force due to the non-perpendicular angle of particle entry into the sector region. Effectively, the flutter F is multiplied by the coefficient $S\ (r,\gamma)$; however, in a structure with a large spirality angle, the increase in focusing force is noticeably less [1] than could be expected from the above formula. This is due to a decrease of the flutter when the spirality angle is introduced and a mismatch between the iron and the magnetic spirality angles.

There is a simple geometric explanation for the first effect. With a large spirality angle, the difference between the sector length along the azimuth (*AB* in Fig. 2) and the width of the A_1B_1 sector determined from geometric considerations, becomes significant. In the case of straight sectors, the flutter is determined by the magnetic field difference in the hill and the valley. In this case, the field falls off along the azimuth. When a spiraling angle is introduced, the distance between the sectors along a line perpendicular to the centre-line of the sector is much smaller than the distance along the azimuth. This leads to a decrease in the effective length of the sector A_1B_1 and, accordingly, to a decrease in the length of the valley. From geometric considerations, we can conclude that the effective length of the A_1B_1 sector is approximately equal to the length of the sector along the azimuth *AB* multiplied by a factor equal to cosγ, *i. e.* $A_1B_1 \approx AB\cos\gamma$. With a decrease in the length of the sector, the effective length of the valley and the period of periodicity decrease. In this case, the dimensionless parameter x, introduced in expression (1) and related to the length of the periodicity period, will also decrease and becomes $x_{\text{eff}} = x\cos\gamma$. According to Fig. 1, a decrease in the value of the parameter $x_{\text{eff}} = x\cos\gamma$ leads to a shift along the graph towards lower flutter values. At intermediate and large radii, the spirality causes an increase in the edge focusing and a decrease in the flutter, and the total effect leads to an overall increase in focusing. However, at small radii, the introduction of spiraling reduces the effective sector length and this can lead to a very sharp drop in the flutter and a total decrease in focusing. The total effect of the introduction of the spiral sectors can be characterized by a parameter that is the product of two factors: the flutter F and $S\ (r,\gamma)$. Since the flutter drops sharply at $x_{\text{eff}} < 0.5$, the introduction of spiraling in the central region leads to a decrease in focusing. For each radius, it is possible to calculate the limiting value of the spiraling angle, exceeding which spiraling does not give an increase in focusing. This value for each parameter x can be estimated by finding the solution for the following equation:

$$U(x,\gamma) = (F(x\cos\gamma)/F(x)) \cdot (1 + 2\text{tg}^2\gamma) - 1 = 0, \tag{3}$$

where $F(x)$ is a function of the type shown in Fig. 1.

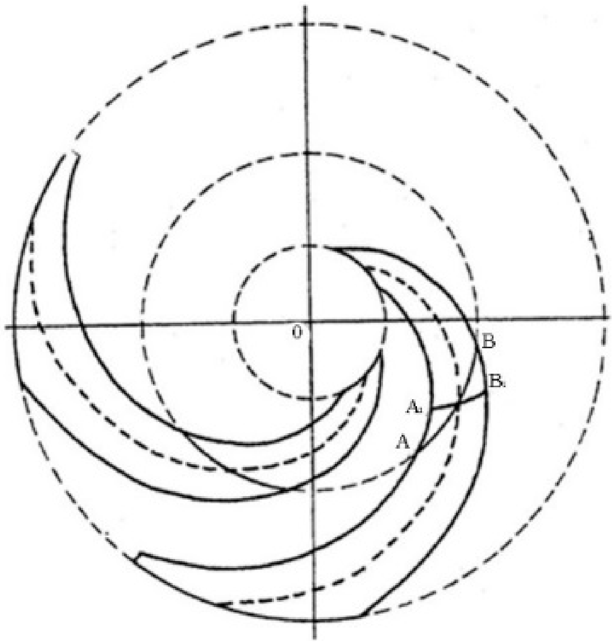

Fig. 2. There is a difference between the sector length along the azimuth *AB* and the “effective” length A_1B_1 at large spiraling angles. The effective sector width corresponding to its average line for a given r is equal to $A_1B_1 \approx AB\cos\gamma$

Figure 3 shows the limiting spiraling angle calculated by formula (3) as a function of the radius for the case of the C-80 cyclotron. According to Fig. 3, spiraling leads to decreasing of vertical focusing at radii smaller than 35 cm, and it is advisable to use a structure with a large spirality angle at radii greater than 35 cm. Thus, a structure with a large spiraling angle is effective only at radii larger that the hill gap value.

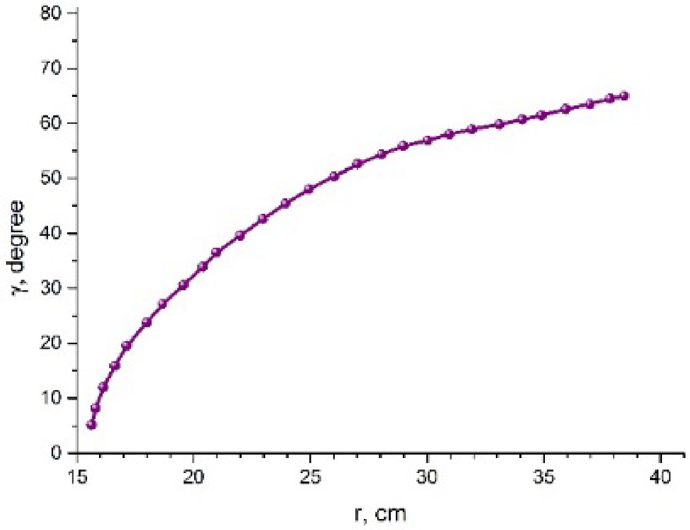

Fig. 3. Ultimate spirality angle for C-80 cyclotron in dependence on the radius for $2g_v$ = 386 mm, $2g_h$ = 170 mm, N = 4

3. 3*D* computation and experiment

When choosing the spiral angle in the cyclotron design, it is necessary to take into account the fact that the magnetic field does not completely repeat the iron sector geometry [5].

According to Fig. 4, there exists an effect of magnetic spirality “netration” into the region of straight sectors [6]. This effect leads to a decrease in vertical focusing at radii smaller than 35 cm. This explains the widespread use of direct sectors in the central region. It is also seen that at radii ~ 75 ≤ r ≤ 88 cm there is a “lag” between the magnetic field spiraling angle and the geometrical one. The maximum lag reaches 7°, which at a spirality angle of 65° leads to a 30% decrease in focusing.

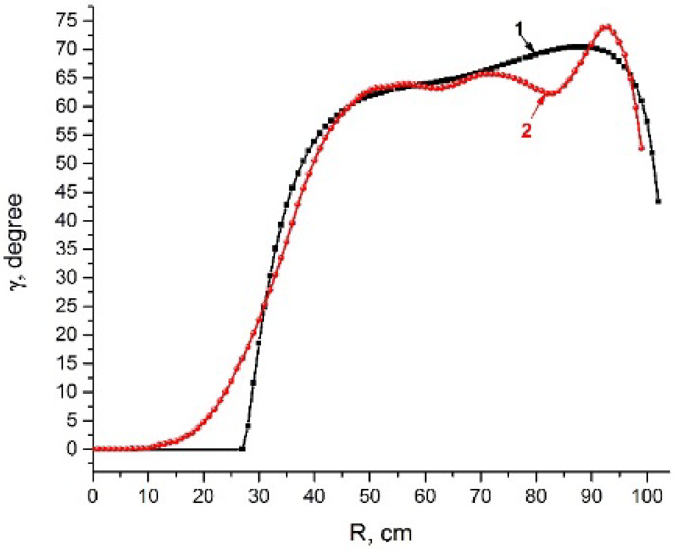

Fig. 4. The spirality angle γ (deg.) in dependence on the radius of the cyclotron: *1* – the data of the sector geometry spirality (*black*); *2* – the spirality of the fourth focusing harmonic of the magnetic field, obtained in 3*D* calculations and measurements of the magnetic field (*red*)

After preliminary assessments related to the choice of the parameters of the magnetic structure, the final variants were calculated in detail using the 3*D* MERMAID program.

In the calculations, to achieve the maximum accuracy, the magnetic structure was described using ~ 20.5 million straight prisms [7]. During the design process, two variants of the magnetic structure were considered at a finite radius: the flutter $F = 0.04$, the spirality angle $\gamma = 55°$, and $F = 0.025$ with $\gamma = 65°$, and the field variation amplitudes of 4.14 and 3.28 kG, respectively. Ultimately, the second option was adopted, providing a lower field in the hill, at which the loss of H^- ions due to electrodissociation does not exceed 2.6% [8].

4. Conclusion

The analysis of the structure of the magnetic field of a cyclotron with a high spirality angle, presented in this work, makes it possible to investigate the effect of different parameters of the structure and promptly compare various options. Such an approach provides the means to qualitatively analyse the effect of a decrease in the vertical focusing of the spiral structure at the centre of the cyclotron. It is expedient to use the structure with a large spiraling angle only at radii larger than the gap in the hill. In the central region, it is advisable to use direct sectors. The paper presents a technique that was used in the design of the magnetic structure of the C-80 cyclotron. The use of the limiting large values of the spirality angle in the C-80 cyclotron made it possible to obtain the limiting energy as high as 80 MeV in a magnet with a diameter of 2 m at an extraction radius of 0.9 m. The magnetic structure allows us to limit the negative ions electrodissociation to less than 2.6%.

References

1. H.G. Blosser, D.A. Jonson, Nucl. Instr. Meth. **121**, 301 (1974).
2. Yu.N. Gavrish *et al.*, in *Proc. 25th Rus. Part. Accelerator Conf. (RuPAC-2016),* 180 (2016).
3. N.K. Abrossimov, S.A. Artamonov, V.A. Eliseev, G.A. Riabov, Preprint PNPI 2049, 1995.
4. V.I. Danilov, Preprint JINR-R-409 (1959).
5. S.A. Artamonov, E.M. Ivanov, G.A. Riabov, in *Proc. 26th Rus. Part. Accelerator Conf. (RuPAC-2018),* 103 (2018).
6. D.A. Amerkanov, S.A. Artamonov, E.M. Ivanov *et al.*, in *Proc. 27th Rus. Part. Accelerator Conf. (RuPAC-2021),* 219 (2021).
7. S.A. Artamonov, E.M. Ivanov, G.A. Riabov, N.A. Chernov, in *Proc. 23th Rus. Part. Accelerator Conf. (RuPAC-2012),* 475 (2012).
8. S.A. Artamonov, D.A. Amerkanov, G.I. Gorkin *et al.*, in *Proc. of XX Int. Conf. Beam Dynamics & Optimization (BDO-2014),* 18 (2014).

CALCULATION AND OPTIMIZATION OF HIGH ENERGY BEAM TRANSFER LINES BY THE MONTE CARLO METHOD

D.A. Amerkanov, S.A. Artamonov, E.M. Ivanov, G.A. Riabov, V.A. Tonkikh

1. Introduction

The calculation of high-energy beam lines consists of tracing of the proton beam trajectories along the transport channel from the source. There are many programs in the world for calculating the optics of high-energy beams [1, 2]. In most of them, the ion source is represented in the phase space in the form of a multidimensional ellipsoid, inside which particles and their initial parameters are uniformly distributed, while there are no particles outside. Moreover, it is assumed that the beam emittance is conserved during the transport of the beam along the channel, which means that there are no beam losses in the channel. In particular, it is not possible to compute the effect of collimators on the intensity and other parameters of the beam. These assumptions greatly facilitate the mathematical formulation of the problem, but they do not quite reflect the experimental situation. In this work, a more adequate representation of the ion source is proposed.

The Proton_MK program code has been developed to carry out such calculations using the Monte Carlo method. The beam from the accelerator is introduced in the form of a multivariate Gaussian distribution in $x, x', z, z', dp/p$ phase space. In the case when an absorber (absorber, air section, window in the channel, *etc*.) is installed in the transport channel, the beam parameters after the absorber are calculated using the GEANT4 code. The output file of this code can be used as input for the program. The program allows calculation of any beam parameters – intensity, spatial or phase density, energy distribution, *etc*. The program includes a block for the optimization of beam parameters presented in a functional form. Random search method with learning for search correction based on analysis of intermediate results (so-called statistical gradient method) is used for obtaining the global maximum of a function of many variables. The program has been tested in calculations of the beam transport lines for the IC-80 cyclotron and for the development of the beam line for ophthalmology.

2. Representation of sources

In the experiment, the beam profile *i. e.* the distribution of the beam intensity over the transverse coordinates is well approximated by the Gaussian distribution, and the beam spot, *i. e.* intensity distribution in x–z plane is an ellipse. This situation is typical for a multivariate Gaussian distribution, where any marginal or partial distribution along any axis is also described by a Gaussian distribution. Let us assume that the beam in the ion source can be described by a five-dimensional normal distribution with a distribution function in space $\left(x, x', z, z', \delta\right)$ in the form

$$f\left(X, Z, s, \delta\right) = \frac{1}{\left(2\pi\right)^{5/2}\left|\Sigma\right|^{1/2}} \exp\left\{-\frac{1}{2}\begin{pmatrix} X \\ Z \\ \delta \end{pmatrix}^{T} \Sigma^{-1} \begin{pmatrix} X \\ Z \\ \delta \end{pmatrix}\right\}, \tag{1}$$

where Σ is a 5 × 5 symmetric matrix, which is the covariance matrix of the adopted distribution, *i. e.* the mathematical expectation of the distribution and its elements of interest, X is a vector (x, x'), Z is a vector (z, z'). The components of the matrix Σ have the form where $\sigma_{k\ell} = \langle y_k \cdot y_e \rangle y_k$, y_e are the components of the random vector $\left(x, x', z, z', \delta\right)$.

In most cases, the movements along x and z are independent and then $\Sigma_{xz} = 0$. In the case when the magnetic analysis takes place only in the x-plane, $\Sigma_{zp} = 0$. Based on the general properties of the multivariate normal distribution, it is possible to write the bivariate Gauss distribution in $x, -x'$ space in the form

$$f(X) = \frac{1}{(2\pi)\left|\Sigma_{xx'}\right|^{1/2}} \exp\left\{ -\frac{1}{2} X^T \Sigma_{xx}^{-1} X \right\}. \tag{2}$$

The elements of the correlation matrix Σ_{xx} are the mathematical expectations of the vector $(x_i\ x_j')$ *i. e.* $M(x_i x_j)$, where $i, j = 1, 2$ and $x_1 = x, x_2 = x'$. The matrix Σ_{xx} has the form

$$\sum_{xx} = \begin{pmatrix} M(x^2) & M(xx') \\ M(xx') & M(x'^2) \end{pmatrix} = \begin{pmatrix} \sigma_x^2 & \rho\sigma_x\sigma_{x'} \\ \rho\sigma_x\sigma_{x'} & \sigma_{x'}^2 \end{pmatrix}, \tag{3}$$

where $M(x, x') = \rho\sigma_x\,\sigma_{x'}$ by definition of the correlation coefficient ρ.

Then the bivariate Gaussian distribution on the plane takes the form

$$f\,(x, x') = \frac{1}{2\pi\sqrt{1-\rho^2}\;\sigma_x\sigma_{x'}} \exp\left\{ -\frac{1}{2\left(1-\rho^2\right)}\lambda^2 \right\}, \tag{4}$$

where $\sigma_x\,\sigma_{x'}$ are the standard deviations and ρ is the correlation coefficient. From the general form of the probability density of two random variables, it follows that the probability density is constant in all points of the xx' plane at which

$$\lambda^2 = \left(\frac{x^2}{\sigma_x^2} - 2\,\rho\,\frac{xx'}{\sigma_x\sigma_{x''}} + \frac{x'^2}{\sigma_{x'2}} \right), \tag{5}$$

where λ is an arbitrary value.

The curve on the xx' plane, defined by the equations above, is the so-called ellipse of equal probabilities. In the case of a Gaussian distribution, instead of one ellipse, there is a set of concentric ellipses each of which corresponds to the fraction of the beam particles lying inside the ellipse contour. Let us denote by *P*(λ) the probability of a beam particle to fall inside an ellipse with a given value of λ parameter and *F*(λ) the area of this ellipse in phase space:

$$P(\lambda) = \iint\limits_{\lambda} f\,(x, x')\,dx\,dx' = 1 - \exp\left(-\lambda^2\right), \tag{6}$$

$$F(\lambda) = \iint\limits_{\lambda} dx\,dx' = \sigma_x\,\sigma_{x'}\,\lambda^2 \Big/ \sqrt{1-\rho^2}\,. \tag{7}$$

If δ is a fraction of particles outside the ellipse, then

$$P(\lambda) = 1 - \delta,\ \ \lambda^2 = -2\ln\delta(1-\rho^2). \tag{8}$$

Gaussian distribution parameters can be determined by characteristic points of the ellipse. The ellipse of the beam and its three characteristic points x_1, x_2 and x_2' are shown in Fig. 1.

The sign of ρ corresponds to the sign of x_2. If $x_2 > 0$ then the beam diverges, and $\rho > 0$. If $x_2 < 0$, then $\rho < 0$, and the beam converges. In the case of $\rho = 0$, the beam is described by a straight ellipse.

3. Geant code usage

Another way of generation of the particle source is used when an energy degrader, a scattering foil or a vacuum window is presented in the channel.

In this situation, the beam behaviour in the degrader material is calculated by using the GEANT code. On the output of the program, a file containing the energy, transverse coordinates and velocities of the particles is produced. The file is then used as input for further tracing of trajectories through the channel.

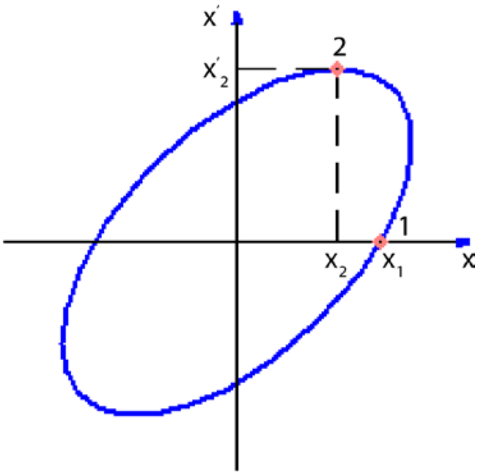

Fig. 1. Ellipse of the beam

4. The beam transport along a channel

The calculation algorithm is as follows: a five-dimensional vector $(x, x', z, z', dp/p)$ randomly generated according to the Gaussian distribution determines the initial conditions for a particle at the entrance of the channel. Then the particle with the chosen initial conditions is traced along the channel. The transport channel consists of standard magnetic elements located in different positions: quadruple lenses, various types of magnets, which provide deflection of the beam in different directions. In a linear approximation, the relationship between the input and output coordinates and velocities in the transport element can be obtained using the transition matrix, which is different for each element.

The mathematical expression for the transition matrices were formulated in many works. In this work, we used the coordinate system and the transition matrices from Steffen's monograph [3]. The calculation of the trajectory of a particle along the channel is carried out step-by-step by application of transition matrices for magnetic elements. At the output of each element, the x and z coordinates are compared with the apertures. If a particle falls out of the aperture, then its transport is stopped and it is counted as a lost particle. As a result of multiple repetitions of this procedure (several thousand times), the beam parameters are evaluated at the output of each element.

5. Optimization

In addition to the problem of calculating the beam parameters in a channel with a given configuration, it is often necessary to obtain the optimal value of some beam parameter by changing the configuration of the channel or by varying the magnetic field in the channel elements. This problem is solved in this work by using the Monte Carlo method. Different beam parameters such as intensity, energy distribution and so on are calculated using the above technique. In our case, one of the random search methods, the statistical gradient method, was used for optimization. The calculation algorithm is as follows. A sequence of random vectors is selected whose components are variable parameters with a normal distribution with dispersions σ_i and mean value X_0.

$$\overrightarrow{\mathrm{X}}^K = (x_1^K, x_2^K, x_3^K, \ldots x_n^K), \quad K = 1, 2, \ldots n. \tag{9}$$

For each set of randomly selected parameters, *i. e.* for each vector, the quality function $\Phi(\vec{\mathrm{X}}^K)$ is calculated, the maximum $\Phi_m = \max \Phi(X)$ and the vector $\vec{\mathrm{X}}^M$ for which $\Phi = \max \Phi$ are found [4].

6. Algorithm realization

Based on the described algorithm, a code with a graphical interface Proton_MK has been developed. The program is written in C++ and can be compiled to produce an executable file for Windows. The interface Proton_MK provides the following opportunities:

- Calculation of the high energy beam transport lines which consist of quadruple lenses, bending magnets, free space, collimators;
- Generation of a particle source – a sample of N particles with the axial momentum of the channel p_0 and the parameters of the Gaussian distribution σ_0, σ_x, σ_x', σ_z, σ_z', ρ_x, ρ_z, $\Delta p/p$;
- Beam import after the absorber according to the GEANT4 calculation;
- The output of beam parameters at any channel element;
- Variation of the operation modes of a large number of optical elements of the channel to optimize the output beam parameters;
- The calculation results are presented in the output report.

The program was tested during the development of the beams with energy of 50–900 MeV by decelerating the primary proton beam with energy of 1 000 MeV in a copper absorber. Good agreement of calculation results with experimental data was achieved. Another example of the application of the program was the design of the beam for ophthalmology with a high degree of homogeneity [5] at the IC-80 accelerator. A beam with an intensity of 10 µA is extracted from the accelerator and then is focused onto a thin 300 µm tantalum scattering plate. The collimator after the foil preserves the central and uniform part of the scattered beam in such a way that a beam with a diameter of 60 mm and an intensity of 10^{10} s^{-1} falls into the patient's irradiation room with a 5% uniformity in intensity and a minimum divergence. The beam line for ophthalmology and the beam envelopes are shown in Fig. 2.

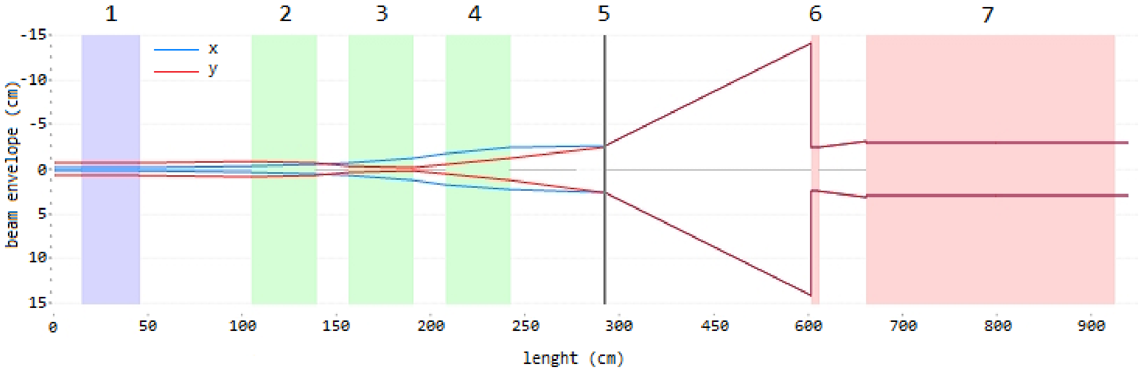

Fig. 2. Ophthalmic beam line and beam envelopes on the level 95% of the intensity: *1* – corrector magnet; *2–4* – quadruple lenses triplet; *5* – tantalum scattering foil 300 µm thick; *6* – collimator; *7* – radiation shielding wall in front of the irradiation room

References

1. K.L. Brown, A First and Second Order Matrix Theory for the Design of Beam Transport Systems and Charged Particle Spectrometers, SLAC Report No. 75, 71–134 (1968).
2. K.R. Crandall, D.P. Rusthoi, TRACE 3-D Documentation, LA-UR-97-886 (1997).
3. K.S. Steffen, High Energy Beam Optics, 211 (1965).
4. D.M. Kuzmenkov, V.I. Chernetsky, Method of Searching for Global Extreme in Linear and Nonlinear Programming Problems Under Arbitrary Constraints: Algorithms and Programs for Random Search ed. Knowledge, 145 (1969).
5. D.A. Amerkanov, S.A. Artamonov, E.M. Ivanov *et al.*, in *27th Rus. Part. Accelerator Conf. (RuPAC'21)*, MOPSA44 (2021).

THE CALCULATION METHOD AND OPTIMIZATION OF A PROTON BEAM LINE WITH COLLIMATORS BY USING COURANT–SNYDER FORMALISM

D.A. Amerkanov, S.A. Artamonov, E.M. Ivanov, V.A. Tonkikh

There are many ways to optimize and calculate the lines of charged particle beams. Calculation methods based on the approximation of the phase ellipse of the beam are widely used. The beam is represented by a 6×6 matrix defining a hyperellipsoid in six-dimensional phase space. The projection of this hyperellipsoid on any two-dimensional plane is an ellipse that defines the boundary of the beam in that plane. This hyperellipsoid can be mathematically specified by Courant–Snyder (or Twiss) parameters [1].

However, this method is not designed for the use of limiting apertures or collimators in the beam line. Therefore, an artificial technique was employed. The effect of the collimator on the phase portrait of the beam was taken into account as follows.

Let the z-axis of the reference system is directed along the beam axis, x is the horizontal coordinate, and y is the vertical one. Let the collimator be a square 3 × 3 mm. The collimator acceptance is imposed on the x and y phase ellipses of the beam at the entrance to the transport path. The acceptance is represented by two straight lines mapped using the collimator aperture transition matrix $x, y \leq 3$ mm onto the entrance of the beam line.

According to Ref. [2],

$$\vec{\mathrm{X}} = M\vec{X}_0,$$

where $M = \begin{pmatrix} M_{11} & M_{12} & 0 & 0 \\ M_{21} & M_{22} & 0 & 0 \\ 0 & 0 & M_{33} & M_{34} \\ 0 & 0 & M_{43} & M_{44} \end{pmatrix}$, $\vec{\mathrm{X}} = \begin{pmatrix} x \\ x' \\ y \\ y' \end{pmatrix}$, $\vec{\mathrm{X}}_0$ are the coordinates and angles of motion of the particle at the entrance to the beam line.

It is obvious that particles whose coordinates satisfy the following relations will pass through the collimator:

$$|x| = |M_{11}x_0 + M_{12}x_0'| \leq A,$$
$$|y| = |M_{33}y_0 + M_{34}y_0'| \leq A.$$

Here $|M_{11}x_0 + M_{12}x_0'| = A$ and $|M_{33}y_0 + M_{34}y_0'| = A$ are, respectively, parallel straight lines in the phase space of the beam x–x' and y–y', which are the mapping of the collimator acceptance to the beam line entrance.

Further, a new ellipse is inscribed in the part of the phase space bounded by the input beam ellipses (vertical and horizontal ones at the input of the beam line) and the straight lines of the reflected collimator (this allows one to remain in the TRACE-3*D* formalism working with beam ellipses). This procedure makes it possible to find the ellipse and emittance of the beam passing along the beam line and through the collimator without losses. The ratio of the area of the inscribed phase ellipse to the area of the original ellipse determines the intensity reduction factor.

For example, let us consider one of projects for a beam line for the C-80 cyclotron. Its scheme is shown in Fig. 1. The effect of the collimator on the phase portrait of the beam is shown in Fig. 2.

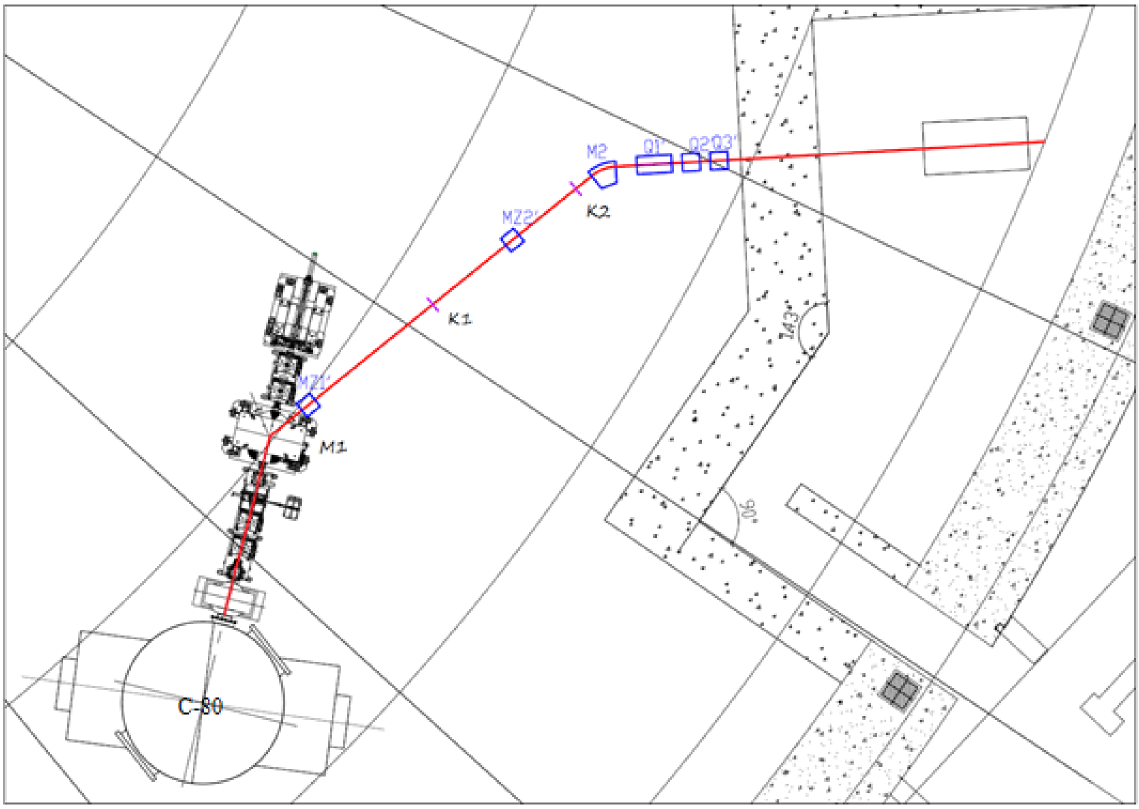

Fig. 1. Optimized beam transport path for ophthalmological needs. Here MZ1 and MZ2 are bending magnets in the vertical plane; M1 and M2 are bending magnets in the horizontal plane; K1 and K2 are collimators; Q1, Q2 and Q3 make up a triplet of quadrupole lenses

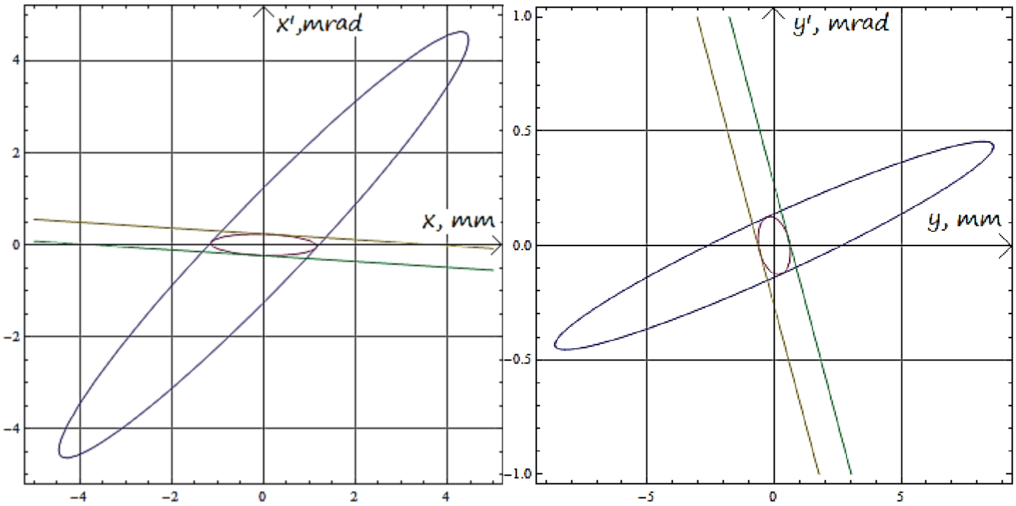

Fig. 2. Horizontal ellipse *x*–*x*' *(left*); vertical ellipse *y*–*y'* (*right*)

Figure 3 shows a screenshot of the result of the TRACE-3*D* software on optimizing the proposed beam line transportation. Above are the optimal values of the gradients of the magnetic fields of the quadrupole lenses. At the bottom of Fig. 4, the upper line corresponds to the horizontal beam envelope (in relation to the midline), and the lower line corresponds to the vertical beam envelope.

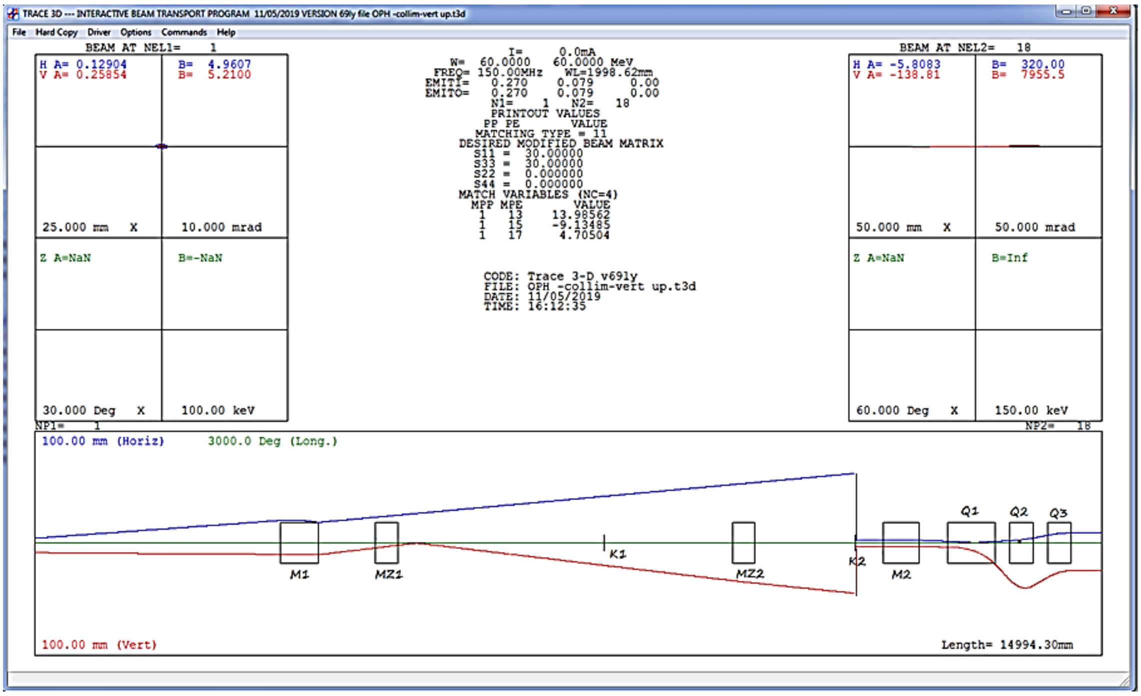

```
          I=       0.0mA
   W=  60.0000   60.0000 MeV
 FREQ= 150.00MHz   WL=1998.62mm
EMITI=    0.270    0.079      0.00
EMITO=    0.270    0.079      0.00
          N1=    1   N2=   18
          PRINTOUT VALUES
         PP PE        VALUE
        MATCHING TYPE = 11
      DESIRED MODIFIED BEAM MATRIX
        S11 =  30.00000
        S33 =  30.00000
        S22 =  0.000000
        S44 =  0.000000
      MATCH VARIABLES (NC=4)
        MPP MPE        VALUE
         1   13     13.98562
         1   15     -9.13485
         1   17      4.70504


          CODE: Trace 3-D v69ly
          FILE: OPH -collim-vert up.t3d
          DATE: 11/05/2019
          TIME: 16:12:35
```

Fig. 4. TRACE-3*D* optimization calculation results and beam envelopes

References

1. K. Crandall, D. Rusthoi, TRACE 3-*D* Documentation, LA-UR-97-886, 106 (1997).
2. K.G. Steffen, High Energy Beam Optics (1965).

STRATEGY OF EQUIPPING THE PIK REACTOR EXPERIMENTAL STATIONS WITH DETECTION SYSTEMS

A.G. Krivshich, D.S. Ilyin

1. Introduction

Due to the appearance of new high-intensity neutron sources and new ways of application of high-performance neutron focusing optical systems, the intensity of neutron beams has increased significantly over the past 10–20 years. General technical progress and new ideas implemented into the construction of the experimental stations and creation of new detector systems allowed one to achieve great potential in the field of neutron scattering research, which recently seemed impossible.

The necessity to develop and apply new research methods for both the study of new class objects and the search for solutions of experimental tasks at the highest level requires equipping the PIK reactor instrumental infrastructure with state-of-art neutron detection systems produced in Russia and worldwide. The PIK reactor is being constructed at the PNPI.

The quality of information received within a modern experiment quite often depends directly on practical realization of a complex of interconnected (and sometimes mutually contradictory) maximum attainable characteristics of the detection systems. Namely, these specifications are the folowing: large registration area, high neutron rate requirements and spatial resolution, low noise level, high performance within the whole required wavelength range of neutrons, very low sensitivity to the background radiation, high stability of functional specifications, low cost and maintainability.

The aim of the present paper is to develop strategies of equipping the PIK reactor experimental stations with the detection systems based on three main factors:

- Analysis of experience accumulated by the leading neutron research centres over the last 40 years;
- Clear understanding of the current state over the last 10 years and ways of practical realization of the development trends of detection technologies;
- Estimation of the global trends of the development of detection technologies and definition of the concept of their further development for the next 10–15 years.

It is clear that the concept of development of neutron detectors for experimental stations of the PIK reactor should be based on the experience of the leading Russian and international neutron research centres, such as ILL (France), J-PARC (Japan), ESS (Sweden), FZ (Jülich, Germany), *etc*.

2. Analysis of experience of world research centres in the field of neutron detector construction

2.1. Over the last 40 years. Analysis of experience of the world research centre ILL, France

In order to produce neutron detectors for the experimental stations of the PIK reactor, it is essential to take into account the world experience, knowledge and achievements of specialists working in the field of development of various types of neutron detectors.

ILL is currently the unofficial world capital of neutron research (https://www.ill.eu/instruments-support/instruments-groups). Experience of neutron experiments was accumulated in this Institute for over 40 years with participation of world leading experts from many different countries contributing to it. Unique world-class experimental stations were created, and their parameters were optimized based on simulations and experiments.

According to its purpose, the structure of instrumentation base in the main neutron centres of the world is approximately the same as in ILL. The neutron flux density of the PIK reactor is expected to be similar to that of the high-flux reactor (HFR) at ILL, which essentially makes the PIK reactor a potential future successor of the HFR. For this reason, it would be reasonable to copy both the general instrumentation structure of ILL and appropriate types of neutron detectors, and to apply this knowledge to the PIK reactor installations. Various devices at ILL are brought to perfection, and their parameters are optimized basing on simulations, real testing and experiments.

Classification of the types of detectors used for ILL experimental stations and detection technologies are presented in Table 1.

Table 1

Classification of the types of detectors used at ILL

Detection technology	Type of detector	Amount
Gas-discharge detectors based on ^{3}He converters	Proportional counter (^{3}He)	9
	Multidetector and installation based on proportional counter	14
	Single- and multimodule microstrip detectors (micro strip gas chambers – MSGC)	6
	^{3}He 2*D* position sensitive detector	10
	Neutron beam monitor	4
	Total	43
Scintillation detectors based on solid-state converters (^{6}Li and ^{10}B)	Scintillation detector based on ZnS / LiF	2
	Scintillation detector ImagePlates	2
	Total	4

It is obvious that, despite the ^{3}He deficit, the leading European neutron research centre, ILL, uses detectors with ^{3}He as a converter gas in the vast majority of its experimental stations (43 out of 47).

2.2. Current status over PAST 10 years. Analysis of experience of the world research centre J-PARC, Japan

The materials and life science experimental facility (MLF) neutron research centre was founded in J-PARC (http://j-parc.jp/index-e.html). MLF uses a high-intensity pulsed spallation neutron source generated by the 3GeV proton beam with the current of 333 μA and the operating frequency of 25 Hz.

Implementation of new scientific and applied research programmes required new experimental stations equipped with new detectors. An analysis showed that in order to use ^{3}He-detectors it would be necessary to acquire more than 10 000 l of this gas. Taking into account the rise of its price, such acquisition will require a serious financial investment – more than 20 million dollars for a period of five years.

Taking into account this reason, it was decided to use scintillation technologies for detectors having the surface of complex geometry and a wide aperture (five stations). In order to comply with the required detector parameters, standard scintillators based on ZnS / ^{6}LiF were dismissed in J-PARC and ceramic scintillators based on ZnS / $^{10}B_2O_3$ were put into operation. This allowed one to improve the parameters of existing scintillation detectors with regard to enhancement of their operation speed, efficiency, decreasing their afterglow and so on. With these enhancements, the efficiency of such scintillation detectors achieved about 70% of the efficiency of ^{3}He-detectors (at 4 bars). This work required creation of a new “scintillation” infrastructure in J-PARC and more than 10 years of hard work. Currently, it can be said that the situation with the application of different types of detectors is balanced in the best way in J-PARC instruments. The proportion of experimental stations with different types of detectors is demonstrated in Fig. 1 (the stations with scintillation detectors are marked with yellow filling and the stations with ^{3}He-detectors – with red filling) [1]. It is obvious that the majority of detectors used are ^{3}He-detectors. They are used in order “to cover” large areas, to work in high-intensity neutron-beams – up to $1 \cdot 10^8$ cm$^{-2} \cdot$ s^{-1}, to work with relatively small apertures (up to 300×300 mm^2) when the method of delay line readout is used (with only five channels of registration electronics), which significantly reduces the cost of the detector.

The J-PARC centre is equipped with more than 21 experimental stations, most of which (about 75%) use gas-filled ^{3}He-detectors.

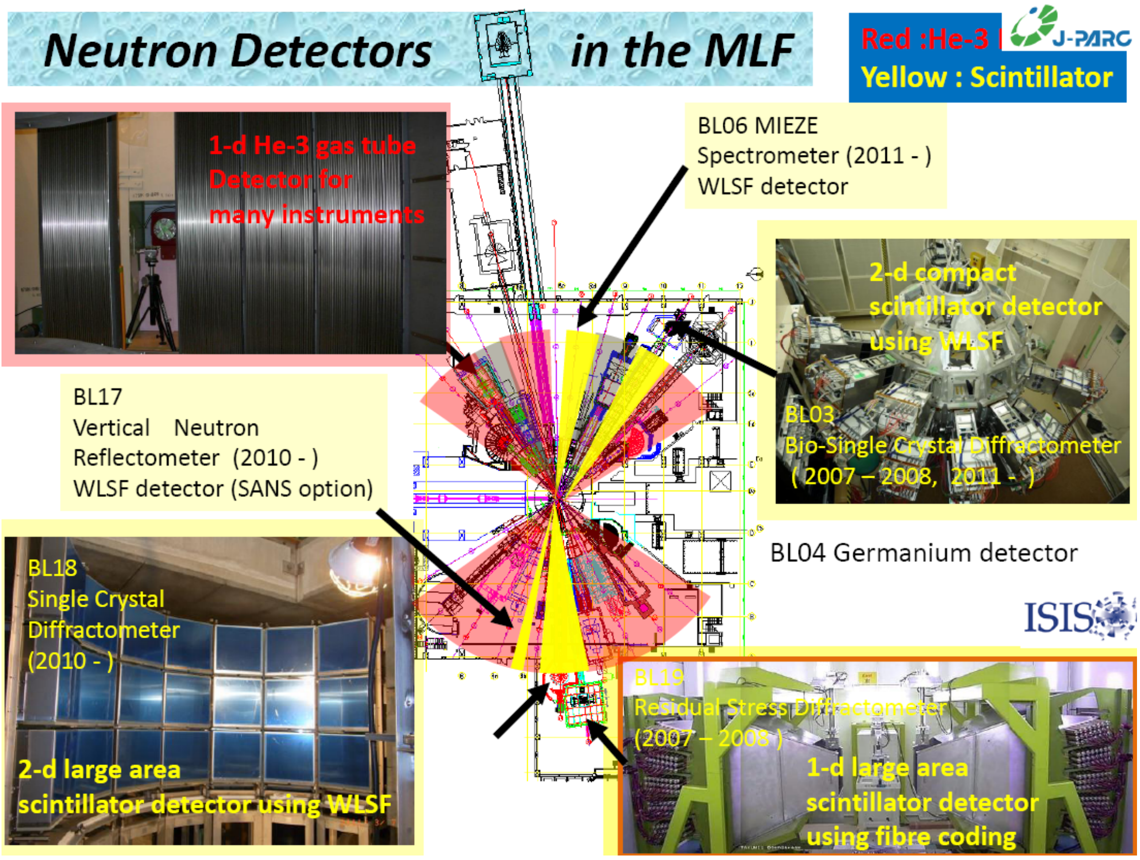

Fig. 1. Location and structure of neutron detectors at MLF experimental stations (J-PARC)

2.3. Estimation of the global trends for the next 10–15 years. Analysis of experience of the world research centre ESS, Sweden

European Spallation Source (ESS) is being actively built in Lund, Sweden. The first neutrons were planned to be generated in about 2020. It is also planned that ESS with its initial suite of experimental stations will be put into operation no later than in 2025. An international expert group was formed in order to perform an analysis of technical requirements for ESS experimental stations and the neutron detectors required for them [2]. The analysis presented here is based on the initial suite of 22 instruments, put forward in the ESS technical design report in 2013.

It appeared that the total area of neutron detectors exceed 280 m^2. More than a half of the area is reserved for three installations – three chopper spectrometer instruments (80, 50 and 30 m^2). The total number of channels of registration electronics is quite large as well, it exceeds 60 000. It is worth noting that only two experimental stations should have the spatial resolution of 0.1 mm. The spatial resolution of other detectors should vary in the range of 1–10 mm, which is possible to achieve with the existing technology. In the course of the analysis, all detectors were divided into four categories according to their registration area: large-area detectors (two stations); high-resolution medium-area detectors (nine stations); small-area detectors with the area of 1 m^2 and less (nine stations) and ultrahigh-resolution detectors (two stations).

The detectors from the first two categories occupy about 90% of the total area of all the detectors. In order to produce them using the ^{3}He-technology, it would be necessary to acquire more than 25 000 l of ^{3}He, which is quite a large sum with respect to the current European prices – about 50 million dollars. The need to decrease the expenses involved in acquisition of ^{3}He essentially defined the choice of the strategy of the detector production.

1. First two categories of detectors are to be based on detectors that do not use ^{3}He.

2. Small area detectors (the third category) are to be based on the ^{3}He-detectors with the aim to ensure maximum attainable parameters. Such are 9 of 22 experimental stations (40%).
3. Ultrahigh-resolution detectors can be produced based on scintillation detectors or gas-filled detectors gas electron multiplier (GEM) or micromesh gaseous structure (Micromegas).

Production of detectors that do not use ^{3}He will be implemented in three basic directions. Their development requires significant financial investments and significant efforts of the international community [3]:

- ^{6}LiF / ZnS and B_2O_3 / ZnS scintillation detectors with the wave length shifting fibers readout;
- Gas detectors with ^{10}B solid converters;
- Position sensitive gas detectors based on BF_3.

At ESS, the primary choice for ^{3}He replacement technology was decided to be gaseous detectors with a ^{10}B solid converter.

On the way to the creation of new detector technologies, there is a lot of open questions and difficult outstanding issues that should be solved for the technical parameters of new detectors to come as close as possible to the parameters of modern ^{3}He-detectors.

The developers will have to take into account the following parameters: efficiency of new detectors should be equivalent to that of ^{3}He-detectors; the capability of operating in high-intensity neutron beams; a low sensitivity to γ-background – the key factor for many experiments; an essential reduction of the cost of large area detectors.

2.4. Peculiarities of detector infrastructure in several other world leading scientific neutron centres

2.4.1. Current state of neutron detectors and trends of their development in Russian research centres

The neutron detectors that are currently most widely used in the Russian Federation can be divided into two main categories: gas-filled detectors and scintillation detectors.

Gas-filled detectors. Russian experts made a notice of favourable conditions for production of ^{3}He position sensitive detectors (PSD) up to 300 × 300 mm^2 in Russia. The PNPI and Joint Institute for Nuclear Research (JINR) groups are successfully developing and producing such detectors and are experienced in this field. A group from the Institute for Nuclear Research of the Russian Academy of Sciences (INR RAS, Troitsk) works now with such detectors as well. Many years of activity in this direction have allowed one to develop stable technologies for production of gas-filled PSDs. Relative availability of ^{3}He in Russia and its lower price (in comparison with the global prices) act as a powerful motivation to continue the work with ^{3}He gas-filled PSDs.

Detection systems based on helium counters operate at the IBR-2M reactor of JINR Laboratory of Neutron Physics (further – LNP) as a part of the experimental stations NERA, SKAT, EPSILON, DN-12, DIN-2PI and at the reactor VVR-M of PNPI. The possibility to measure both coordinates by means of mutually orthogonal cathode planes in a proportional chamber allows one to use 2*D* PSDs in order to perform measurements using the methods of small-angle neutron scattering. Detectors of this type are used in spectrometers REFLEX, GREINS, DN-2 at LNP JINR and at INR RAS (Troitsk), *etc*.

For neutron beam monitors, low efficiency is needed – typically in the region of a tenth-thousandth of a percent. In order to reach such a low level of detection efficiency, the monitor was filled with a gas mixture of 50 mbar ^{3}He + 950 mbar CF_4. The monitor was used to measure the profiles of the IBR-2M reactor beams. N_2 was added to the mixture as a converter-gas in order to be able to work with ultra-high fluxes ($\geq 10^7$ cm$^{-2} \cdot$ s^{-1}).

Scintillation detectors. Scintillation methods are particularly attractive in time-of-flight neutron spectrometers. This is caused by the fact that in scintillation detectors, the detection layer is by an order of magnitude thinner and, consequently, their time-of-flight resolution is better compared to the gas-filled detectors. A higher sensitivity of scintillation detectors to γ-background does not affect the results of time-of-flight experiments. In addition to a high efficiency of thermal neutron registration ($\lambda \leq 1$ Å) and time resolution of less than a microsecond, such detectors are capable of a spatial resolution of about 100 µm.

JINR and PNPI jointly developed a scintillation detector already in the end of 1990s. The design solution was further developed in the RASTR detector for a diffractometer ($\lambda \leq 1{,}53$ Å, the interplanar spacing resolution being $\Delta d / d = 0.2$–0.3%) of the Institute of Metal Physics of the Ural Branch of the Russian Academy of Sciences. The experience of production of modern scintillation detectors gained by LNP JINR is the basis for the future joint PNPI and JINR developments, which will be used at the PIK reactor.

2.4.2. Forschungszentrum Jülich (FZ Jülich, Germany)

FZ Jülich possesses over 30 experimental stations, most of which are at FRM II in Germany, three of which are at ILL, three – at the spallation neutron source (SNS), two – under construction (http://www.fz-juelich.de/jcns/EN/ Leistungen/InstrumentsNEW/_node.html). Several instruments are planned as a contribution to the ESS. The majority of these stations are designed for the investigation of processes of elastic (15 instruments) and inelastic (13 instruments) neutron scattering.

The analysis shows that more than 70% of the stations use ^{3}He-detectors that are implemented as 2*D* PSDs (with the aperture – up to 500 × 500 mm^2, the spatial resolution – 2 mm) and proportional counters (from 100 to 1 000 mm long).

2.4.3. Brookhaven National Laboratory (BNL, USA)

BNL no longer has a research reactor, but implemented previously a research development programme focused on creation of high-precision thermal neutron PSDs and equipped with them the experimental stations of national research centres (USA), in particular for the SNS for structural biological and chemical research (http://www.inst.bnl.gov/programs/gasnobledet/neutrons/neutron_brochure.pdf).

All the BNL detectors are ^{3}He-detectors based on proportional chambers with the data readout from cathode strips.

2.4.4. Some other centres

In other centres, for instance Rutherford Appleton Laboratory (RAL, UK) at the spallation neutron source ISIS or Oak Ridge National Laboratory (ORNL, USA; SNS and the HFIR reactor), the correlation of gas-filled and scintillation detectors is a little more balanced. RAL successfully used scintillation technologies for neutron registration. The higher importance of the time resolution at a pulsed spallation source, along with the better efficiency for lower wavelength neutrons, is the primary motivation behind the higher fraction of scintillator detectors for spallation sources.

3. Final analysis of the global trends of neutron detector development

Basing on the analysed experience of the most significant Russian and international neutron research centres and on their development trends drawn out in the course of the analysis (some of them were mentioned above), one can propose a strategy for development of neutron detectors and equipping the experimental stations of the PIK reactor. The results of the analysis and prediction of the detection technology development based on it demonstrate clearly the development strategies of neutron detectors over the period of more than 60 years (40 years of past + “the current” period of the last 10 years + about the next 10 years of the future) based on three main international neutron centres.

1. Using the example of the ILL experimental stations, an analysis of the neutron detector structure established over the last 40 years is presented.

In the course of these 40 years, unique world-class experimental stations were created, and their parameters were optimized based on simulations and experiments. The absolute majority of detectors (90%) are gas-filled devices using ^{3}He as a neutron converter.

2. The current state and practical implementation of the “current” development trends of detection technologies (over the last 10 years) were analysed on the example of the MLF centre operating as part of the neutron research centre at J-PARC (Japan).

About 75% of the detectors are gaseous detector devices using ^{3}He as a neutron converter. Implementation of new scientific and applied programmes required creation of new complex experimental stations (five units) equipped with the detectors based on scintillation technology.

3. The estimation of the global trends of the detection technology development and generation of their development strategies (for the next 10 years) were considered based on the baseline ESS instrument suite from the technical design report as an example.

Small-aperture detectors (1 m^2 and less) are in many cases planned to be produced based on the ^{3}He-technology. Such are 9 of 22 experimental stations (40%).

Nine more detectors (40%) having medium and large aperture (from 1 to 80 m^2) will be created based on the following technologies: scintillation detectors and gaseous detectors based on the ^{10}B solid convertor. It is assumed that for the next 5–7 years these technologies will reach such a level that their parameters can come close to those of ^{3}He-detectors.

So, the gas-discharge ^{3}He-detectors will be the basic development direction at least for the next 10 years. This is connected with the outstanding combination of properties of the detectors using ^{3}He as a neutron converter, which defined the inclination of neutron centres towards the use of such detectors for their experimental stations throughout their history.

A transition to different detection technologies based on ^{6}Li and ^{10}B converters that are being currently developed is mostly caused by the necessity and has the aim to reduce the cost of devices by means of abandoning the use of ^{3}He in large volume detectors. At the same time, it should not cause an intention to upgrade all the detector knots of the instruments, since, on the one hand, it would require a significant financial investment, and on the other hand, it would guarantee a change of a number of characteristics of devices for the worth: registration efficiency, spatial resolution, γ-background sensitivity and so on.

It is necessary to perform a detailed and thorough analysis of applicability of different detection technologies to a specific physical task, to a specific physical instrument. For instance, scintillation detectors are effective in the cases when it is necessary to achieve a high spatial resolution (≈ 100 μm) and to build a complex geometry shape of the registration surface.

4. Analysis of the issue of ^{3}He deficit

An analysis of the ^{3}He demand for the equipment of neutron detectors operating as a part of the neutron scattering research at large international neutron centres has been presented (http://dx.doi.org/10.1080/10448632.2012.725325, http://www.tandfonline.com/doi/full/10.1080/10448632.2012.725325) see Table 2. It should be noted that this is a minimum estimate of a global ^{3}He demand. For instance, Table 2 does not include the information of ESS detectors requiring more than 25 000 l of ^{3}He.

Based on the comparative analysis of the data presented in Table 2, it is possible to state that the demand of experimental facilities of the PIK reactor for ^{3}He is relatively small, around 900 l, which is a great deal less than the amount required by any more or less significant national or international centre.

One can see (Tables 3 and 4) that about 70% of neutron detectors are ^{3}He-detectors, which corresponds well with the global development trends. The cost of ^{3}He for the PIK reactor is relatively low (one-time investments of ~ 0.9 million dollars USA) and the advantages gained by the PNPI international neutron research centre based at the PIK reactor are positively significant. Such as:

- Detectors based on ^{3}He have a generally accepted unique complex of performance characteristics;
- PNPI already possesses technologies necessary for development and production of neutron detectors with aperture of up to 300 × 300 mm^2 (and larger), which guarantees compliance with the complex of requirements for modern neutron detectors. It does not require significant financial investment in technology. A technological modernization would be necessary due to creation of detectors with aperture of 1 000 × 1 000 mm^2;
- There are almost no sources of ^{3}He acquisition in Europe, and its price there is rather high;
- For this reason, the European scientific community is actively searching for alternative neutron converters and conceptually new construction ideas in order to create detectors that could replace ^{3}He detectors.

^{3}He is available in Russia, and its price is several times lower than the European one. For this reason, detectors based on ^{3}He are our competitive advantage over Europe, which certainly should be used to the fullest extent.

Table 2

Analysis of ^{3}He demand in the leading neutron centres of the world

Neutron centers	Exploitation of detectors and research, l/year	New small-aperture detectors, l	New large-aperture detectors, l
ORNL (SNS)	100	1 300	25 000
ORNL (HFIR)	100	1 210	2 500
Los Alamos	100	1 994	12 362
NIST	100	560	40
BNL	50	180	–
FRM II	100	650	4 500
HZ Berlin	100	520	7 850
ILL	100	1 000	3 000
JCNS	40	15	7 200
LLB	50	600	600
PSI	50	–	2 000
STFC	100	400	11 300
J-PARC	100	40	16 100
JRR-3	31	71	–
KAERI	150	–	2 000
CSNS	200	–	21 000
Total	1 431	8 540	115 372
The PIK reactor	10	900	0

Table 3

Types of detectors proposed for applications at the PIK research complex and their quantity

Device / detector	Gas neutron converter (^{3}He)		Solid neutron converters (^{6}Li and ^{10}B)	
	Proportional counter and 2*D*-module based on LPSC counter	2*D* position sensitive detector	Scintillator	Solid-state detector
Powder diffractometer	3 (D1, D2, D3)	–	–	–
Crystal diffractometer	–	3 (DC1, DC3, DC5)	3 (DC3, DC4, DC6)	–
Inelastic scattering spectrometer	2 (IN4)	1 (IN2)	3 (IN1, IN3, IN5)	–
Small-angle instrument	2 (S2, S3)	3 (S1, S4, S5)	–	–
Reflectometer	4 (R1–R4)	4 (R1–R4) 2 (R2, R3)	–	–
Total number	11	13	6	–

Table 4

Detectors operating in neutron beams of different intensity at PIK

Intensity of neutron beams, s^{-1}	Experimental station	Number of detectors, un.	Detector technology
Up to $1 \cdot 10^5$	S1	1	2*D* PSD (^{3}He)
	D2, IN2, IN4 (2 un.)	3	^{3}He proportional counter and LPSC
	IN1, IN3	2	Scintillators
Up to $1 \cdot 10^6$	DC1–DC5, DC7, S3, S4, S5, R1, R2, R3, R4	12	2*D* PSD (^{3}He)
	D1, D3, S2, R1–R4	7	^{3}He proportional counter and LPSC
	DC3, DC6, IN5	3	Scintillator
Up to $1 \cdot 10^7$	Beam monitor (R2, R3)	2	2*D* PSD (^{3}He-technology)
	None	0	^{3}He proportional counter and LPSC
	None	0	Scintillator
–	Total	30	–

5. Analysis of the PIK reactor planned instrumental facility and recommendations on equipping the experimental stations with neutron detectors

An analysis of the PIK reactor instrumental facility with regard to compliance of the neutron detectors with all the required operation parameters has been performed based on the information on detectors and strategic trends of their development in the leading neutron research centres of the world and analogous centres in Russia [4].

Detectors that are planned to be used at the experimental stations of the PIK reactor are listed in Table 3. Requirements for the loading capability of detectors with ^{3}He-converter are presented in Table 4. The background level and the γ-background sensitivity are stated as the maximum loading capability / background count of $\geq 10^6$ and the minimum possible sensitivity to the γ-background ($< 1 \cdot 10^{-7}$).

It is clear from Tables 3 and 4 which detection technologies should be given a high priority for the development at PNPI.

^{3}He detection technologies necessary for equipping the majority of experimental stations of the PIK reactor either exist at PNPI or can be produced there since there are technological capabilities for their development and realization.

1. PNPI already possesses technologies necessary for development and production of neutron detectors with aperture up to 300 × 300 mm^2 (and larger), which comply with the requirements of the current physical experiments (Fig. 2). Creation of such detectors does not require now any significant financial investments in their development stage. Based on these technologies, one can fabricate ^{3}He-detectors of different structural variations including the capacity to operate in vacuum.
2. Beam intensity: up to $1 \cdot 10^6$ s^{-1}. For the existing 2*D* PSD ^{3}He-detectors to be able to work in intensive neutron fields, it is necessary to change the data readout method from a delay line readout to channel-by-channel readout from the cathode strips.
3. Beam intensity: up to $1 \cdot 10^7$ s^{-1} and higher. If the experiment requires the detector to operate in a counting mode with efficiency close to 100%, then it is necessary to perform a detailed analysis of new detection technologies such as, 2*D* linear position sensitive counters (LPSC), GEM-technology, pad-structural gas-discharge detectors, scintillation detectors, *etc*.
4. Neutron beam monitors have a very low efficiency, which allows them to work in neutron beams of very high intensity ($1 \cdot 10^8$ s^{-1}).

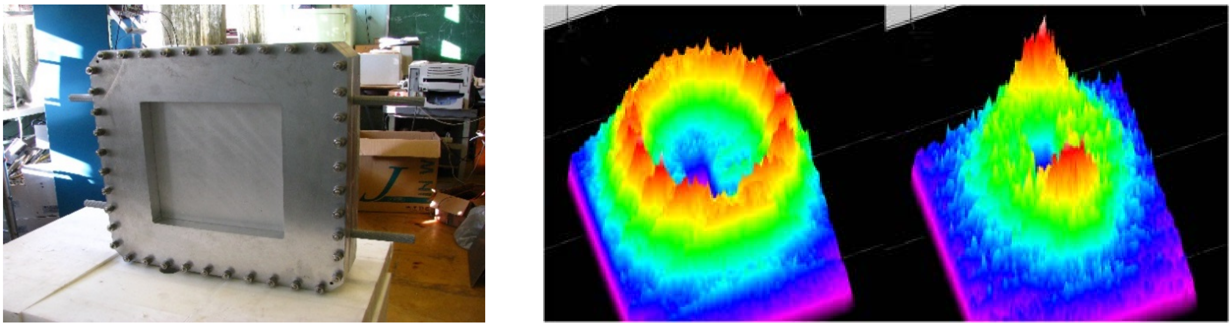

Fig. 2. Neutron detector (*left*); asymmetric scattering of neutrons on a fluoroplastic film before its deformation and after (*right*)

In order to create 2*D* detectors with aperture of 1 000 × 1 000 mm^2 based on LPSC, it is necessary to update the technological line, to develop prototype models and registration electronics.

The production of banana-type detectors based on LPSC-technologies (or microstrip gas chambers) requires a separate development.

Special attention should be paid to the development of scintillation detection technologies: the PIK reactor experimental stations are not yet fully equipped with such technologies, which are being actively developed in the world and have their own technological niche, such as:

- Fabrication of wide-aperture detectors of complex geometry;
- Neutron beam monitors;
- Practical applications of neutron tomography requiring the creation of detectors with high spatial resolution at the level of 0.1 mm (and higher), *etc*.

Taking into account the insufficient technological potential existing at PNPI in this field and quite significant financial investments needed to be done in the future, it is necessary to join efforts and support the joint activities of the developing collaboration of PNPI, JINR and INR RAS aimed at the applied development of scintillation technologies.

Neutron imaging for the purposes of tomography and radiography is a separate research field that is widely developing in modern sources, but is still not listed among the PIK reactor research stations.

The most advanced installations for neutronography and neutron tomography in Europe are located at the FRM II reactor in cold and thermal neutron beams and at the PSI – cold and thermal neutrons. The analogs are put in operation at the National Institute of Standards and Technology – NIST (USA).

Currently, the development of this field is possible only with the development of scintillation technologies.

6. Conclusion

An analysis of the PIK reactor instrumental facility with regard to compliance of the neutron detectors with all the required operation parameters has been performed based on the information on detectors and strategic trends of their development in the leading neutron research centres of the world and analogous centres in Russia over the period of more than 60 years (40 years of past + "the current" period of the last 10 years + about the next 10 years of future). We have come to the conclusion that the global trends for the next 10 years of creation of new neutron detection technologies are developing in several main directions (they are arranged in priority order):

- Modernization and development of gas detectors based on ^{3}He neutron converters;
- Development of gas detectors based on ^{10}B solid converters;
- Development of scintillation detectors based on spectrum-shifting optical fibers;
- For specific cases another type of detectors, such as GEM, Micromegas, solid state semiconductor detectors and so on.

Despite the high price of ^{3}He, a global neutron community still considers gas-discharge ^{3}He-detectors to be the basic development direction, first of all, for the detectors with aperture of up to 1 m^2. The reason for this is a unique combination of such properties as high efficiency for neutron registration and low γ-background sensitivity.

A possible transition to different detection technologies based on ^{6}Li and ^{10}B converters, which are being currently developed in Europe, is mostly caused by necessity and has the aim to reduce the cost of devices by means of abandoning the use of ^{3}He in large and medium volume detectors with aperture from 1 to 80 m^2 and larger.

He-3 detection technologies. These technologies necessary for equipping the majority (about 70%) of experimental stations of the reactor PIK either exist at PNPI or can be produced there, as there is a technological capability for their development and realization. The aperture of these detectors does not exceed 1 m^2 and consequently they do not require a large amount of ^{3}He (about 900 l). ^{3}He is available in Russia, and its price is several times lower than that in Europe. For this reason, detectors based on ^{3}He is Russia's competitive advantage over Europe, which certainly should be used to the fullest extent.

Scintillation detection technologies. Groups of experts professionally working with scintillation detectors and having some interesting activities have been formed at PNPI, JINR and INR RAS. The greatest experience in development of large-area ZnS(Ag) scintillation detectors was accumulated by JINR (LNP). Several such detectors have been created there and are successfully put into operation at some Russian scientific centres. In order to succeed with any further activity in this area, it is necessary to join efforts of at least three Russian scientific centres, and it is reasonable to base this joint activity on the experience of JINR (LNP) developments.

To perform a detailed and thorough analysis of applicability of different detection technologies (today's and future) and to guarantee the best realization of its advantages, its competitive strengths in comparison with other neutron sources in Russia and abroad, it is important to organize a fruitful collaborations between PNPI and the world leading scientific centres such as: ESS (Sweden), ILL (France), FZ Jülich (Germany), J-PARC (Japan).

In the process of development of the neutron detector technique, it is necessary to apply widely the ideas and technologies developed for charged-particle detectors in high energy physics (and other research fields). It is necessary to strive for unification of the equipment used and ready-made technological solutions. It is also reasonable to develop a unified detection electronics for the detection systems, as well as electronics for data accumulation and processing. It is necessary to standardize interfaces and software at a lower level.

Acknowledgements

Special thanks for our collegues from JINR (Dubna, Russia) and from PNPI HEPD and NRD (Gatchina, Russia) for their fruitful discussions and assistance during preparation of this article.

References

1. K. Soyama, Basic Energy Sciences Neutron & Photon Detector Workshop (2012).
2. S. Peggs *et al*., European Spallation Source Conceptual Design Report, ESS-2012-001 (2012);
   S. Peggs *et al*., European Spallation Source Technical Design Report, ESS-2013-001 (2013);
   O. Kirstein *et al*., PoS (Vertex2014) 029 (2014), arXiv:1411.6194.
3. Int. Collab. on Neutron Detectors, http://icnd.org;
   K. Zeitelhack *et al*., Neutron News **23** (4), 10 (2012);
   T. Wilpert, Boron Trifluoride Detectors, Neutron News **23** (4), 14 (2012);
   B. Guerard *et al*., ^{10}B Multi-Grid Proportional Gas Counters for Large Area Thermal Neutron Detectors, Neutron News **23** (4), 20 (2012);
   N.J. Rhodes, Scintillation Detectors, Neutron News **23** (4), 26 (2012).
4. A. Krivshich *et al*., Reactor Complex PIK, Vol. II. Scientific Background for a Complex of Experimental Stations at the PIK Reactor, Detectors for the PIK Reactor Experimental Stations, 164 (2014).

PROTON ARM SPECTROMETER FOR THE R^{3}B SET-UP AT FAIR

G.D. Alkhazov, V.A. Andreev, V.L. Golovtsov, D.S. Ilyin, A.G. Inglessi, V.Yu. Ivanov, N.N. Filimonova, L.M. Kochenda, P.A. Kravtsov, A.G. Krivshich, D.A. Maysuzenko, A.V. Nadtochiy, I.N. Parchenko, S.S. Volkov, L.N. Uvarov, V.I. Yatsura

1. Introduction

The R^{3}B (reaction studies with relativistic radioactive beams) experimental facility for the study of reactions with relativistic radioactive beams is part of the FAIR project. The goal of the R^{3}B Collaboration is to develop and create a universal reaction set-up with high efficiency, acceptance and resolution for kinematically complete measurements of reactions with high-energy radioactive beams. The installation will be located in the focal plane of the high-energy branch of the super fragment separator (Super-FRS). The installation is adapted to the highest beam energies up to 1 GeV/nucleon provided by the Super-FRS, which ensures the maximum possible transmission of secondary beams. The R^{3}B facility will cover experimental studies of reactions with exotic nuclei that are far from stability, which will allow implementing a broad physical program with beams of rare isotopes with an emphasis on the structure and dynamics of nuclei. The work is carried out within the R^{3}B Collaboration, which includes more than 50 different institutes from around the world. To cover such a large physical program, several different tracking detection subsystems are provided (Fig. 1*a*). One of these systems will be a spectrometer for determining the momentum of emitted protons with energies up to E_p = 500–900 MeV. Unstable nuclear beams formed by the Super-FRS hit a secondary target, the reaction products being magnetically analysed with the superconducting magnet GSI large acceptance dipole (GLAD). Protons emitted in flight from excited fragments are bent in the GLAD and tracked using the dedicated proton arm spectrometer (PAS), which creation is the subject of responsibility of PNPI.

In 2016, the FAIR scientific council approved the PAS detector design and concept proposed by the Tracking Detector Department (TDD) of the HEPD [1]. The TDD proposal calls for the PAS facility to be based on thin-walled drift tubes (DT), which have a small material budget (X/X0 ≈ 0.05% per tube) and operate in vacuum. PAS will consist of four straw tube walls (STW), two walls for horizontal (X1&X2) and two walls for vertical (Y1&Y2) particle coordinate detection. A schematic arrangement of the PAS STWs, which are placed on a moving platform inside a vacuum chamber, is shown in Fig. 1*b*.

Each STW of the PAS will consist of three layers of straw tubes filled with a gas mixture at an overpressure of about 1 bar. The tubes are glued together, each layer being shifted by one tube radius with respect to the previous layer. In this way, for an orthogonal proton track, a lower detection efficiency close to the tube wall is always combined with a high efficiency in the centre of the straw in the following (staggered) layer. Also, the track's left/right ambiguity from the wire can be disentangled in the next layer.

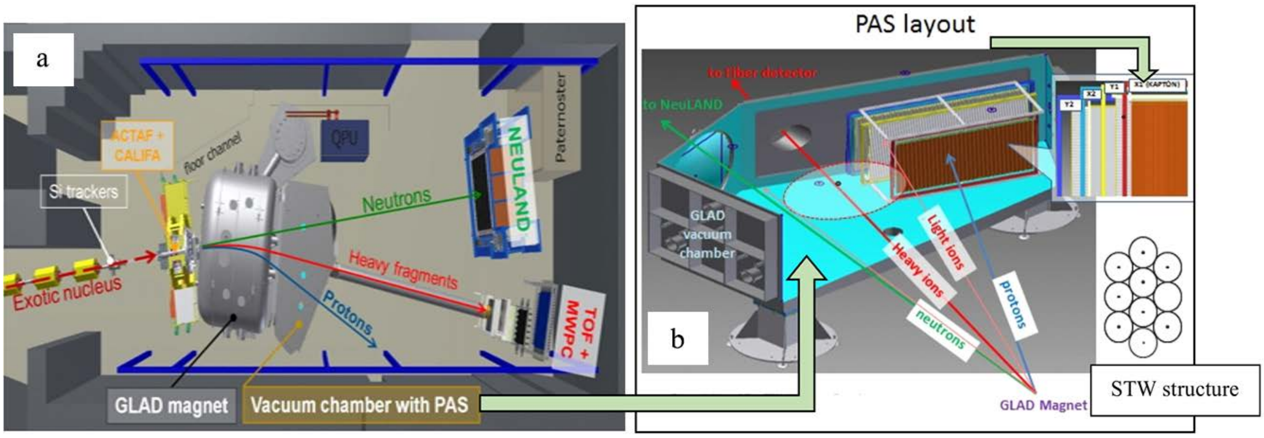

Fig. 1. R^{3}B set-up (*a*); proton arm spectrometer lay-out (*b*)

As follows from the technical requirements, the PAS installation must have a minimum amount of substance to ensure small angular straggling of the passing particles. First of all, this requirement applies to the first STW-X1. Therefore, it was decided to make this plane from Mylar tubes with a wall thickness of 60 µm, and the other three planes from ultrathin aluminum tubes with a wall thickness not exceeding 300 µm. Although the angular straggling caused by these tubes is larger compared to the thin Mylar tubes, their influence on the angular resolution is small since they are located near the end of the track.

The front-end electronics is placed in vacuum close to the straw-tube detectors for optimum performance in terms of noise. The PAS infrastructure, such as the gas supply, high-voltage (HV) and low-voltage (LV) power supply will be located outside the vacuum chamber. The technical requirements for the PAS spectrometer were discussed in more detail in the previous edition of HEPD Main Scientific Activities.

2. Drift tubes technology at Tracking Detector Department

A thorough search showed that there is no production of aluminum tubes with such parameters in Russia. A similar production was found in Switzerland and Germany, however, the minimum wall thickness of European pipes is 400 µm. As a result, the company MedSpetsTrub LLC was found, which agreed to develop and debug the necessary tube technology on the basis of its production. Within three years, with the direct participation of experts from the TDD, a technology was developed for the production of tubes from aluminum alloys AMg-5 and AMg-6 with a wall thickness of 220–240 µm [2].

Below are the main technical parameters of the tubes manufactured by this technology [3]:

- Inner diameter – 9.50–9.70 mm;
- Wall thickness – 0.22–0.24 mm;
- Uniformity of the inner surface $R_a \approx 0.32$ µm;
- Straightness of tubes is not worse than 150 µm per one metre of length;
- Tube material corresponds to aluminum alloy Amg-5;
- The tube leak is on the level of no worse than $5 \cdot 10^{-6}$ mbar · l/s.

On the basis of that technology, about 2 800 aluminum tubes (with a length of 2 750 mm) for the PAS spectrometer were manufactured. These tubes have passed through the output quality control (OQC) at the company (MedSpecTrub LLC) and the input quality control (IQC) at the TDD PNPI [2]. The mandatory incoming inspection of each tube included: visual inspection (the tube was rejected if any defects were found); mechanical machining of the tube ends; pressure steam washing; checking geometric parameters; checking the tube vacuum strength at overpressure of 4 bar.

After successfully passing through the IQC, the tube was cut out to the required length. Then this tube was used to manufacture the drift tube, which has its own procedure of certification including: gluing and checking of end pieces, leak test on a straw leak test station (SLTS) and HV tests with radioactive sources (^{55}Fe and ^{90}Sr) [3].

At the moment, about 1 400 drift tubes have passed through certification. Three prototypes and two working planes (STW-X2 and STW-Y2) for PAS were assembled from them. The gas leaks of these tubes did not exceed $2 \cdot 10^{-6}$ mbar · l/s, which is an order of magnitude better than required.

3. The choice of the gas mixture for proton arm spectrometer

This activity was based on GARFIELD simulations of the drift tubes. The operating characteristics of a gaseous detector are highly dependent on the gas mixture. One can select it for one or more of the following criteria: stability; low tendency to spurious discharges; good detection efficiency; high amplification; the drift velocity can be either slow (for good position measurement) or fast, for small dead time; non-flammability for safety; low diffusion for better time and space resolution; minimum aging effects for longer operational life of the detector.

As a result of Monte Carlo modeling of PAS drift tubes functioning in the GARFIELD program package, 70% Ar + 30% C_2H_6 was selected as a working gas mixture. It was used in tests of both prototypes and directly in the PAS STWs.

4. Proton arm spectrometer prototyping

These works were performed to test the PAS technology, to determine the diameter and length of the anode wire, to investigate the drift tube behaviour under different pressures (1–3 bar). Three prototypes were assembled and tested: prototype 1 (X2, length – 1 000 mm), prototype 2 (Y2, length – 2 500 mm) and prototype 3 (length – 300 mm).

Prototype 1. We have fabricated and tested the detector module, structurally corresponding to the STW-X2. This detector performance was studied at PNPI with a β-source ^{90}Sr and a photon source ^{55}Fe, as well as a high-energy (600 MeV/u) beam of carbon ions at GSI. The gas mixture Ar + 30% C_2H_6 was used. A general view of the prototype 1 and its location on a carbon beam at GSI is shown in Fig. 2*a*. The space structure of the beam and its halo were measured, the time spectra of the drift tubes were obtained, and algorithms for event selection were worked out [4, 5].

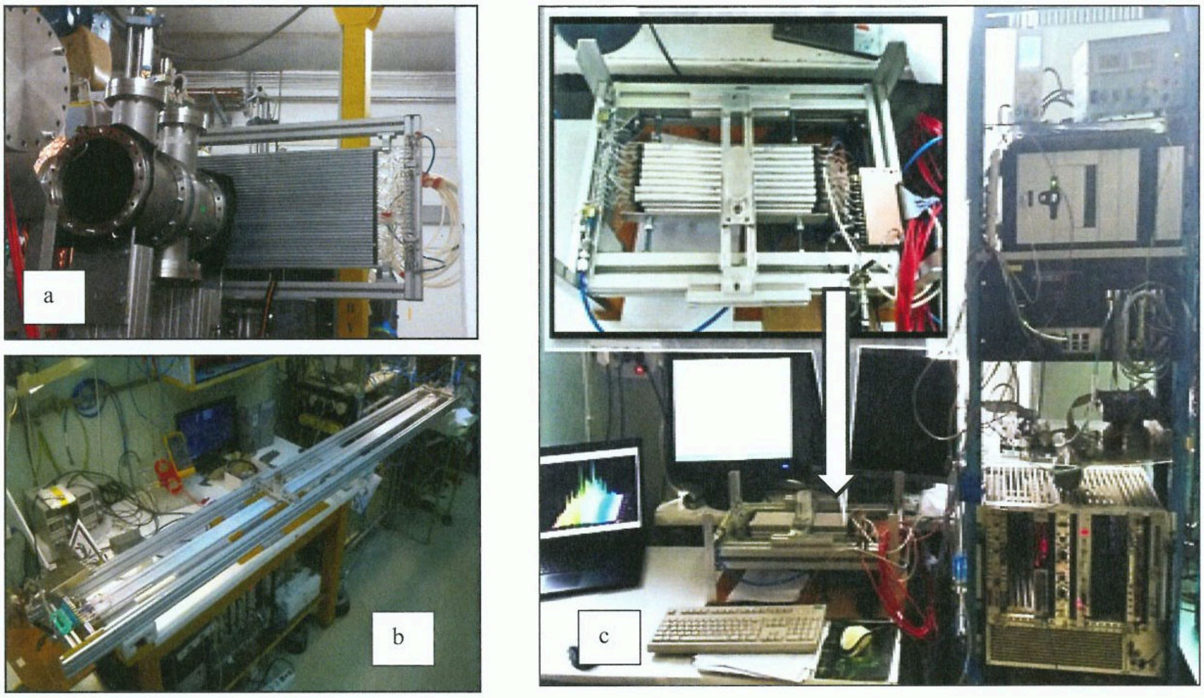

Fig. 2. Prototype 1 testing on a carbon beam at GSI (a); prototype 2 testing at PNPI (b); prototype 3 as a part of the proton arm spectrometer test station (*c*)

Prototype 2. We have fabricated and tested the detector module with the length *L* = 2 500 mm, which is larger than the tubes in the longest plane STW-Y2 (*L* = 2 180 mm). In addition, some of the drift tubes had anodes with different diameters – 30 and 35 µm with and without a special support. The operation of the detector with electronics was tested at a working gas pressure of 1–3 bar and different deformation of the drift tube [5].

Prototype 3. It was used to test the front-end electronics modules DT_ASD16 (amplifier / shaper / discriminator) and to study their interaction with the R^{3}B data acquisition system using a special test station (Fig. 2*c*). The test station includes: a time-code converter (CLK-TDC-128) with a control personal computer (PC) and an auxiliary module EXPLODER, four DT_ASD16 modules with a drift-tube unit, a server PC for remote operation with the test station, LV and HV power supplies (LVPS, HVPS).

Based on the results of our research, the following conclusions were made: the diameter of all PAS anodes will be the same and equal to 35 µm; the anodes of the drift tubes work confidently without special supports at pressures of 1–3 bar; the allowable deformation of the tubes is 300 µm [5].

5. Construction and testing of X2 and Y2 planes

A general view of the X2 and Y2 planes is shown in Fig. 3. (Note that in this paper we use symbols ST wall and ST plane, which are identical to each other.) In the upper right corner of the plane X2 one can see preamplifiers (two preamplifiers on each side) which are mounted on both sides of the frame.

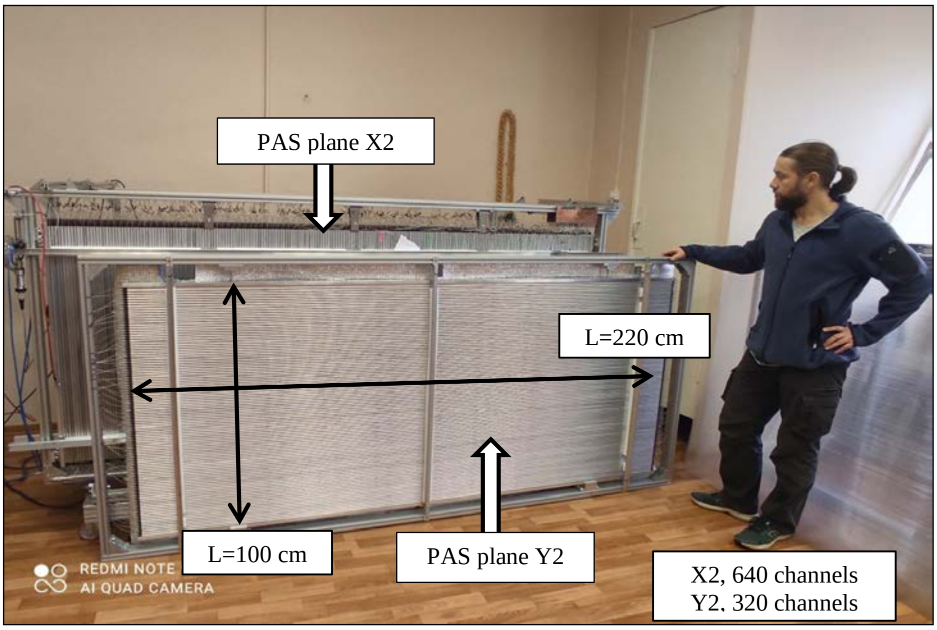

Fig. 3. General view of two proton arm spectrometer planes (X2 and Y2)

All drift tubes were tested for the vacuum leak (Fig. 4*a*) and after that their current and counting characteristics were measured. The tubes selected in this way were glued together in three layers by a specially developed technology and placed in a frame for the PAS spectrometer. The distance between the drift tubes for each of the planes was measured and shown in Fig. 4*b*. It is seen that the absolute position of these tubes in space has no deviation, and the accuracy of their positioning will be 10 250 ± 30 µm, which is 2 times better than the technical requirements.

The vacuum leak was measured independently for each drift tube and plane. Since we do not have a vacuum chamber of sufficiently large dimensions, the gas leak rates were tested at a pressure much higher than the atmospheric pressure (not less than 2 bar). As a result, the gas leakage rates were tested at the following gas pressures:

- Hydrotesting of drift tubes P = 4 bar;
- Gas tests of drift tubes P = 3 bar;
- Gas tests of the plane from drift tubes P = 2 bar.

The pressure and temperature in the planes were recorded during seven days. The data obtained for the X2 and Y2 planes are shown in Fig. 4*c*. The temperature was practically constant in the range 22–25°, and so the density of the gas inside the tubes depended only on the behaviour of the pressure. As one can see, the pressure dropped down from 2 to 1.1 bar in X2 during (74 – 16) / 24 h = 2.4 days and in Y2 during (135 – 28) / 24 h = 4.5 days. These are upper estimates! The obtained data on the leak level in the planes differed by a factor of about two, which corresponded to the number of drift tubes in the X2 and Y2 planes. This allows us to state that the gas leaks in the planes are mainly associated with the gas connections between the tubes, and they are rather small.

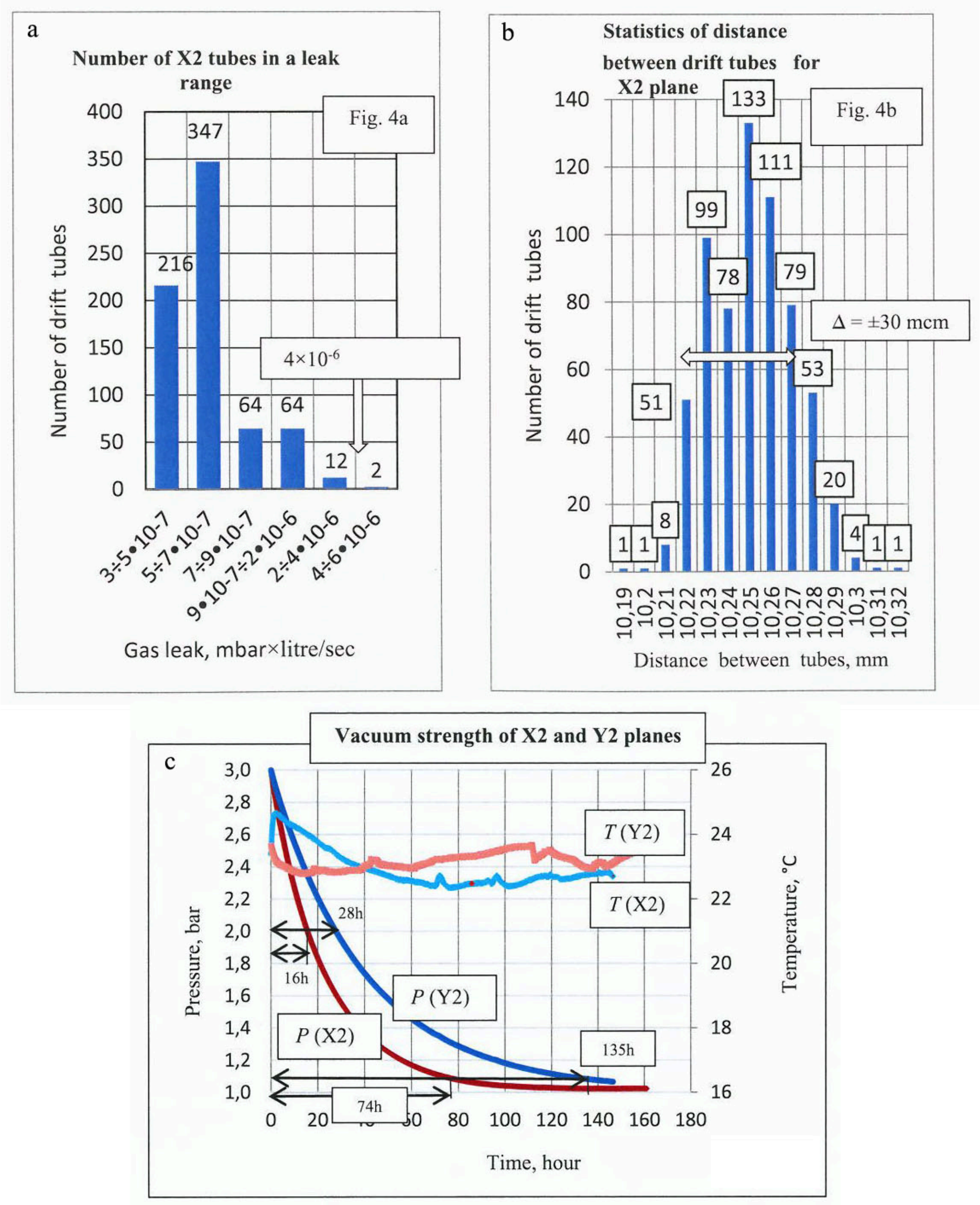

Fig. 4. Number of X2 tubes in a leak range (*a*); statistics of distance between drift tubes in STW-X2 (*b*); plane's pressure and temperature time behaviours (*c*)

6. The straw leak

To investigate the straw leakage, two methods were used by us. The first method was implemented on the basis of the straw leak test station (SLTS, Fig. 5) and answered the question of the gas leakage rate into vacuum. It had high sensitivity and allowed us to select drift tubes with small leakage. The second method was based on the behaviour of the tube in water. It had a slightly lower sensitivity, but it allowed to accurately spot the place where the leak occurred. By combining both methods, it was possible to efficiently select drift tubes with no leakage to vacuum under an absolute pressure of 4.0 bar. We worked with tubes leaking up to $4 \cdot 10^{-6}$ mbar · l/s.

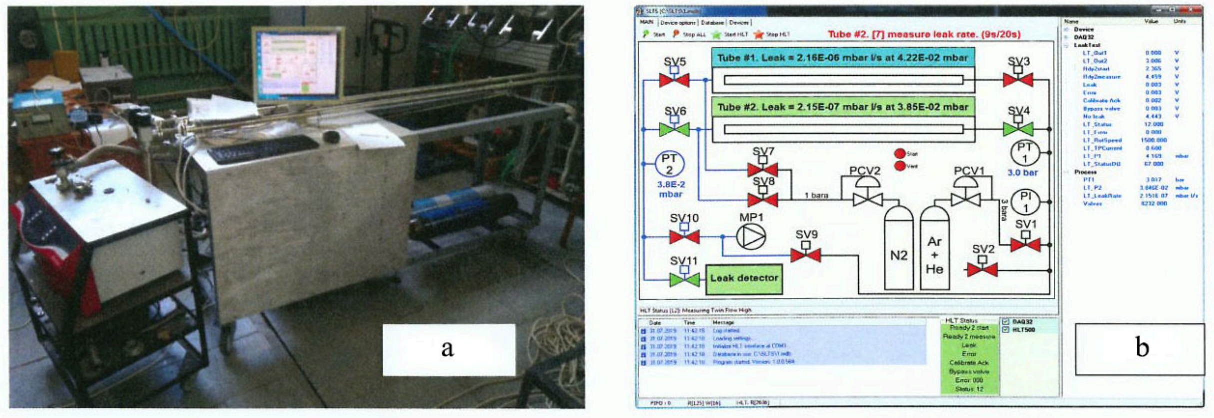

Fig. 5. Straw leak test station (*a*); straw leak test station software main window (*b*)

The main task of the SLTS was to measure the leak rates from the straw drift tubes into vacuum. The parameters of the system are listed below: the leak rate sensitivity – ~ $1 \cdot 10^{-8}$ mbar · l/s; the straw working gas mixture – Ar + 8% He; the absolute pressure range was 0.5–5.0 bar; the maximum straw length was 3 m. The system was mounted in a special bench with two vacuum cartridges and a control console on top of the bench. All valves, a vacuum pump and gas cylinders were located inside the bench.

7. Proton arm spectrometer gas supply system

The main task of the gas system (Fig. 6*a*) is to provide a pure (70% Ar + 30% C_2H_6) mixture to the PAS detector at the chosen operating pressure. The gas supply system works in flushing mode, with the total flow rate of up to 4 litres per minute. The absolute pressure in the straw tube walls is stabilized in the range 1–3 bar with ~ 1% accuracy. The oxygen and moisture concentration in the mixture is kept at the 5 ppm level.

The wiring of the control and gas panels was finished. All sensors and control devices were checked. The control software of the gas system is shown in Fig. 6*b*. The software package consists of the main control program, the CHARTS program for online parameters visualization, the DBVIEWER program for handling the databases with the gas system parameters. The pressure stabilization in X1 plane (PT4) and in X2, Y1, Y2 planes (PT5) is shown in Fig. 6*c*.

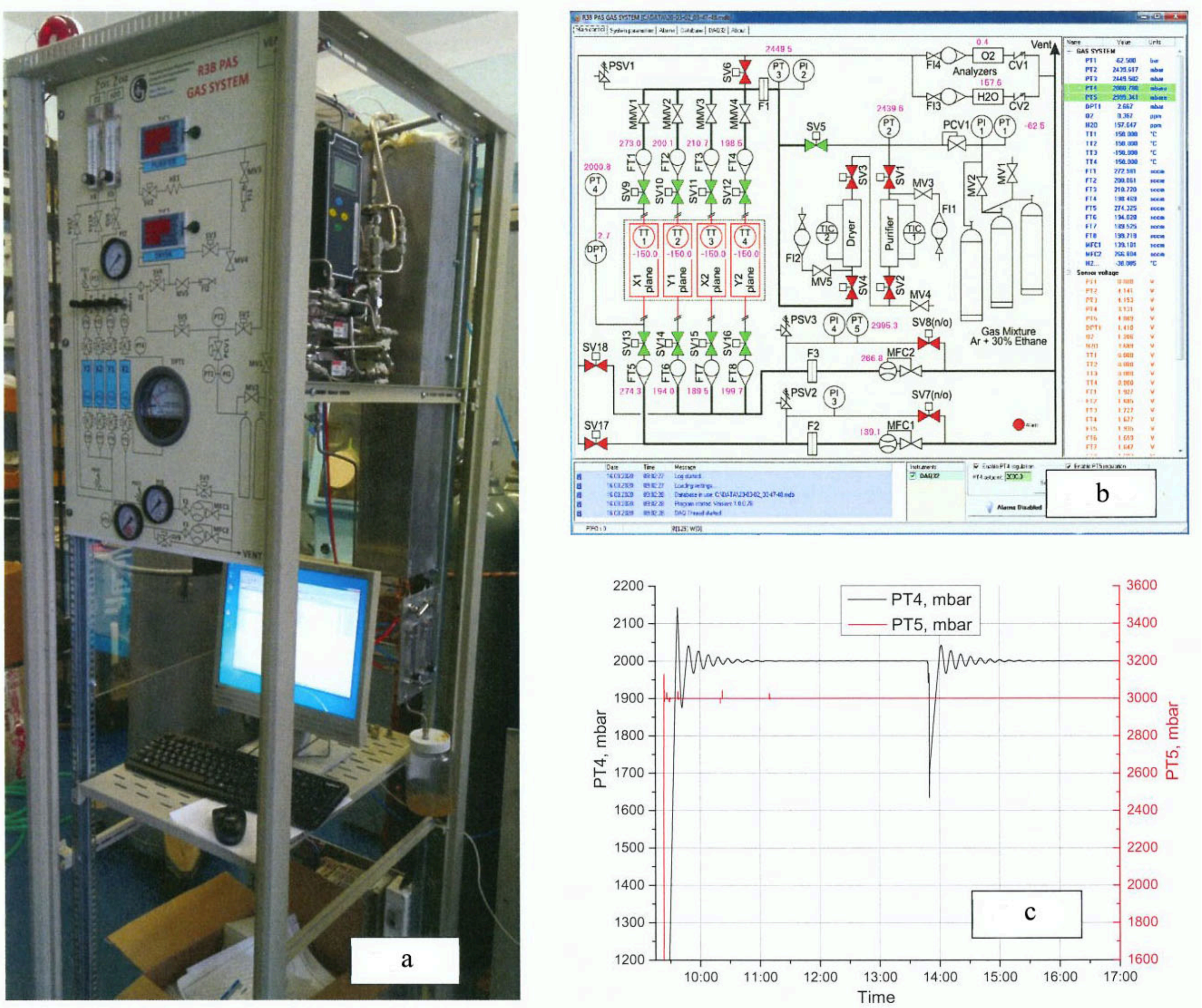

Fig. 6. Proton arm spectrometer gas supply system appearance (*a*) and system software main window (*b*); pressure stabilization in X1 plane (PT4) and in X2, Y1, Y2 planes (PT5) (*c*)

The pressure histogram for the X1 plane was measured during the stable operation of the system. The standard deviation of the pressure was only 0.22 mbar at the total pressure of 1999.99 mbar, so the stability is about 0.01%. This is very good, but should be checked again with the real detector planes. The gas system is ready to operate with the detector planes.

8. Front-end electronics

The Radio Electronics Department (RED) of the HEPD has developed a version of the front-end electronics that combines an amplifier, a shaper and a discriminator on one 16-channel DT_ASD16 card (amplifier, shaper, discriminator), see Fig. 7*a*–*c*. Its specification is in the Table. These cards are located directly on the STW frame in vacuum. The DT_ASD16 card is optimized to work with straw tubes manufactured by PNPI and has an output connector compatible with the CLK-TDC-128 digitizing module of the data acquisition system. These modules are produced at GSI.

The LVPS has a LV switchboard (not shown in Fig. 7*a*) located on the STW frame to supply power to each DT_ASD16 *via* a separate 3.8–4.5 V wire. (This is LV IN, see Fig. 7*a*.) Low dropout voltage regulators (LDOs) provide a nominal 3.3 V (LV OUT) voltage to power on-board circuits. LV switchboard combines up to 20 DT_ASD16 cards per one LVPS.

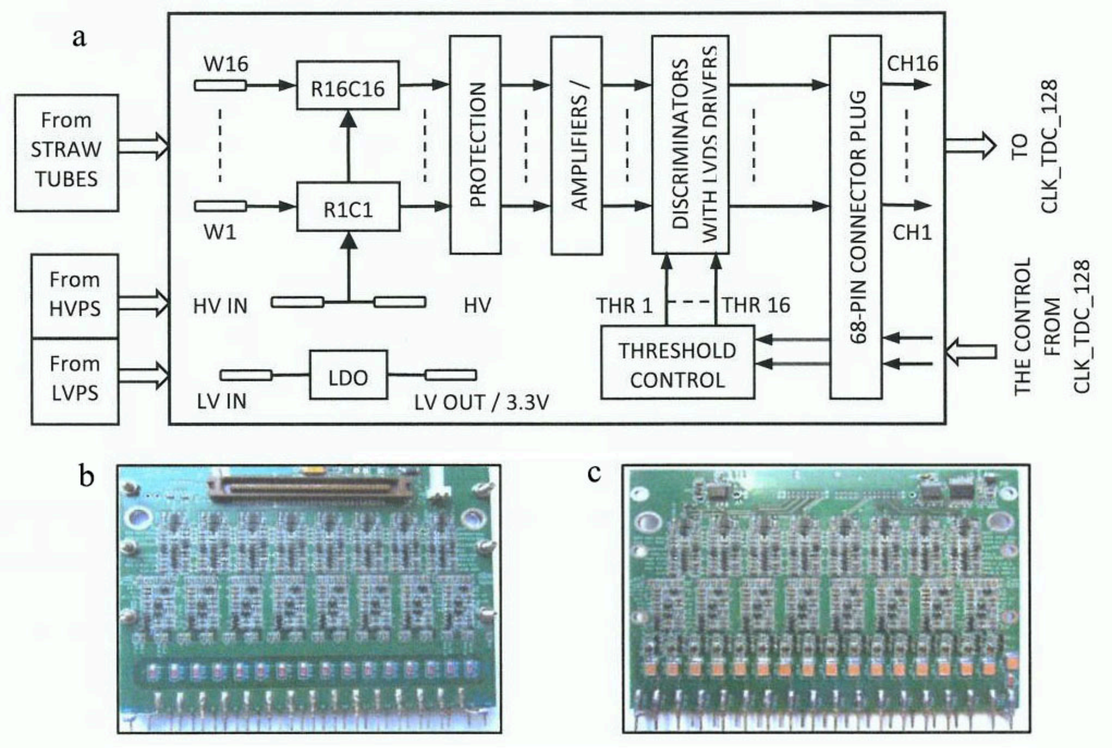

Fig. 7. DT_ASD16: *a* – block diagram; *b* – top view; *c* – bottom view

Table

DT_ASD16 specification

Parameter	Value
Board size	105 × 84 mm^2
Input	Charge sensitive
Input impedance	260 Ohm
Gain	5.4 mV/fC
Shaping	8.5 ns
Threshold control	Per channel
Supply Voltage	3.8–4.5 V
Output standard	Low voltage distribution system
Internal noise	2 fC
Double pulse resolution	100 ns
Output connector	68-pin 1.27 mm pitch low profile plug (by KEL Corporation)
Current consumption per card	240 mA

The HVPS comes from a HV switchboard (not shown in Fig. 7*a*), also located on the STW frame. The DT_ASD16 distributes the high voltage from the HV IN pin to each straw wire (W1… W16). The HV OUT pin allows multiple DT_ASD16 boards to be connected in series, allowing more straws to be powered per HV channel.

Placing the DT_ASD16 cards on both sides of the frame made it possible to achieve two important things: firstly, to minimize the couplings between the amplifier inputs and drift tubes, and secondly, to ensure efficient removal of the generated heat from the electronics, which should operate in vacuum. The measured temperature of the hottest elements on the DT_ASD16 card does not exceed 45°C, which should ensure long-term stable operation in vacuum without active cooling.

Up to eight DT_ASD16 cards are connected to one CLK-TDC-128 module, also located in vacuum on the inner wall of the vacuum chamber, which allows minimizing the length of the connecting flat cables to 6 m. Individual thresholds in each DT_ASD16 channel allow to compensate gain fluctuations in tubes and are set *via* the CLK-TDC-128 module.

All DT_ASD16 cards were tuned and quality controlled on the set-up shown in Fig. 8*a*. The LVPS of the preamplifiers was carried out from standard power supplies. The HVPS of the drift tubes was carried out through the preamplifier board by power sources developed in the RED. The modules of this power supply (HVCD MASTER and DB50) are shown in Fig. 8*b*.

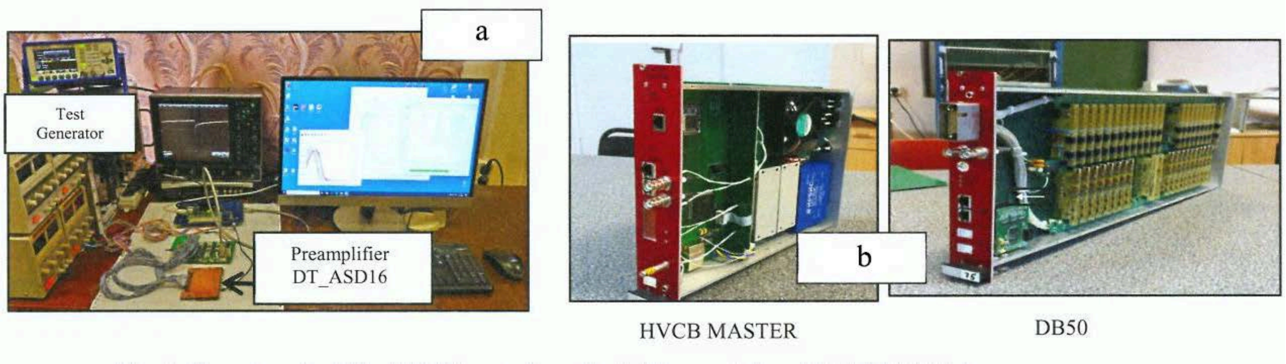

Fig. 8. The set-up for DT_ASD16 tests of quality (*a*); the modules of HVDS1600 (*b*)

The development of the HVPS HVDS1600 (high voltage distribution system) was performed in the RED in accordance with the parameters of the required technical specifications [6].

Tests of four DT_ASD16 modules at a test bench and a test station with the CLK-TDC_128 module showed that their characteristics comply with the technical specifications (Fig. 9). As a result, this version represents the final technical solution DT_ASD16 for PAS, which will be put into serial production.

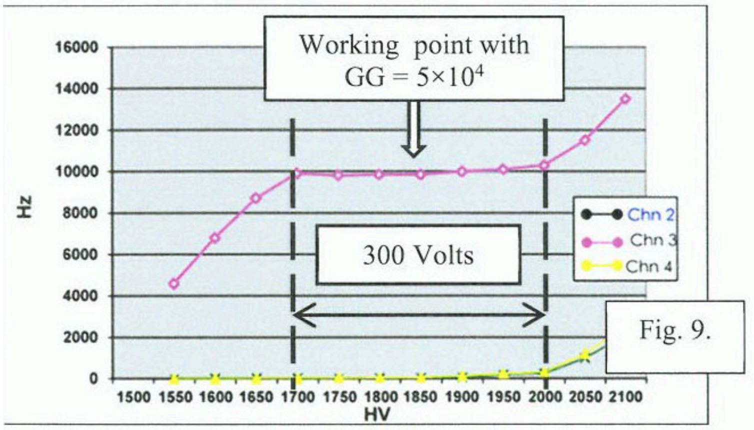

Fig. 9. The counting rate versus high voltage from ^{90}Sr source for different channels of DT_ASD16

The results of testing of four DT_ASD16 modules are presented below. The following parameters are ensured, which cover the entire range of lengths of the drift tubes (0.3–2.2 m) for PAS:

- The counting rate plateau is in the range of 1 700–2 000 V;
- The operating point is at 1 850 V, which corresponds to the gas gain (GG) factor of GG = $5 \cdot 10^4$;
- The measured cross couplings within the plateau do not exceed 2.0%.

Currently, four DT_ASD16 modules are installed on the system test station and demonstrate stable operation with the CLK-TDC-128 module. These modules are reference ones and will be used for product tests during serial production. The threshold control is also provided by the CLK-TDC-128 module; thus no special threshold control unit is required.

9. Conclusion

1. The manufacturing technology of the PAS spectrometer based on long drift tubes with ultrathin walls for vacuum operation has been developed at PNPI.

2. The PAS spectrometer is in a high state of readiness:
   - The plane X2 is ready for work;
   - The plane Y2 is already done and ready to be equipped with electronics;
   - The plane Y1 is in the process of being assembled;
   - The plane X1 will be made from Mylar drift tubes. This technology has been developed at PNPI. The tubes for this plane were ordered in England, delivered to GSI and are ready to be sent to PNPI.

References

1. Technical Report for the Design, Construction, and Commissioning of Tracking Detectors for R^3B, 101–117 (2014).
2. V.A. Andreev, M.I. Gasanov *et al.*, Preprint NRC “Kurchatov Institute” – PNPI 3052 (2021).
3. V.A. Andreev, V.Yu. Ivanov *et al.*, Preprint NRC “Kurchatov Institute” – PNPI 3059 (2021).
4. A.G. Krivshich *et al.*, Preliminary Results of the PAS Prototype Test with a ^{12}C Beam: GSI Scientific Report 2016, 217 (2017). DOI:10.15120/GR-2017-1.
5. A.G. Krivshich, V.A. Andreev *et al.*, Preprint NRC “Kurchatov Institute” – PNPI 3062 (2022).
6. A.A. Fetisov, A.G. Krivshich, D.A. Maisuzenko, in *Contract Between FAIR and PNPI: Technical Specifications*, 1–7 (2018).

HIGH VOLTAGE POWER SUPPLY FOR THE PROTON ARM SPECTROMETER OF THE R^{3}B EXPERIMENT AT FAIR

S.V. Bondarev, V.L Golovtsov, N.V. Gruzinsky, N.B. Isaev, E.A. Lobachev, L.N. Uvarov, V.I. Yatsyura, S.S. Volkov

The design and construction of the high voltage power supply (HVPS) for the proton arm spectrometer (PAS) at FAIR further developed the ideas implemented in the design and construction of the high voltage distribution system (HVDS) for photomultiplier tubes (PMTs) for the new large-area neutron detector (NeuLAND) described in Ref. [1].

PAS [2, 3] consists of four straw-tube walls (STW), two pairs of which are either horizontal or vertical. The first STW (X1) is made of thin-walled Kapton (or Mylar) tubes. The remaining three STWs (Y1, X2, Y2) are made of aluminum tubes with a wall thickness of about 300 µm. Straw tubes require a higher input voltage but draw less current than PMTs. Each HVDS channel feeds one PMT, whereas each HVPS channel serves an array of 48 straws. Thus, the total number of high voltage (HV) channels for PAS is about 40 (with a total number of straws less than 2 000), while the total number of HV channels for NeuLAND is 6 000.

HVPS for PAS consists of two modules: high voltage control board – master (HVCB–MASTER) and distributor board (DB50), Fig. 1.

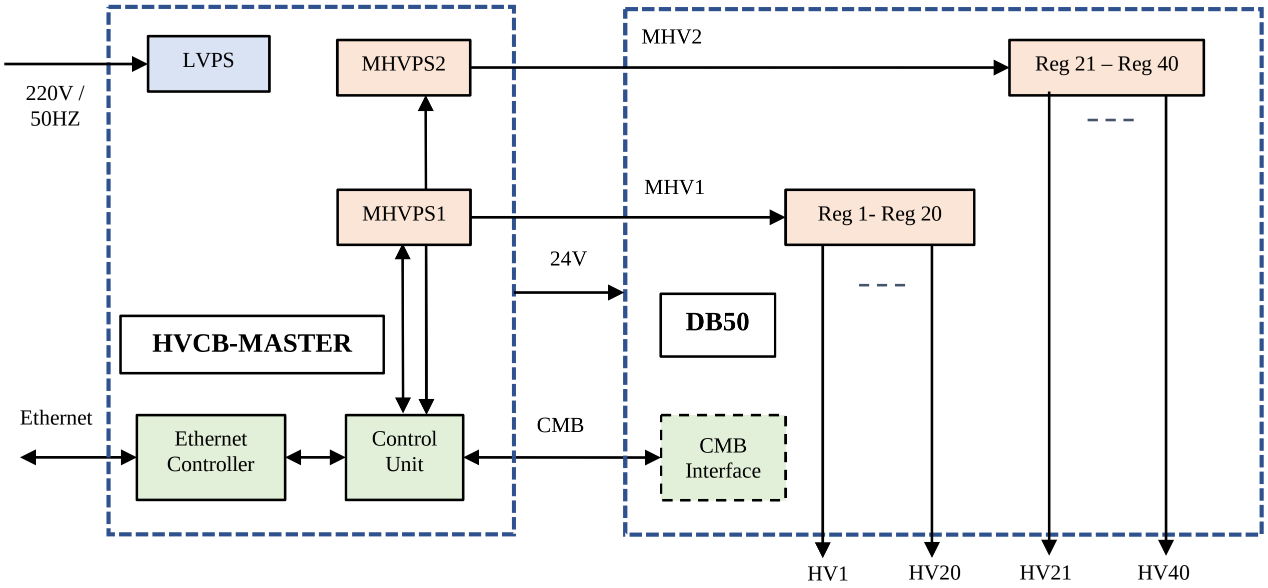

Fig. 1. High voltage power supply block diagram

HVCB–MASTER integrates in one module:

- Two Master HVPS (MHVPS1 and MHVPS2) based on the Spellman UM4P30/E 4 kV / 7.5 mA module;
- HVCB, which provides communication with the main computer and performs setting and monitoring of voltages and currents in MHVPSs and DB50 regulators;
- Low voltage power supply (LVPS, 24 V) for DB50 and itself.

The DB50 is a modified module originally designed for HVDS, containing HV regulators individually adjustable for each channel. Firstly, the two previously jumpered HV connectors are now separated, with each connector feeding exactly half of the regulators. Secondly, only 40 slots for the regulators are populated with modified 3 kV plug-in cards, since PAS requires only 40 HV channels.

The control and monitor bus (CMB) is a serial link between modules over an Ethernet patch cord with RJ45 connectors. HV cables with save HV (SHV) connectors carry the master HV (MHV) from the HVCB–MASTER to the DB50.

The HVCB–MASTER provides a 100 Mbps Ethernet connection to the host computer. The host software allows one to download required voltage setting and read back voltage and current monitor values to / from the buffer memory of the control unit (CU). The finite state machine (FSM) in the CU field programmable gate array communicates directly with the MHVPSs in the HVCB–MASTER and *via* the CMB with the regulators in the DB50. The CMB interface on the DB50 converts serial CU commands and monitoring data back and forth. Every 20 ms, the FSM updates the voltage set values from the buffer memory to the MHVPS / regulators and the voltage and current monitor values from the MHVPS / regulators to the buffer memory. In this way, the host computer can promptly process trip conditions in the straw tubes.

The main system parameters are as follows:

- Control range of a single channel – 0 to 3.0 kV;
- Voltage setting and monitor step – 2 V;
- Output current, max – 240 μA;
- Current monitor step, min (non-linear scale) – 0.1 μA;
- Current trip level – under software control;
- Voltage ramp up and down rate – under software control.

HVPS modules are shown in Fig. 2*a*–*c*.

Fig. 2. Module: *a* – HVCB–MASTER; *b* – DB50; *c* – HVPS

The host computer runs software developed within the visual components library for Windows of the Delphi integrated development environment (IDE) to manage and monitor the HVPS. Delphi IDE uses the Delphi dialect of the Object Pascal programming language. New application libraries have been developed. The software has a friendly and intuitive graphical user interface. The software is described in detail in the “HVPS-40 Operating Manual”.

References

1. G.D. Alkhazov *et al.*, PNPI. High Energy Physics Division. Main Scientific Activities 2013–2018, 377–378 (2019).
2. G.D. Alkhazov, V.A. Andreev, A.V. Dobrovolsky *et al*., PNPI in the R^3B Project at FAIR, This Vol.
3. A.A. Fetisov, A.G. Krivshich, D.A. Maisuzenko, Description of the High Voltage System for the PAS R^3B Detector: Technical Design Report, 7 (2018).

COMPREHENSIVE STUDY OF A PROPORTIONAL CHAMBER CATHODE'S SURFACE AFTER ITS OPERATION IN AN EXPERIMENT AT THE LARGE HADRON COLLIDER

G.E. Gavrilov, A.A. Dzyuba, O.E. Maev

1. Introduction

Radiation resistance of multiwire proportional chambers (MWPCs) in experiments at the Large Hadron Collider (LHC) remains a hot topic, due to the recent tenfold increase in the luminosity of the collider after its upgrading. The key motivation for this research is to maintain the stability of MWPCs for the next 10 years of the LHC operation with an expected jump in the ionization current and the already observed spontaneous self-sustaining current – Malter effect (ME) [1]. Spontaneous currents arising in MWPCs are ten times higher than the current from collisions of the proton beams in the collider and reach up to 30–40 μA [2]. This complicates operation of the readout electronics and overloads it with false responses. The ME current localized at a point on the cathode as well accelerates the aging of the anode wires located nearby.

It should be noted that the main source of the background in the muon detector of the LHCb experiment are fast neutrons with energies of up to several hundred MeV. They form photons with energies of 0.1–1 MeV as a result of nuclear interaction with the structural materials of the facility. Compton electrons are generated when photons pass through the gas volume of the MWPC, and their energy exceeds the threshold of the formation of radiation defects in metals ~ 0.5 MeV [3, 4].

The aim of studying the surface of the cathode of the MWPC was to determine the cause of ME currents in order to develop non-invasive ways of suppressing them.

2. Experiment

A module of the MWPCs of the muon detector of the LHCb experiment (type M5R4_FIR037), which operated at the LHC ($T \approx 3.2 \cdot 10^7$ s), was chosen for the study [2]. This module consists of four detecting planes (Gaps A, B, C and D) of MWPCs, and only Gap D's plane regularly displays spontaneous self-sustaining currents. It was from this plane that cathode samples were taken (disks 1 mm thick with radius of 23 mm).

As a result of the LHC operation with a working gas mixture of Ar 40% / CO_2 55% / CF_4 5%, the MWPC anode wires in the M5R4_FIR037 module accumulated charges of $Q \approx 1$ mC · cm^{-1} (or ~ 2.5 mC · cm^{-2}). After the module was dismantled from the muon detector, it was additionally studied at the gamma irradiation facility (GIF++) [5] using an Ar 40% / CO_2 58% / CF_4 2% gas mixture. As a result, a charge of $Q_1 \approx 0.5$ mC · cm^{-1} was additionally accumulated on the wires.

It should be noted that the charge Q_1 accumulated in a very short time (the current of the MWPC detecting planes was two orders of magnitude higher than that during operation as a part of the muon detector). The CF_4 content in the working mixture was 2% and the gas flow through the volume was reduced by 30%. Despite the tougher testing conditions, there were no new zones of spontaneous electron emission in the MWPCs. The already existing ME zone remained in its original place.

High voltage was not applied to one of the MWPC planes (Gap A) during operation on the collider (and at the facility). Like its counterparts, however, this plane was exposed to charged particles with an intensity of $R \approx 350$ Hz · cm^{-2}. Since there was no electric field, the cathodes in the Gap A plane were not exposed to the plasma chemical effect of products of the dissociation of the gas mixture's components. The samples taken on this plane are therefore referred to below as control samples. They were compared to samples from the Gap D plane, which had experienced the entire set of radiation and plasma chemical effects. The characteristic fluence of minimum ionizing particles for the MWPC planes was $F \approx 5 \cdot 10^{13}$ cm^{-2}. The dose on the copper foil of the cathode (35 μm thick), calculated using the GEANT4 software package, was thus at a level of $D \approx 1.3$ Gy.

The count rates of Gap D anode wires combined into groups were measured to localize the zone of the ME current generation in the MWPCs during irradiation at the GIF++ facility. The zone of generation was therefore found as a group of wires with a very high count rate. Here and below, the cathode samples taken along these wires are referred to as ME samples, while those taken outside the zone of the high count rate are non-ME samples.

Figure 1 (*upper part*) shows photographs of the M5R4_FIR037 cathode planes after disassembly. Photos of the Gap A and Gap D planes are on the left. The layout of the samples on the cathode is on the right. ME samples were taken in series along the Y axis (30 cm long) parallel to the anode wires with the highest count rate. Non-ME samples were also taken along the Y axis, but were offset by ~ 20 cm from the zone of spontaneous currents. Visual inspection of the MWPC module after disassembly showed that the cathodes of all the MWPC planes, except for the Gap A plane, were strongly oxidized (the *lower photo* of Fig. 1). However, since the ME was observed only on the Gap D plane, we can assume that the oxidation and reduction of copper are still not sufficient reasons for the emission currents on the cathode [6, 7], although it is known, that the island oxidation of copper surface with the formation of Cu_2O often leads to the emission currents in an electric field of $E \geq 50$ kV · cm^{-1} [8].

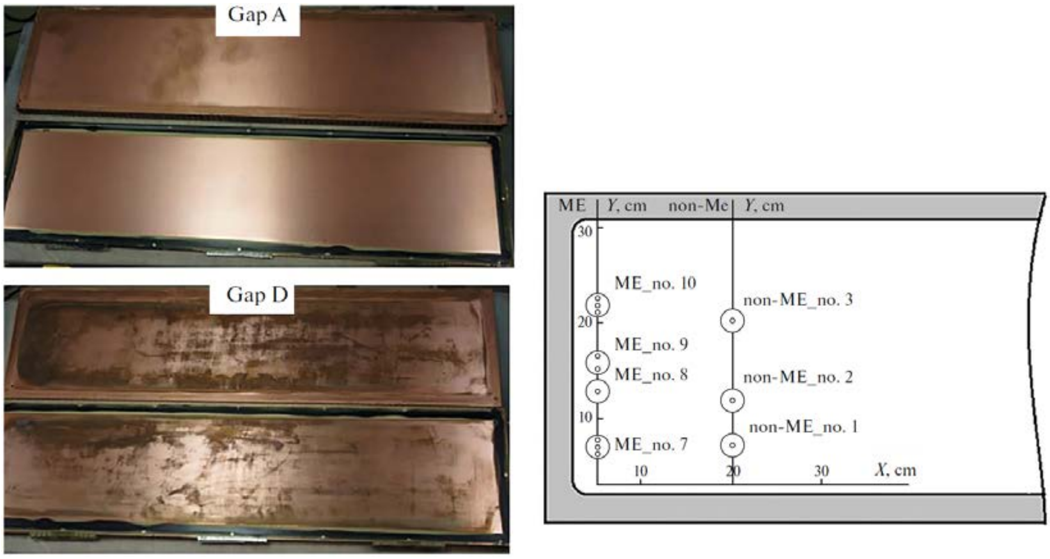

Fig. 1. Photos of the cathode planes Gap A and Gap D after the disassembly of the MWPC (*left*); the arrangement of samples (*dots*) on the cathode (*right*)

The surface morphology of the cathode samples was studied by atomic force microscopy (AFM) with Solver Next scanning probe microscope (OAO NT-MDT, Zelenograd, Russia). Surfaces were scanned by NSG10/TiN cantilevers in the tapping (topography and phase) and contact (current spectroscopy at air under normal conditions) modes. Elemental analysis of the samples surfaces was performed *via* Rutherford backscattering spectroscopy (RBS) on the Mikrozond component of the Mikrozond-EGP-10 complex at a beam energy of 4 MeV, a proton current 0.01 nA on the samples, and a beam size of 30 × 30 μm^2. The scanning area was 300 × 300 μm^2. The phase composition of samples was determined using a Shimadzu XRD-7000 X-ray diffractometer and copper anode radiation (wavelength, 1.542 A), $V = 40$ kV, $I = 30$ mA.

The composition of microparticles and microstructured objects was analysed *via* Raman spectroscopy. A RamMics M532R Raman microscope was used that combined the capabilities of an EnSpectr R532R Scientific Edition Raman analyser and an Olympus CX-41 microscope.

3. Results and discussion

An analysis of the surface structure of samples taken from different sections of the cathode in the Gap D plane showed the nonuniformity of the radiation aging processes. Figure 2*a* (*upper part*) shows a scan of the surface of a control sample (Gap A plane). Figures 2*b*, *c* show scans of no-ME samples 2 and 3 (Gap D plane). The surface of the control sample has a weakly structured fibrous relief with zones of disorder (technological defects) and single peaks. Primary defects most likely were formed on the cathode when bonding copper foils to fiberglass plates during production.

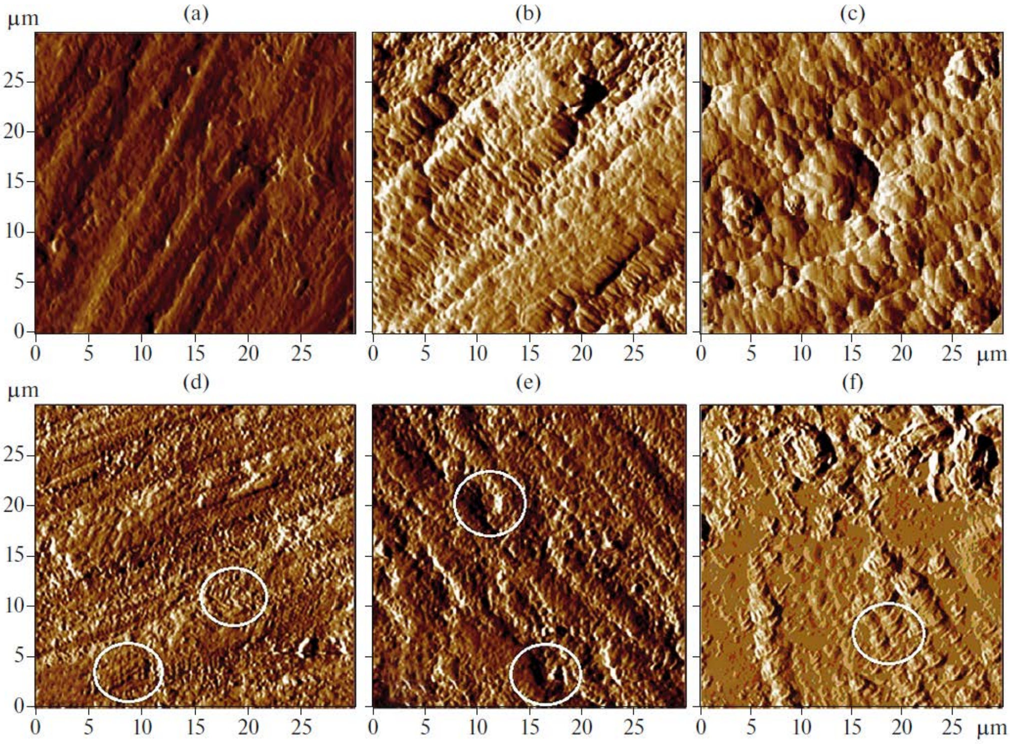

Fig. 2. Atomic force microscopy scan of the sample surface with a scanning field size of 30 × 30 μm^2: *a* – control sample; *b* – non-ME 1; *c* – non-ME 2; *d* – ME 5; *e* – ME 8; *f* – ME 10

In addition to radiation, the surfaces of ME and non-ME samples were exposed to products of the dissociative ionization of gas molecules ($\mathrm{O}^{\bullet}$, $\mathrm{F}^{\bullet}$, $\mathrm{CF}_n^{\bullet}$ and $\mathrm{CO}^{\bullet}$ radicals, where $^{\bullet}$ is the number of not coupled electrons of the outer shell) in vicinity of the anode wires of the MWPC [9]. Thus, a different morphological type of surface (terraced structures with isolated cells) was formed on the cathodes than on the control sample. As can be seen in Figs. 2*b*, *c*, non-ME samples were characterized by zones of segregation in addition to terraced structures.

Figures 2*d*–*f* (*lower parts*) show AFM scans of ME samples 5, 8 and 10. Most of their surface areas were subjected to erosion. Common to these samples are terraced structures similar to those found in non-ME samples (marked with white ovals in Figs. 2*d*–*f*). Changes in the surface morphology of ME samples were due to such radiation defects as blisters, craters, and finely dispersed structures characteristic of copper oxide Cu_2O. These structures are clearly visible in Figs. 2*d*, *e*. Both the foamy areas on the surface (see Fig. 2*d*) due to small blisters and the formation of craters caused by radiation (see Fig. 2*e*) do not have melting zones.

Zones of structural phase transitions (oxidation and melting) are clearly visible in Fig. 2*f*. The observed smoothing due to melting is distributed over image area of 30 × 30 μm^2, due apparently to the thermal action of high-density emission currents on the cathode copper foil. Surface melting can also occur in the copper foil along the trajectories of fast charged particles, which cause cascades and subcascades of moving vacancies and interstitial atoms. However, such effects at a relatively low intensity of irradiation ($R \approx 350$ Hz · cm^{-2}) should be point-localized [10].

At the same time, due to absorption by copper from the gas mixture of molecules containing oxygen, carbon and fluorine, the islands of dielectric oxide Cu_2O grow [2, 8] and nanocarbon and fluorocarbon films form [11, 12] on the cathode surface. The point emission of electrons is possible for such formations under the action of an electric field, which can heat their surfaces to the melting point. The inhomogeneity of the distribution of emission points on the cathode could be due to the turbulence of the gas flow in the narrow gaps of the MWPC (5 mm) near the inlet and outlet of the gas mixture [2].

Figure 3 presents results of an analysis of the main characteristics of the surfaces of samples (roughness S and peak height differences Δh, both in nm). Data for four ME samples and three non-ME samples are given that depend on their coordinates along the Y axis. The surfaces of ME samples 7, 9 and 10 ($Y \approx 6$ cm, $Y \approx 15$ cm and $Y \approx 32$ cm, respectively) were examined at several points.

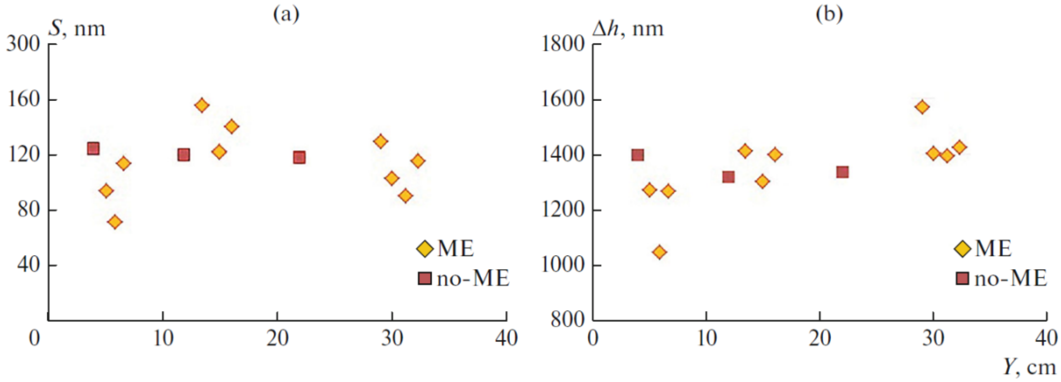

Fig. 3. Distribution of (*a*) roughness S and (*b*) peak heights Δh on the surface of ME samples and non-ME samples along the Y axes in and outside the zone of spontaneous currents

The roughness of the control sample surface was $S \approx 90$–100 nm, and the difference between peak heights at different points was $\Delta h \approx 1\,100$–$1\,200$ nm, very close to the values in Fig. 3. The surface is rougher than that on the control sample in the zones on the Gap D plane, regardless of electron emission. The roughness varies in the range of $S \approx 100$–140 nm, and the difference between peak heights varies in the range of $\Delta h \approx 1\,300$–$1\,450$ nm. This is apparently due to the plasma-chemical and radiation effects on the copper foils, which usually oxidizes the boundaries of crystallites and remove material from the surface [6].

Only the surface of ME sample seven is characterized by notable smoothing (see Fig. 1, $Y \approx 6$ cm) where the roughness and height of the peaks fall pointwise to $S \approx 70$–100 nm and $\Delta h \approx 1\,000$–$1\,250$ nm, becoming comparable to the control sample. Electrons were apparently emitted precisely in the region where ME sample seven was taken. They heated the foil to the melting temperature locally and burned out peaks formed by radiation erosion [11, 12]. Analysis of the pore space of ME sample seven confirmed this assumption. Number n of pores in two areas (30×30 μm^2) of AFM scanning of the sample almost doubles (from $n = 768$ to $n = 1\,327$), indicating high heterogeneity of surface erosion according to the type of blistering. The AFM scanning revealed a porous surface in the area with the most intense formation of pores, on which blisters could no longer form [13].

The AFM revealed new structural effects that could result in the spontaneous emission of electrons in the MWPCs. It was found that nanoscale carbon films are formed in the cavities and interstructural spaces of the copper foil of ME samples. Figure 4 (*upper part*) shows a fragment of an AFM scan of ME sample eight with a graphite-like film ~ 20 nm thick. The film is inside a cavity on the surface and has a characteristic structure similar to images of nanographite films obtained under laboratory conditions by condensing carbon from the gas phase [12]. Figure 4 (*lower part*) shows the current-voltage characteristic measured in the area where nanographite film is formed. A current-voltage characteristic with voltage U rising from −10 to +10 V is indicated by *red dots*. A current-voltage characteristic with voltage U falling from +10 to −10 V is shown by *blue dots*. The current hysteresis displays resistive switching, which is typical of many nanocarbon formations. The threshold value of the electric field strength for the emission of electrons in such structures is $E_t \approx 10$ kV · cm^{-1} [14].

A nanocarbon film is uncontrollably and slowly formed on the copper foil of the MWPC cathode. This occurs in the electric field of the detector ($E_{\text{cathode}} \approx 5$ kV · cm^{-1}) with the gas mixture of $Ar/CO_2/CF_4$ at atmospheric pressure under prolonged exposure by the charged particles and processes of plasma-chemistry interaction between the active radicals, ions, and copper. With AFM scanning, zones with a nanocarbon film are most often found near the walls of craters at the cathode.

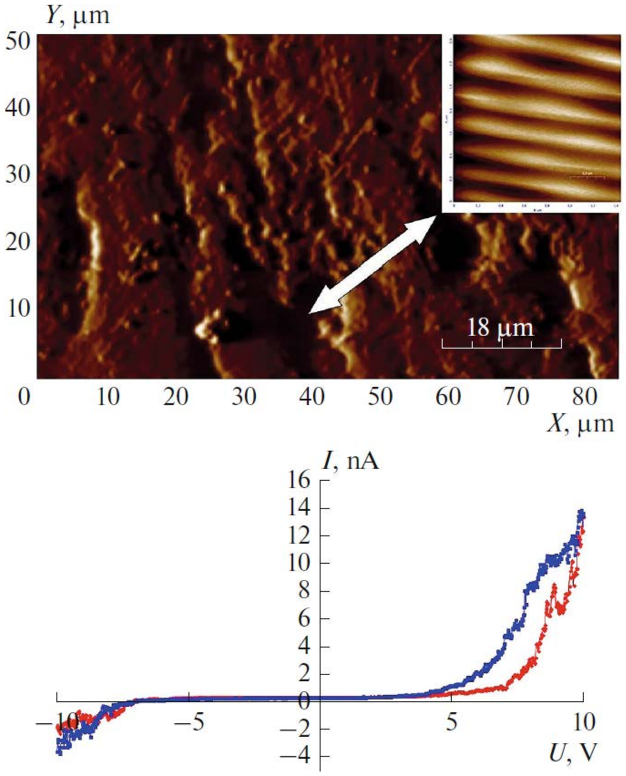

Fig. 4. An atomic force microscopy scan of ME sample eight with a scanning field size of 90 × 90 μm^2 (inset, 1.5 × 1.5 μm^2) is shown at the *top*. The current-voltage characteristic measured in the area of the nanographite film is shown *below*. The current-voltage characteristic upon raising voltage *U* from −10 to +10 V is represented by *red dots*. The current-voltage characteristic upon lowering voltage *U* from +10 to −10 V is given by *blue dots*

Our structural AFM-analysis of the MWPC cathode samples thus showed that the non-ME samples were characterized by a cellular structure with local zones of erosion. Radiation erosion was more pronounced in the ME samples. They were structurally heterogeneous, and their surfaces were smoothed as a result of melting. There were cascades of small craters (see Fig. 2*e*), and porous zones with many clearly visible small peaks and blisters. Nanosized carbon films were found at the boundaries of smoothed areas with loose defective areas, and in the cavities between microfibers in the ME samples. The observed morphological types of the surface were due to structural phase transformations and thermal processes that occurred on cathode surfaces under the action of charged particles and in pointwise zones of electron emission [12].

Integrated Rutherford backscattering spectra (RBSes) were analysed layer-by-layer for all types of the samples in areas of 300 × 300 μm^2. The depth of penetration measured for oxygen and carbon in the samples was no greater than 2 μm. The content of oxygen in near-surface layers (≤ 0.4 μm) was comparable for ME (~ 70%) and non-ME samples (~ 80%). On the other hand, the content of carbon in the ME samples (~ 15%) was three times higher than that in the non-ME samples (~ 5%). Graphite-like film formations on the surfaces of the ME samples are explained by their elevated carbon content (see Fig. 4). Another important difference between the samples was the presence of fluorine. In the RBS spectra of the ME samples, we detected fluorine at a level of ∼ 5% in addition to carbon and oxygen, due to the high sensitivity of the procedure. We may therefore assume there were structures that contained fluorocarbon compounds CF_n on both cathodes surfaces in the MWPC.

Our results from studying samples *via* Raman spectroscopy were in good agreement with those from *X*-ray phase analysis. The oxide phase of Cu_2O and the phase of amorphous carbon were revealed on the analysed ME and non-ME surfaces by blowing the gas mixture through all four planes of the MWPC in succession. The gas flow thus redistributed active radicals in the working volume of the MWPC over all of the cathodes [2]. The presence of the Cu_2O oxide phase on the surface of the cathode in the MWPC of the LHCb muon detector agrees with results from studying detector prototypes. Laboratory tests of the MWPC prototypes with an $Ar/CO_2/CF_4$ gas mixture have also established that Cu_2O was the main phase of the surface layers of cathode samples [6].

Copper oxide is a *p*-type semiconductor and, like all semiconductor materials, it is sensitive to the presence of defects and microimpurities. They result in local energy levels emerging in the bandgap and changes in such conductivity parameters as the concentration and mobility of carriers. The presence of Cu_2O oxide microgranules on the cathode surface may be the reason for the appearance of many centres of electron and photon emission with a wavelength $\lambda \approx 600$ nm at the electric field above a threshold of $E_t \geq 50 \text{ kV} \cdot \text{cm}^{-1}$ [8]. Due to the absorption of electrons in a cathode's material, however, the emission of electrons into the gas volume of the detector becomes impossible at a depth of ~ 1 μm. From the experience of observing ME in gas-discharge detectors, it is known that the dielectric on the cathode surface should be no more than several tens of nanometers thick for emission currents to appear [7]. Spontaneous currents due to Cu_2O granules are possible in the MWPC only if they form on the surface of a cathode in the form of micropeaks with an aspect factor (ratio of the height to the tip diameter) greater than 10 for the electric field on the cathode ($E_{\text{cathode}} \approx 5 \text{ kV} \cdot \text{cm}^{-1}$). The current of electrons through such a microobject heats the foil up to the melting point ($T_{Cu_2O} = 1\,235$°C). The emission of electrons stops as a result of changes in the electrochemical properties of the material. The next possible reason for the ME is the emission of electrons by nanographite structures. The results revealed the condensation of carbon- and fluorine containing molecules on the cathode that were produced in the gas-discharge plasma near the anode wire. An example of such structures are nanographite films that form crystallites 1–2 μm tall. Since they are thin, the aspect ratios of these structures can be as great as 1 000. The threshold value of the electric field for electron emission by nanographite films is $E_t \approx 10 \text{ kV} \cdot \text{cm}^{-1}$. This value of the electric field strength is easily achievable in an MWPC [11, 12].

The presence of fluorine and nanocarbon on the cathode surface can result in the formation of dielectric fluorocarbon compounds, which are a stable source of emission currents [14]. It is difficult to attribute definitely the nanostructures observed in the MWPC to one of the many models of low-threshold emission. To identify the reasons for the ME, however, it is important that almost all such nanostructures are characterized by electron emission.

4. Conclusion

The surface of a MWPC cathode from the LHCb experiment at the LHC was studied comprehensively for the first time in order to establish the reasons for spontaneous self-sustaining currents in the detector. Radiation erosion accompanied by the formation of copper oxide and nanosized carbon and fluorocarbon structures of high resistivity were revealed by the AFM, microprobes, *X*-ray diffractometry and Raman spectroscopy on the copper foil of the cathode. A characteristic feature of carbon and fluorocarbon nanostructures is the low threshold of electron emission. The threshold value of the electric field strength for nanostructures ($E_t \sim 10 \text{ kV} \cdot \text{cm}^{-1}$) is one fifth that of Cu_2O, and it can be reached on a cathode under the conditions of radiation damaging copper. Carbon and fluorocarbon nanostructures therefore seem to be the most realistic source of spontaneous currents in the MWPC.

References

1. L. Malter, Phys. Rev. **50**, 48 (1936).
2. F.P. Albicocco, L. Anderlini, M. Anelli *et al.*, JINST **14**, P11031 (2019).
3. H.H. Hansen, Int. J. Appl. Radiat. Isot. **34**, 1241 (1983).
4. S.B. Fisher, Radiat. Eff. Defects Solids **7**, 173 (1971).
5. D. Pfeiffer, G. Gorine, *et al.*, Nucl. Instrum. Meth. Phys. Res., Sect. A, **866**, 91 (2017).
6. M.E. Buzoverya, G.E. Gavrilov, O.E. Maev, Tech. Phys. **66** (2), 356 (2021).
7. G. Zhou, L. Wang, J.C. Yang, J. Appl. Phys. **97**, 063509 (2005).
8. R.E. Hurley, J. Phys. D: Appl. Phys. **10**, L195 (1979).
9. J. Va'Vra, Nucl. Instrum. Meth. Phys. Res., Sect. A **252**, 547 (1986).
10. V.A. Akat'ev, E.V. Metelkin, At. Energy **118** (2), 105 (2015).

11. A.N. Obraztsov, Al.A. Zakhidov, Diamond Relat. Mater. **13**, 1044 (2004).
12. A.N. Obraztsov, V.I. Kleshch, J. Nanoelectron. Optoelectron. **4**, 207 (2009).
13. M.I. Guseva, Yu.V. Martynenko, Sov. Phys. Usp. **24**, 996 (1981).
14. A.I. Ivanov, N.A. Nebogatikova, I.I. Kurkina, I.V. Antonova, Semiconductors **51** (10), 1306 (2017).

DATA ACQUISITION SYSTEM FOR THE EXPERIMENT “PROTON”

A.A. Vorobyev, V.L. Golovtsov, N.V. Gruzinsky, P.A. Kravtsov, P.V. Neustroev, E.M. Spiridenkov, L.N. Uvarov, A.A. Vasilyev, V.I. Yatsyura

The “Proton” experiment uses the innovative *ep* elastic scattering method, which allows recording both recoil protons and scattered electrons with high accuracy and resolution, which leads to a completely new approach to measuring the proton radius.

The “Proton” set-up [1] includes two gaseous ionization detectors: an active hydrogen target in the form of an axial time-projection chamber (TPC) detecting recoil protons and a high precision forward tracker (FT) in the form of a set of multiwire proportional chambers with a cathode strip readout that registers scattered electrons. The FT is located behind the TPC in a separate volume of the same vessel, see Fig. 1.

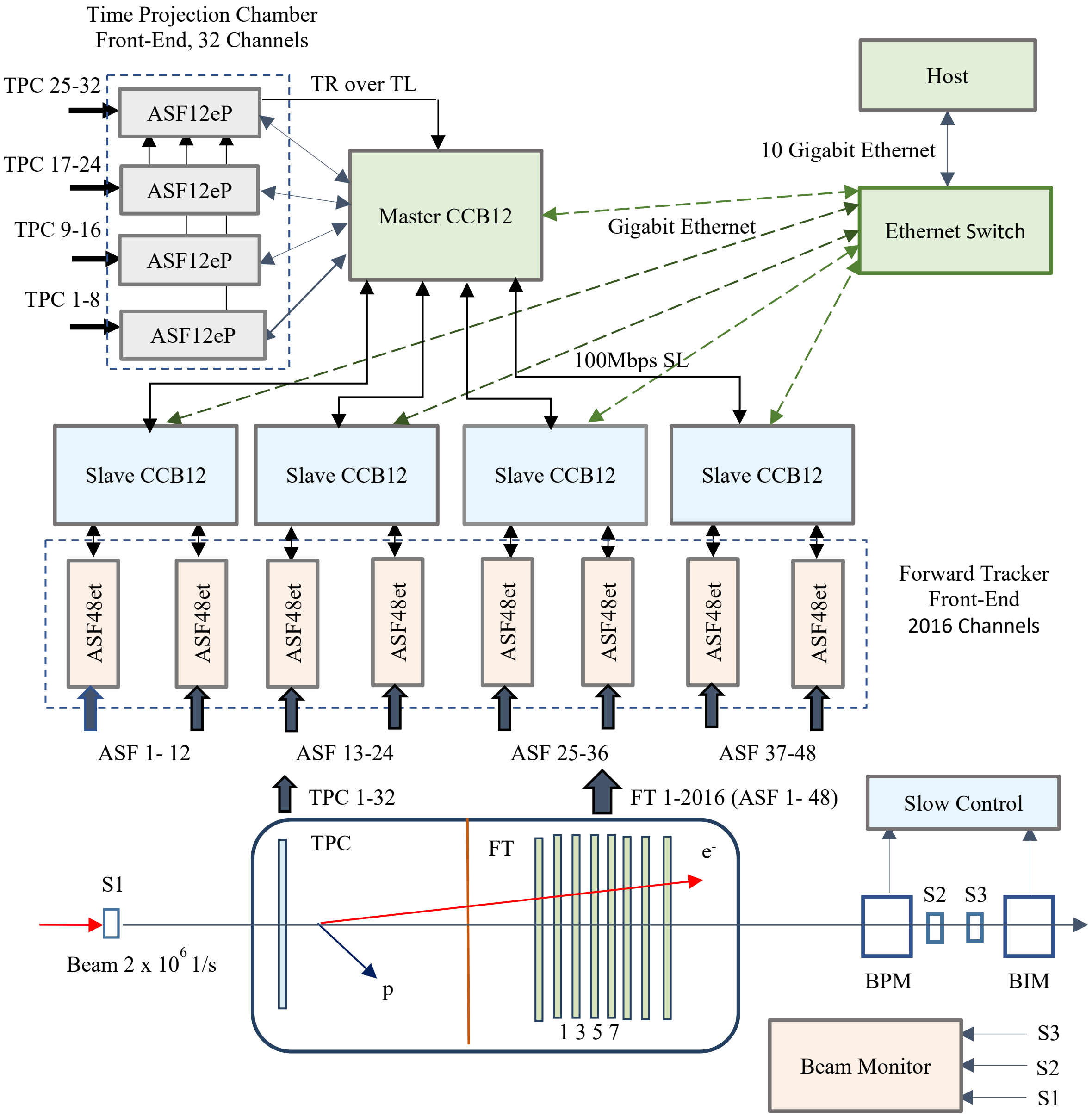

Fig. 1. Schematic view of the experimental set-up and the data acquisition system

The TPC anode is segmented into the central pad and eight concentric rings along the radius, some rings are subdivided into sectors. The total number of channels for the TPC anode readout reaches 32. The target parameters for the measurement are the energy of the recoil proton and the signal arrival time.

The FT consists of four pairs of chambers that measure the X and Y coordinates of the scattered electron track relative to the beam line. Each chamber is a symmetrical multiwire proportional chamber 600 × 600 mm^2 in size with an anode plane (wires with a pitch of 3 mm) between two cathode planes (wires with a pitch of 0.5 mm). The cathode wires are orthogonal to the anode wires in one cathode plane (X or Y) and are inclined at an angle of 45° in the other cathode plane (U). Every five wires in the orthogonal cathode plane are grouped into strips. The strip in an inclined cathode plane consists of 100 wires. The number of signal channels in each chamber is 240 + 12 = 254, which gives a total of 2016 channels for eight chambers. The target parameters for the measurement are the centre of gravity and the time of arrival of the cathode signal(s).

Beam monitoring is based on S1... S3 scintillation counters, a high-pressure ionization chamber as a beam intensity monitor (BIM) and a small proportional chamber as a beam position monitor (BPM). Knowing the number of beam electrons is necessary to determine the absolute cross section. The beam intensity is expected to be $2 \cdot 10^6$ electrons per second.

This article only deals with receiving events from the TPC and FT detectors and does not cover the electronics of the beam monitoring detectors. The detection of both the recoil proton and the scattered electron makes it possible to reconstruct the *ep* scattering event.

Using a flash analog-to-digital converter (flash ADC) is best suited to measure the target parameters of both detectors. The data acquisition system for the above two detectors has a tree-like architecture and is based on a configurable amplifier–shaper–flash (ASF) ADC, multichannel digitizer and a 12-port concentrator–control–board (CCB12). The CCB12 distributes the system clock and commands from the host computer to downstream devices over serial links (SL). The SL connects serial ports (SP) of the upstream and downstream devices and operates at 100 Mbps in both directions. A special class of broadcast commands addressed to the Master CCB12, such as “start operation”, “stop operation”, or generated by the Master CCB12, such as “trigger”, eventually reaches each device in the acquisition tree, causing them to work synchronously.

Registration of a recoil proton in any of the TPC channels causes a trigger request (TR) signal to be sent over the trigger link (TL) to the Master CCB12, the latter may distribute it as a “trigger” command.

Upon receiving a “trigger”, each channel of the TPC and FT digitizers generates a data block, containing event(s). An event is an array of flash ADC readings obtained as a result of digitizing the detector signal.

For offline event synchronization, each event in the data block is timestamped. The timestamp is a 44-bit binary counter that starts running in each device on the “start run” command. The counter overflow occurs after approximately 48 h. This makes the timestamp the unique identifier for the event. The CCB12 multiplexes twelve input 100 Mbps data streams into one and sends it to an Ethernet switch over Gigabit Ethernet. The switch communicates with the host *via* the 10 Gigabit Ethernet.

Digitizer. Two versions of the digitizer, called ASF12eP and ASF48et, serve the TPC and FT detectors, respectively. Both versions use the same ASF_48et main board design. It contains six flash ADC chips and programmable logic in the Spartan-6 LX field-programmable gate array (FPGA), see Fig. 2. For greater flexibility, the amplifiers and shapers are placed on a separate daughter board, which is connected to the input sockets on the main board.

The flash ADC chip is a 12-bit high-performance, low-power, octal channel analog devices ADS5282 ADC with a differential input voltage in the 2 V range and low-voltage differential signaling (LVDS) output. The input sampling rate can vary from 10 to 65 megasamples per second (MSPS). The output data latency is 12 sampling clock cycles. The serialized double data rate (DDR) outputs run at 6 times the input clock.

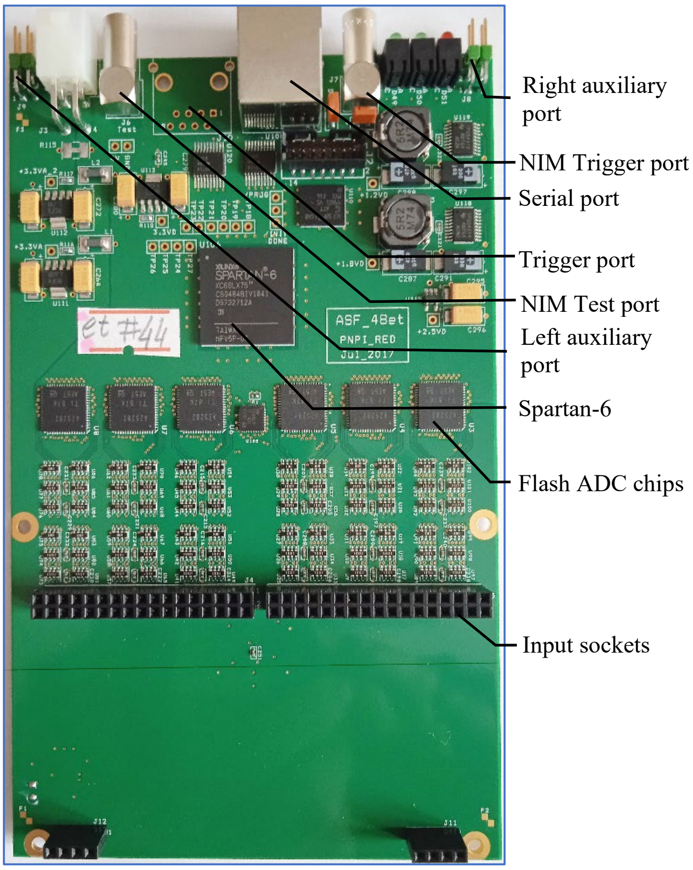

Fig. 2. ASF_48et close up

The Spartan-6 LX FPGA pinouts are 100% compatible across density in the same package. Thus, depending on the requirements, the ASF_48et board can be equipped with either the cheapest LX45 FPGA, or the more expensive LX75 and LX100 FPGAs, or the most expensive LX150 FPGA. All ports: SP for receiving commands and uploading data blocks, trigger port (TP) for sending TR to Master CCB12, NIM (NIM – current-based logic defined in nuclear instrumentation module standard) test port for receiving test signals, left and right auxiliary ports (LAP, RAP) for signal exchange between digitizers – are controlled *via* the FPGA. This data acquisition system does not use the NIM TP to receive external "trigger" signals. The signal standard for all ports except NIM is differential LVDS.

Concentrator. The CCB12 design is made as a main and daughter board, see Fig. 3. The main board has 12 SPs one upstream SP (USP) and TP. All ports use RJ45 connectors. The SLs connecting SPs or TPs of upstream and downstream devices are category 5e shielded patch cords. An inexpensive Spartan-3 FPGA on the main board controls all ports. The daughter board connects to the main board *via* a 96-pin connector. The daughter board is an off-shelf product TE0720-03-1CFA from Trenz Electronic GmbH. It integrates a Xilinx Zynq XC7Z020 system-on-chip (SoC), a Gigabit Ethernet transceiver, 1 GB DDR3 synchronous dynamic random access memory (DDR3 SDRAM), and 32 MB flash memory for configuration and operation. The SoC includes user-programmable resources: an Artix-7 FPGA and a dual-core ARM Cortex-A9 processor, on which all concentrator operation algorithms are built. The two versions of the concentrator, called Master CCB12 and Slave CCB12, use the same hardware but differ in firmware and processor codes.

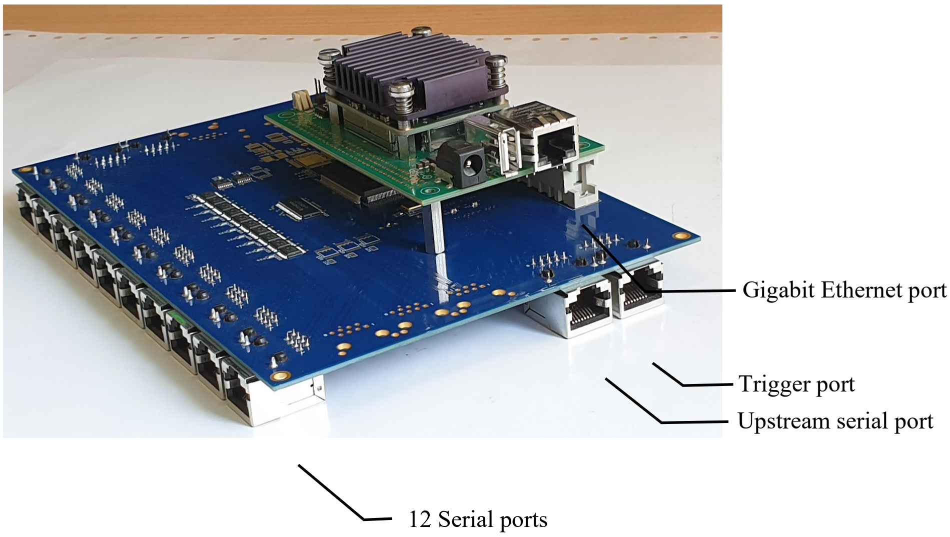

Fig. 3. Concentrator CCB12

ASF12eP digitizer. The ASF12eP digitizer collects data from the TPC. The TPC maximum drift time is 100 μs, but the spread of the signal arrival time from anode segments does not exceed 25 μs. To get a complete picture of the recoil proton track, the digitizers collect data from all segments of the anode in a 40 μs window. The chosen 25 MHz sampling rate is a compromise between obtaining optimal time resolution (40 ns), the number of readings per "trigger" (typically 1 000 readings, but can be increased to 4 000 readings) and the expected "trigger" rate of 50 Hz. To further minimize the SL load and dead time, the number of channels has been reduced from a potentially available 48 to 12. Low-noise, charge-sensitive preamplifiers with a peaking time of 1 μs have a noise level of 13 keV + 0.5 keV/pF and can measure TPC signals from 250 keV up to 5 MeV.

The main board has a Spartan-6 LX100 FPGA. The logic for each digitizer channel includes:

- Deserializer of flash ADC serial output into a parallel word;
- 12-bit signal amplitude discriminator;
- 18-bit moving integrating window (MIW);
- 15-bit MIW discriminator;
- Oipeline delay to compensate for "trigger" latency;
- 8K word first-in-first-out (FIFO) memory that serves as the channel's derandomizing buffer.

The MIW width can be up to 127 readings. The integrator works with the 11 most significant bits (MSB) of the flash ADC reading. On each sampling clock cycle, it adds a new reading and subtracts the earliest in time. The MIW discriminator compares the 15 MSB of the integrator with a threshold.

The outputs of the amplitude discriminator or MIW discriminator in any channel, or their coincidence, can be the source of the TR signal. TR is available at LAP or RAP. One of the four ASF12ep digitizers collects all TR *via* logical OR and sends them *via* TL to the TP of the Master CCB12, and the Master CCB12 broadcasts it as a "trigger" to all devices. Upon receiving a "trigger", each channel of the digitizer generates an event with a timestamp corresponding to the time the "trigger" arrived. Events from all channels are combined into a common 32K word FIFO, which serves as a device derandomizing buffer and forms a single output data stream. Typically, TR generation is enabled for the second or third ring segments of the anode, *i. e.* delayed relative to the beginning of the track. To compensate for the delay, the event window typically begins 15 μs before the "trigger" and ends 25 μs after it, but can be adjusted over a wide range.

ASF48et digitizer. The ASF48et digitizer collects data from the FT. Any electron track found in the FT (outside the central dead zone of 2 cm) in the time window 100 μs before the "trigger" signal could be the parent particle of the recoil proton. The digitizer is equipped with low-noise, charge-sensitive preamplifiers with a peaking time of 1 μs and a noise level of 0.072 fC + 0.0015 fC/pF.

The main board has a Spartan-6 LX75 FPGA. The logic for each digitizer channel includes:

- Deserializer of flash ADC serial output into a parallel word;
- Signal amplitude discriminator;

- Pipeline delay to compensate for “self-trigger” latency;
- 1K word memory as a ring buffer.

Each channel operates in self-triggered mode. Self-triggering causes the event to be stored in the ring buffer. Each event contains a timestamp corresponding to the time the “self-trigger” arrived and an array of flash ADC readings (typically 80 readings, but can be increased to 960 readings). The time position of the event is chosen to include both baseline and maximum amplitude readings. Both are used to find the centre of gravity (coordinate) of the scattered electron. Upon receiving a “trigger”, self-triggered events from all channels that occurred in the 100 μs time window preceding the “trigger” are reloaded into a 16K word output FIFO to eventually form a single output data stream.

Master CCB12 and Slave CCB12 concentrator. The Master has a built-in trigger logic that receives TR signals from the ASF12eP digitizer and sends “triggers” to other devices in the acquisition tree. It assigns a timestamp to each received TR and marks it if it is used to generate a “trigger”. The “trigger” information constitutes the 13th data stream in addition to the 12 data streams coming from the SPs. The Master also distributes broadcast commands from the host to all downstream devices. It has different logic for the SP connected to the digitizer and the SP connected to the Slave, because it does not receive any data from the Slave, only its busy status, which is used in the trigger logic.

Both types of concentrators have the same logic for the SP connected to the digitizer. Two special commands “hold” and “resume” control the flow of data between digitizers and concentrators: “hold” causes the digitizer to stop sending data, and “resume” resumes normal data flow. The 16K word FIFO at the input of each SP serves as the channel’s derandomizing buffer. The FPGA logic reloads the data from the input FIFO to the 32K word output FIFO, splitting it into packets with headers and trailers. The header and trailer added to the packet contain overhead information such as header timestamp, packet number, SP number, number of kilo-words loaded into input and output FIFOs, trailer timestamp, and checksum. The processor forwards packets from the output FIFO to the host *via* Gigabit Ethernet.

The data acquisition system for the “Proton” experiment has been tested on cosmic rays.

References

1. A.A. Vorobyev *et al*. PNPI. High Energy Physics Division. Main Scientific Activities 2013–2018, 316–325 (2019).

HIGH-TEMPERATURE AND MASS-SEPARATOR METHODS FOR SELECTIVE PRODUCTION OF MEDICAL RADIONUCLIDES AT PROTON AND NEUTRON BEAMS

V.N. Panteleev, A.E. Barzakh, D.V. Fedorov, V.S. Ivanov, P.L. Molkanov, S.Yu. Orlov, M.D. Seliverstov

1. Introduction

Special pharmaceuticals, prepared on the basis of radionuclides, are very efficient tools for diagnostic and therapy of many kinds of different diseases. Presently, reactors on thermal neutrons and high current cyclotrons are utilized to this end. Regardless of the production method, the desired radionuclides should be separated from the irradiated target material and other undesired radionuclides. Generally, the so called “wet” radiochemical methods are used for extraction and purification of targeted medical radionuclides. However, these methods are accompanied by a large amount of liquid radioactive waste. Nevertheless, the problem of the isotope purification was successfully solved more than sixty years ago by building of special installations for nuclear physics studies – isotope separator on-line (ISOL) facilities working at beams of different projectile particles.

2. Mass-separator method

Shortly, the mass-separator method may be described as follows. At an ISOL installation, radioactive atoms are produced in an irradiated mass-separator target kept at a high temperature in a high vacuum. Then the atoms diffuse out of the target material and effuse as neutral atoms from the target container into the cavity of an ion source, where they are ionized. Finally, they form radioactive ion beams [1] after passing through a system of electrostatic lenses and a magnet analyser.

This method is usually applied for short-lived isotope production in nuclear physics experiments for study of exotic nuclei. The mass-separator method gives the possibility to produce very pure beams of radioisotopes. Another advantage of the mass-separator method is that several radioisotopes separated according to their mass numbers can be obtained and investigated simultaneously.

The mass separator can be applied for production of radionuclides in various modes:

- On-line mode (radionuclides are accumulated in the process of the target irradiation);
- Semi on-line mode (radionuclides are accumulated after the switching off the irradiating beam);
- Off-line mode (the target is irradiated separately and after that it is installed at the mass-separator).

In any case, certain requirements on the target material should be fulfilled. It should be a high-temperature resistant (to avoid destruction at a temperature of the targeted radionuclide evaporation) and should have a low vapor pressure ($< 10^{-4}$ mbar) at the working temperature to ensure a proper work of a high voltage system of the mass-separator. Provided these requirements are fulfilled, long-term operation of the mass-separator can be ensured with the efficiency of some radionuclide production up to 80%.

First experiments on the production of mass-separated medical radioisotopes were successfully carried out at the on-line mass-separator facility ISOLDE at CERN [2, 3]. These experiments have shown very promising prospects of the method, provided that it would be possible to increase significantly the activities of the obtained radionuclide samples. This can be achieved by using high current cyclotrons or high neutron-flux reactors.

3. High-temperature method of separation of the target material and the produced radionuclide

In case of non-compliance the above mentioned conditions for collection of long-lived radioisotopes with the half-lives of several tens of hours or more, a method of thermal preseparation in vacuum of the target material and the selected radionuclides was proposed [4].

For this purpose, the difference in volatility of atoms of the desired radionuclide, the target material, and other produced radionuclides at a certain target temperature was used. In other words, the separation can be done if the target material and the atoms of targeted radionuclides have a considerable difference in the saturated vapour pressure in vacuum at a certain temperature. In general, this difference correlates with the difference in enthalpy of adsorption on the surface of refractory metals from which the target containers are usually manufactured [5].

If the target material is much more volatile (has much higher vapour pressure) than the resulting radionuclide, it can be easily evaporated at a certain temperature from the target container into some cold ballast volume without loss of the resulting radionuclide. As it was demonstrated in our previous work, the radionuclide ^{82}Sr used for positron emission tomography (PET) diagnostics can be isolated from the binary compound of the RbCl target material with the efficiency better than 99% by heating it in a high vacuum for one hour [4, 6]. It was also shown that this principle works for separation of ^{82}Sr from metallic rubidium and a therapeutic radionuclide ^{67}Cu from a target made of metallic zinc [7].

These results show that the effect of thermal separation is universal regardless of whether the target substance is a molecular compound or it is in the natural metallic state. It is very important that the carrier-free radionuclide samples prepared by this method can be further utilized for isotopic separation using a mass-separator. This is necessary, when other radioisotopes of the selected element are present in the resulting sample.

Our previous work is related in general to the development of a thermal method for the separation of radionuclides obtained by irradiation of a target by protons of different energy [1, 4, 7, 8]. The main objective of the present work is to test experimentally whether this method could also be used to isolate the radionuclides produced in reactions with neutrons. For this purpose, ^{177}Lu which is the most promising radionuclide for the treatment of prostate tumors and ^{99m}Tc, widely used for diagnostics, were selected. In the experiments, a metallic ytterbium target was used in order to obtain ^{177}Lu. For ^{99m}Tc production, the molybdenum oxide MoO_3 target was used.

4. Radioisotope complex ISOTOPE project

A detailed description of the ISOTOPE project which is constructed at the beam of high current cyclotron C-80 [9] can be found in Ref. [10]. Below its main features are presented.

The cyclotron C-80 with the proton beam energy 40–80 MeV and the intensity of 100 μA is designed to produce a wide spectrum of medical radionuclides for diagnostics and therapy. The use of three target stations will allow one to investigate and introduce different new methods of radionuclide production. They are the high-temperature separation method [1] and the mass-separator method, in which a specially constructed target is used [4]. A mass-separator with its target station will allow one for the production of isotopically separated medical radionuclides of a high purity, which will be implanted into corresponding collectors from which they can be easily extracted. Radionuclides which are planned for production at ISOTOPE are listed in Table 1. Additionally new methods are being developed for the following radionuclide production: ^{64}Cu, ^{67}Cu, ^{149}Tb, ^{177}Lu, ^{188}Re, ^{212}Pb, ^{212}Bi.

Table 1

Radionuclides planned for production at ISOTOPE

Radionuclide	Decay half-life, $T_{1/2}$
^{68}Ge	270.8 d
^{82}Sr*	25.55 d
^{99}Tc	6 h
^{111}In*	2.8 d
^{123}I*	13.27 h
^{124}I*	4.17 d
^{223}Ra*	11.4 d
^{224}Ra*	3.66 d
^{225}Ac*	10 d

* Radioisotopes, which can be produced by means of a mass-separator.

5. High-temperature separation of lutetium radionuclides from an ytterbium target irradiated by protons and neutrons

^{177}Lu is considered to be a very efficient radionuclide for the prostate cancer therapy [11]. It can be produced by thermal neutrons in the ^{176}Yb(n, γ)^{177}Yb → ^{177}Lu reaction. Usually, to extract ^{177}Lu from an irradiated ytterbium target, a complex radiochemical procedure, called “wet radiochemistry” is used. According to Ref. [5], ytterbium and lutetium are elements with very different enthalpy of adsorption on refractory metal surfaces – ~ 3.6 and ~ 6.6 eV, respectively. As is pointed out above, enthalpies of adsorption in general are in good correlation with the boiling points of the corresponding elements. In particular, this is confirmed for the couple ytterbium–lutetium with their boiling points of 1 194 and 3 393°C, respectively.

The first tests of a high-temperature method for separation of $^{171,\,172}$Lu from an ytterbium metal target were described in Ref. [12]. In that work, an ytterbium metal target was irradiated by a proton beam of the PNPI synchrocyclotron SC-1000 with a proton energy of 100 MeV. Such a beam was achieved by using a calibrated copper degrader [13] with remote change of its thickness.

For the neutron irradiation experiment for ^{177}Lu production, a neutron lead converter was used. The ytterbium target material was placed in a water tank, staying close to the neutron converter. The water tank with a metal ytterbium target is shown in Fig. 1. The target mass of metallic ytterbium for the experiment with neutron irradiation was about 100 mg. After three days of radiation cooling, the target was placed into a quartz vessel, which was inserted into a tungsten oven, heated by resistant heating at the vacuum test bench. The target material processing procedure was completely identical to that described in Ref. [12].

Fig. 1. The water tank used for slowing down of scattered neutrons. A metal ytterbium target is placed in a cylindrical channel inside the tank

During all the time of the target heating, the evaporated target material (metallic ytterbium) was collected in a special cooled volume. In the process of the target material evaporation, the oven temperature was kept in the interval of 800–900°C for the period of one hour in a high vacuum about 10^{-5} mbar.

In Figure 2*a*, the spectra with γ-lines of proton-irradiated ytterbium before (*black points*) and after (*red points*) the target heating in the quartz vessel are shown. The γ-line with the energy of 396 keV follows the ^{175}Yb ($T_{1/2}$ = 4.2 d) β^--decay. This line was used for calculation of the target material evaporation efficiency x, which can be expressed by the formula

$$x = (S_1^{\mathrm{Yb}} - S_2^{\mathrm{Yb}})/S_1^{\mathrm{Yb}}, \tag{1}$$

where S_1^{Yb} – the γ-line intensity of ^{175}Yb before the irradiated sample heating; S_2^{Yb} – the intensity of the same γ-line after the sample heating.

The γ-line with the energy of 740 keV belongs to the ^{171}Lu ($T_{1/2}$ = 8.24 d) β^+-decay. A comparison of its intensity before and after heating shows what part of lutetium atoms remains in the vessel after heating. One can calculate the efficiency of lutetium isotope production ε using the following expression:

$$\varepsilon = S_2^{\mathrm{Lu}} / S_1^{\mathrm{Lu}},$$

where S_1^{Lu} – the γ-line intensity of ^{171}Yb before the irradiated sample heating; S_2^{Lu} – the intensity of the same γ-line after the sample heating.

In Figure 2*b*, the spectra with γ-lines of neutron irradiated ytterbium before (*black points*) and after (*red points*) target heating in a quartz vessel are shown. The γ-lines with the energies of 177 and 198 keV follow the ^{169}Yb ($T_{1/2}$ = 32 d) β^+-decay. These lines were used for monitoring of the target material evaporation. The γ-line with the energy of 208 keV belongs to the ^{177}Lu ($T_{1/2}$ = 6.73 d) β^--decay and shows what part of lutetium atoms remains in the vessel after heating.

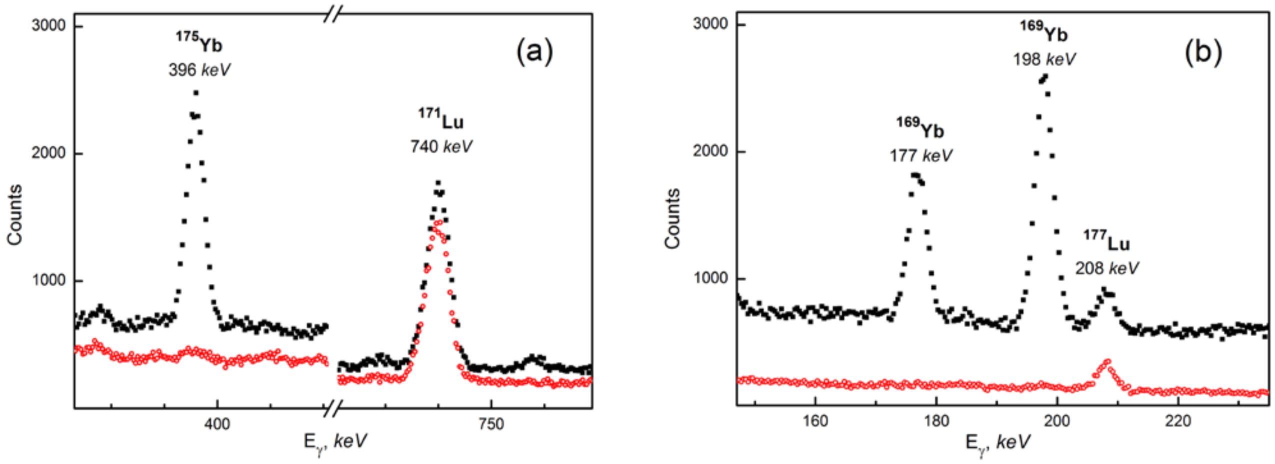

Fig. 2. Gamma spectra of the ytterbium target before (*black squares*) and after (*red open circles*) heating of the sample irradiated: *a* – by protons; *b* – by neutrons

The γ-lines intensities of the ytterbium and lutetium isotopes mentioned above are shown in Table 2. A comparison of the results of two experiments presented in Fig. 2 and Table 2 demonstrates that the method of thermal separation of lutetium isotopes does not depend on whether the required radionuclide are produced in the target material by protons or by neutrons.

Table 2

Gamma-lines intensities of the ytterbium and lutetium isotopes

Irradiation method	Protons (100 MeV)		Thermal neutrons	
Radionuclide	^{175}Yb	^{171}Lu	^{169}Yb	^{177}Lu
E_γ, keV	396	740	198	208
S_γ before heating	19 500	20 500	20 000	2 680
S_γ after heating*	870	19 940	300	2 060

* Corrections for S_γ after heating were introduced in accordance with decay half-lives.

The evaporation efficiency *x* for the Yb target material irradiated by protons and the production efficiency ε were determined as 0.96(1) and 0.97(2), respectively. For identical Yb target material irradiated by thermal neutrons these values were 0.99(1) and 0.77(7).

Despite the pronounced effect of efficient separation of lutetium isotopes produced by protons or neutrons from the metallic ytterbium target and relatively small statistical errors, the difference between the values of the production efficiency for different projectiles (protons or neutrons) is about 20%. This discrepancy can be explained by a possible systematic error resulting from not precisely controlled procedure of the temperature rise while reaching the optimal temperature of the target material evaporation. In that case, if the temperature increases too rapidly, the desired radionuclides can be entrained by the flow of atoms of the target substance.

6. High-temperature separation of ^{99m}Tc from a molybdenum trioxide ^{99}Mo / ^{99m}Tc target irradiated by protons and neutrons

The ^{99}Mo / ^{99m}Tc radionuclide generator is the most widely used in diagnostic medicine. In the diagnostic procedures ^{99m}Tc ($T_{1/2}$ = 6.01 h) is used. It is extracted from the generator containing the parent isotope ^{99}Mo ($T_{1/2}$ = 2.75 d). The most common method for obtaining ^{99}Mo is the fission reaction of highly enriched ^{235}U with thermal neutrons. An alternative way is the method based on the application of a proton cyclotron. The mass of the target material MoO_3 for experiments with proton and neutron irradiation was about 200 mg. The molybdenum trioxide was irradiated by a proton beam of the PNPI synchrocyclotron SC-1000 with a proton energy of 100 MeV.

For the neutron irradiation of the molybdenum trioxide, a neutron lead converter was used. Similar to the experiment with Yb/Lu, the target material was placed into a water tank, staying close to the neutron converter (see Fig. 1). In each experiment, the irradiation time was about 24 h. The majority of isotopes produced by protons in a MoO_3 target have a fairly short life-time. Therefore, the cooling time of the irradiated target was only three hours. After that it was placed into a quartz vessel, which was inserted into a tungsten oven heated by resistant heating at the vacuum test bench. During all the time of the target heating, the evaporated target material MoO_3 was collected in a special cooled volume. During the target material evaporation, the oven temperature was kept in the interval of 600–800°C for the period of one hour in a high vacuum about 10^{-5} mbar.

The time interval between measurements of the spectra before and after target material heating was two hours. Corrections for isotope decay half-life were introduced when comparing the γ-lines intensities. In Figure 3*a*, the γ spectra of the proton irradiated molybdenum trioxide target before (*black points*) and after (*red points*) target heating in the quartz vessel are shown.

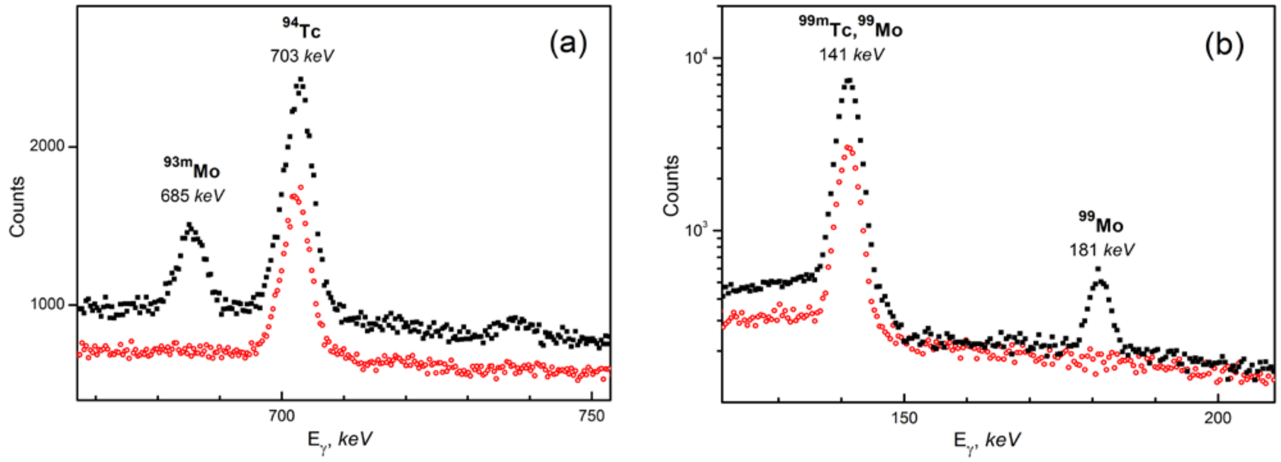

Fig. 3. Gamma spectra of the molybdenum trioxide target before (*black squares*) and after (*red open circles*) heating of the sample irradiated: *a* – by protons; *b* – by neutrons

In Figure 3*a*, the γ-line with the energy of 685 keV follows the ^{93m}Mo ($T_{1/2}$ = 6.85 h) β^--decay. This line was used for monitoring the target material evaporation. The part of the evaporated MoO_3 target material was calculated by the following formula:

$$x = (S_1^{\mathrm{Mo}} - S_2^{\mathrm{Mo}})/S_1^{\mathrm{Mo}}, \tag{3}$$

where S_1^{Mo} – the γ-line intensity of ^{93m}Mo before the target material heating; S_2^{Mo} – the intensity of the same γ-line after the sample heating.

The γ-line with the energy of 703 keV belongs to the ^{94}Tc ($T_{1/2}$ = 4.88 h) β^--decay, and a comparison of its intensity before and after heating shows what part of technetium atoms remains in the vessel after heating. One can calculate the efficiency of technetium isotope production using the following expression:

$$\varepsilon = S_2^{\mathrm{Tc}}/S_1^{\mathrm{Tc}},$$

where S_1^{Tc} – the γ-line intensity of ^{94}Tc before the target material heating; S_2^{Tc} – the intensity of the same γ-line after the sample heating.

In Figure 3*b*, the spectra of neutron irradiated molybdenum oxide before (*black points*) and after (*red points*) target heating are shown. The γ-line with the energy of 181 keV follows the ^{99}Mo ($T_{1/2}$ = 2.75 d) β^--decay. This line was used for monitoring the target material evaporation. The γ-line with the energy of 141 keV belongs to the ^{99m}Tc ($T_{1/2}$ = 6.01 h) isomeric transition and shows what part of technetium atoms remains in the vessel after heating. The γ-lines intensities of the molybdenum and technetium isotopes mentioned above are presented in Table 3. A comparison of the results of two experiments presented in Fig. 3 and Table 3 demonstrates that the method of thermal separation of technetium isotopes does not depend on whether the required radionuclide are produced in the target material by protons or by neutrons.

Table 3

Gamma-lines intensities of the molybdenum and technetium isotopes

Irradiation method	Protons (100 MeV)		Thermal neutrons	
Radionuclide	^{93m}Mo	^{94}Tc	^{99}Mo	^{99m}Tc
E_γ, keV	685	703	181	141
S_γ before heating	7 450	24 600	2 800	64 300
S_γ after heating*	0	22 500	0	35 800

* Corrections for S_γ after heating were introduced in accordance with decay half-lives.

The evaporation efficiency *x* for the MoO_3 target irradiated by protons and the production efficiency ε were determined as 0.96(3) and 0.92(3), respectively. For the identical MoO_3 target material irradiated by thermal neutrons these values were 0.99(3) and 0.56(1).

Apparently, the difference between the production efficiency values for different projectiles (protons or neutrons) can be ascribed as in the case of Lu to the not precisely controlled procedure of temperature rise while reaching the optimal temperature of the target material evaporation. Another possibility of uncontrolled escape of technetium during the thermal injection from MoO_3 target is discussed in the next section.

7. Discussion

The goal of this work was to check the applicability of the method of thermal separation in vacuum of the desired isotopes from targets irradiated not only by protons but also by neutrons. For this purpose, the target materials were selected that ensure the production of radionuclides of lutetium and technetium both with proton and neutron beams. They were: metallic ytterbium for lutetium production and a binary molecular compound molybdenum oxide MoO_3 for technetium production.

It is natural to assume that in the case of a metal target the process of separation of the target substance and the produced radionuclides should not depend on how radionuclides are produced – using protons or neutrons, since both the target substance and the produced radionuclides are in the form of atoms. Therefore, it should be expected that at a significantly higher degree of volatility of the atoms of the target substance (ytterbium) with respect to the atoms of the generated lutetium (boiling points, respectively, 1 194°C and 3 393°C) a possibility arises to evaporate selectively the atoms of the target substance, while keeping the atoms of lutetium in the heated capsule. As it can be seen in Figures 2*a* and 2*b*, the thermal separation process is quite efficient, regardless of the method of obtaining lutetium from a metal ytterbium target.

A similar process occurs when a molecular compound is used as a target substance in the case of irradiation by protons. In this case, the molecular bonds are destroyed due to the bombardment of the target by protons with the energy of several tens of MeV and the produced nuclides are presented in the target as atoms rather than retain their molecular form. Therefore, the process of separation of the target substance (in this case MoO_3 with the boiling point 1 255°C) and the produced radionuclide technetium (with the boiling point 4 265°C) will proceed as efficiently, as in the case of the above-discussed lutetium.

A somewhat different situation may arise when a molecular compound is irradiated by neutrons. In this case, the destruction of the molecular bonds may not occur, as the recoil energies are commensurate with the binding energy of the molecule. This can lead to the formation of a new molecular compound, containing the produced radionuclide, with a high volatility, which will not allow the thermal separation of the target substance and the desired radionuclide. In the case of the target substance MoO_3, such a compound may be TcO_2, which has the boiling point about 1 100°C. Therefore, for each target substance in the form of a molecular compound (oxide, chloride, fluoride) preliminary experiments should be carried out to study the efficiency of production of the target material and the desired radionuclide, if they are produced by neutrons.

8. Conclusion

The present work shows that the method of thermal separation in vacuum can be used to isolate the produced radionuclides from the target substances irradiated not only with proton but also with neutron beams. The value of the efficiency of extraction of ^{177}Lu from the target of metallic ytterbium irradiated with neutrons is 77% with the efficiency of evaporation of the target substance being close to 100%. This value is somewhat different from the value of the efficiency of ^{171}Lu extraction, obtained by its isolation from exactly the same target material irradiated by a proton beam. The reason for this can be insufficiently precisely controlled rate in the process of reaching the operating temperature of evaporation of the target substance.

The value obtained for the production efficiency of ^{99m}Tc from the MoO_3 target material irradiated with neutrons is about 56%. This value differs significantly from the value of the production efficiency $\varepsilon = 92\%$ of ^{94}Tc from the same target material irradiated by protons.

Another possible reason for this discrepancy, beside the mentioned above for the lutetium case, is the formation of the molecular compound TcO_2, which has a boiling point of about 1 100°C very close to that of the target material. In this case, some of technetium atoms included in the formed TcO_2 molecules will evaporate at the same rate as the molecules of the target substance. But it should be pointed out here that at this stage of the research this assumption requires additional experimental verification.

References

1. V.N. Panteleev *et al.*, Rad. Appplic. **3**, 106 (2018).
2. G.J. Beyer, Hyperfine Interact. **129**, 529 (2000).
3. G.J. Beyer, T.J. Ruth, Nucl. Instrum. Meth. Phys. Res. B **204**, 694 (2003).
4. V.N. Panteleev *et al.*, Tech. Phys. **63**, 1254 (2018).
5.R. Kirchner, Nucl. Instrum. Meth. Phys. Res. B **26**, 204 (1987).
6. V.N. Panteleev *et al.*, RAD Proc. **2**, 43 (2017).
7. V.N. Panteleev *et al.*, Phys. Part. Nucl. **49**, 75 (2018).
8. V.N. Panteleev *et al.*, Rev. Sci. Instrum. **86**, 123510 (2015).
9. S.A. Artamonov *et al.*, PNPI. High Energy Physics Division. Main Scientific Activities 2007–2012, 332 (2013).
10. V.N. Panteleev *et al.*, PNPI. High Energy Physics Division. Main Scientific Activities 2007–2012, 278 (2013).
11. A.A. Shurinov *et al.*, Simpozium “Yadernaya Meditsina”: Sb. Tes. Docl., 18 (2019).
12. V.N. Panteleev *et al.*, RAP Conf. Proc. **1**, 1 (2019).
13. S.A. Artamonov *et al.*, PNPI. High Energy Physics Division. Main Scientific Activities 2013–2018, 6 (2019).

MODERNIZATION OF THE MEDICAL PROTON COMPLEX FOR STEREOTACTIC RADIOSURGERY AT NRC “KURCHATOV INSTITUTE” – PNPI

L.G. Vaganyan, A.A. Vasilev, D.L. Karlin, N.A. Kuzora, V.I. Maksimov, F.A. Pak, A.I. Khalikov

This paper is dedicated to the memory of professor Aleksey Alekseevich Vorobyov, who proposed in november 1971 to use a 1 GeV proton beam of the SC-1000 for clinical radiation therapy.

1. Introduction

Radiotherapy (stereotactic radiosurgery) using a proton beam of the synchrocyclotron SC-1000, was conducted from 1975 to 2013. It confirmed its viability and effectiveness, and received recognition in the scientific community. This article considers the method of proton therapy with 1 GeV beam energy based on the Medical Proton Complex (MPC) of the National Research Centre “Kurchatov Institute” – PNPI, created by the joint efforts of the PNPI and of the Russian Scientific Centre for Radiology and Surgical Technologies (RSC RST). The main results of the current activities of the Laboratory of Medical Physics of the Department of Medical Radiology of the PNPI on the modernization of the MPC, which consists in updating the material and technical base, expanding verification methods for quality assurance (QA) of dose planning and dose delivery for stereotactic radiosurgery using protons with an energy of 1 GeV at the PNPI, are presented. The modernization program will bring the treatment of oncological diseases in Gatchina to a new level.

Nowadays, thanks to technological advances of developed countries, radiation therapy has reached a qualitatively new level and has made a significant progress in terms of achieving the main aim, which is bringing the required dose to the therapeutic focus area while maintaining healthy tissues. About 40% of patients in Russia and up to 70% of patients in other developed countries receive at one stage or another the disease radiation treatment alone or in combination with other methods of cancer treatment. One of the most perspective and actively developing type of radiotherapy is proton beam therapy (PBT). The main advantage of using protons is a more efficient dose distribution within a target than with other types of radiation therapy.

Currently, there are more than 80 functioning PBT centres in the world [1], four proton therapy centres operating in Russia:

- A medical and technical complex in Dubna based on the Joint Institute for Nuclear Research phasotron, which accelerates protons to 660 MeV and protons are slowed down to 200 MeV for medical purposes;
- A proton complex at the A. Tsyba Medical Radiological Research Centre in Obninsk, opened in 2016 on the basis of a synchrotron with variable proton energy in the range from 70 to 250 MeV;
- The medical and diagnostic centre of the Sergey Berezin Medical Institute in Saint Petersburg, launched in 2017 on the basis of a Varian cyclotron with an energy of 250 MeV;
- A multicabin centre in Dimitrovgrad, launched in 2019 on the basis of an ion beam applications (IBA) cyclotron with an energy of 235 MeV.

2. Bragg peak method and on-through method

A typical depth dose distribution curve for a proton beam (Bragg ionization curve) in a tissue-equivalent medium (Fig. 1) has certain features. Depending on which part of the Bragg curve falls on the irradiation focus, there are two options for radiation therapy with proton beams: irradiation method using the Bragg peak (the method of stopping) and the method of irradiation with the plateau region (the “on-through” method). The last method is expedient to use for narrow beams. Protons up to 250 MeV are used when appliying the Bragg peak method. Their range in biological tissues corresponds to the depth of the irradiated objects. A successful experience was gained in radiotherapy of patients with intracranial pathologies using higher energy protons in the USSR, which will be discussed in the article. The treatment of patients was started in 1975 in Gatchina (Leningrad region, Russia), at the Leningrad Nuclear Physics Institute (LNPI, and PNPI nowadays). The radiation therapy was carried out by the “on-through” method with 1 GeV protons of the LNPI synchrocyclotron SC-1000 [2]. It is worth noting that the first experience of proton therapy at Berkeley was just the “on-through” method.

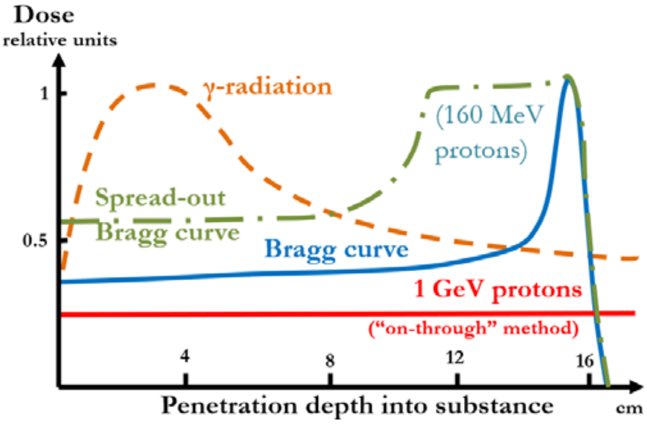

Fig. 1. Absorbed dose radiation distribution depending on the penetration depth into substance

The method of proton therapy using a beam of such energy is fundamentally different from other methods. There is no experience in the world practice of clinical use of beams of such energy in matters of their formation and dosimetry. The proton beam of the accelerator is monoenergetic and it has a small cross section. In order to enhance the effect in the irradiated tumor and to reduce the irradiation of healthy tissues, the technique of multifield irradiation from different directions is applied, which is implemented by rotating the irradiation stand relative to a monodirectional stationary beam.

The therapeutic installation (UPST) designed to implement the multifield irradiation technique in PNPI is shown in Fig. 2. The main elements of the UPST are a treatment table, a head fixation device (HFD) and an *X*-ray centralizer. The treatment table can rotate around the vertical axis (*Z*), passing through the isocentre of the installation by ±40°. The HFD can perform pendulum movements at an angle of up to ±36° around the horizontal axis (*X*) perpendicular to the beam axis (*Y*). Both rocking axes, as well as the axis of the proton beam, intersect at one point, which is the isocentre of the UPST. At any rotation of the head fixation device and the treatment table, the object located in the isocentre of the UPST remains motionless. Thus, the proton beam is directed to the set-up isocentre (target centre) at different angles. The *X*-ray centralizer is a specially adapted *X*-ray diagnostic apparatus with the ability to rotate around the isocentre. It has two fixed positions: horizontal and vertical, which makes it possible to produce a lateral and frontal *X*-ray image, respectively, for precise targeting at the isocentre of the UPST.

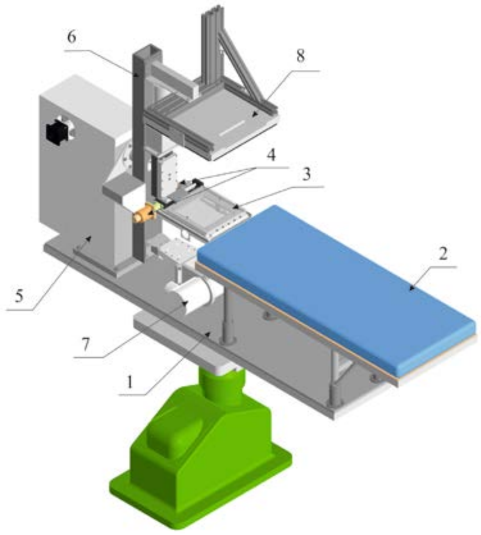

Fig. 2. Scheme of the installation of proton stereotaxic therapy: *1* – treatment table; *2* – treatment table deck; *3* – head fixation device; *4* – drives for movement of the deck of the HFD along the *X* and *Y* axes; *5* – HFD drive rack; *6* – rocker for rotation of the *X*-ray centralizer; *7* – *X*-ray monoblock; *8* – flat panel *X*-ray detector

The irradiation procedure begins with setting the initial position of the UPST: the HFD is set to –36°, the treatment table is set to –40° (depending on clinical requirements, other angles can be chosen). Simultaneously with switching on the beam, the movement of the UPST is started in accordance with the preset irradiation program. The HFD rotates from –36° to +36°, after which the treatment table rotates to a fixed angle, depending on the planned number of passes (for example, 8° for 10 passes). This cycle of movement corresponds to one pass. Then the second pass begins: the HFD makes a reverse movement from +36° to –36°, the treatment table again turns to a fixed angle, *etc*. (Fig. 3) until the irradiation program is completed.

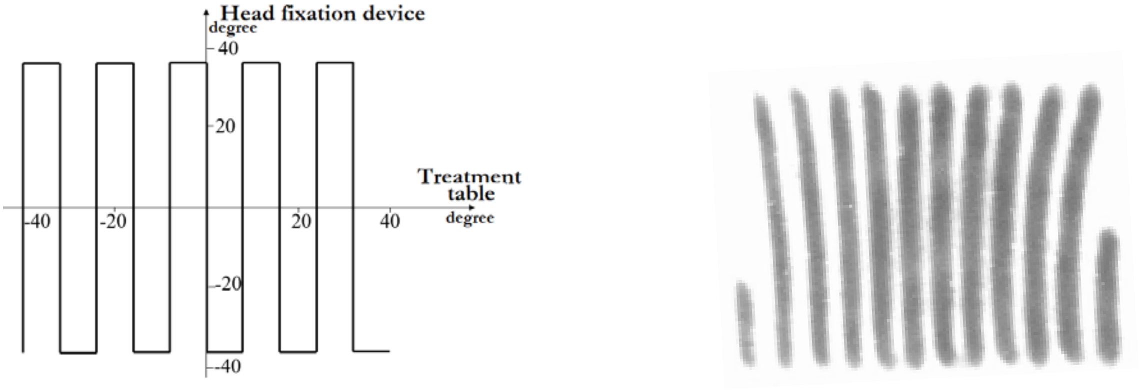

Fig. 3. Diagram of movement of the head fixation device and treatment table during 10 passes (*left*); radioautograph of a proton beam (*right*)

As a result, the beam describes a trajectory on the patient’s head, shown in Fig. 4. The concentration of the dose at the desired point occurs due to the following factors:

- Changing the direction of the patient irradiation by slowly turning it in two planes relative to the beam axis;
- Focusing of the proton beam by quadrupole magnetic lenses to the irradiation point;
- Small angular scattering of protons with an energy of 1 GeV in the patient’s body.

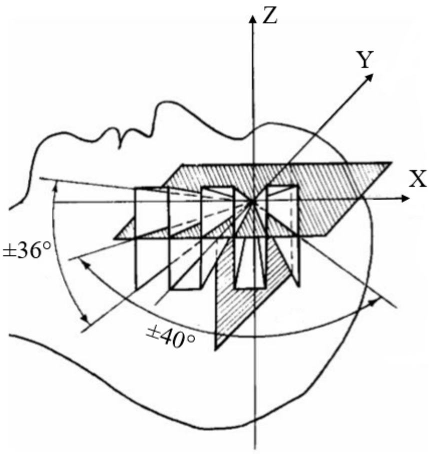

Fig. 4. Irradiation scheme. Direction of the proton beam passing through the centre of the target during stereotaxic irradiation using rotation of the stereotaxic proton therapy unit

Based on the results of clinical trials, it was found that the medical proton beam formed at the SC-1000 can be rationally used in the field of radioneurosurgery to affect small pathological areas of the brain (up to 2 cm) in order to destroy them. The main advantage of this method is the possibility of forming small dose fields with a high edge gradient, which makes it possible to concentrate the absorbed dose in the tumor with minimal radiation exposure of the surrounding tissues. Due to the high energy of the particles, the angular divergence of the 1 GeV proton beam is much smaller with the PBT than with the standard energy for PBT (using the Bragg peak), which simplifies the treatment planning. Using the gantry system is not provided due to the high energy of protons: guide magnets would be too heavy and cumbersome, so the technique of rotating the object of irradiation on a special installation is used.

The first full-scale dosimetric and radiobiological studies to analyse the effectiveness and at the same time the safety of using 1 GeV proton beam of the SC-1000 for radiation therapy, as well as to determine the scope of its application, were carried out back in 1971–1974. By 2013, the proportion of patients receiving proton therapy from the RSC RST–PNPI was approximately 2% of the global number of patients treated in the world. Using of proton stereotactic therapy (radiosurgery) proved to be effective in the treatment of various brain diseases, especially pituitary adenomas and cerebrovascular malformations, as well as in adenohypophysis irradiation for palliative purposes in breast and prostate cancer [3]. After 40 years of successful experience in treating patients, studies conducted in 2013–2017 led to the decision on the advisability of upgrading the stereotaxic proton therapy (radiosurgery) unit to meet modern requirements and world standards in radiation therapy, as well as for UPST registration as a medical device and the resumption of medical activities. The key stages of the modernization were: updating the material and technical base and software, including the replacement of the *X*-ray centering complex, updating the clinical dosimetry system, creating an automated control system for the UPST, a system for dose-anatomical planning and expanding methods for verifying of exposure plans.

3. Modernization of the medical proton complex

3.1. Replacement of the main elements of the X-ray centralizer

The *X*-ray centralizer is an integral part of the UPST, which is necessary to point the irradiation focus at the isocentre of the UPST. Previously, a TURDE-19 *X*-ray machine manufactured in 1982 was used with an electron-optical converter (EOC) and an *X*-ray television installation, on the monitor of which the resulting image was displayed. The issue of replacing the old *X*-ray centralizer with a more modern one is long overdue. The obsolescence of the equipment was considered the main obstacle to the beginning of the formalization of the complex as a medical device. The main parts of the *X*-ray centralizer (the *X*-ray emitter, the power supply and EOC) were replaced in 2018 with new equipment that meets modern requirements for *X*-ray studies. The EOC device was replaced with a digital flat panel detector DFP 4343 (Fig. 5). The size of the active area of the detector is 430 × 430 mm^2, the matrix resolution is 3 072 × 3 072, and the pixel size is 140 × 140 μm^2. For the new detector, a protective cover was made of plexiglass, and a radiopaque crosshair was applied, corresponding to the centre of the detector.

The updated *X*-ray centralizer based on a flat-panel detector surpasses the previously used one based on an image intensifier tube in most characteristics. The advantage is high spatial resolution, large dynamic range, high resistance to direct *X*-ray radiation, absence of spatial distortions and unevenness, insensitivity to magnetic fields, remote control, reduction of radiation exposure to staff. The high sensitivity of the flat panel detector makes it possible to obtain a high-quality image with a wide exposure range. In addition, it became possible to visualize small and low-contrast structures, which simplifies the procedure of laying the patient. Also, an automated workplace for the operator was organized to control the system and to work with the research results (Fig. 6). The digital format allows additional computer processing of the obtained images; the results of the study are stored in the system.

Fig. 5. *X*-ray centralizer in vertical position

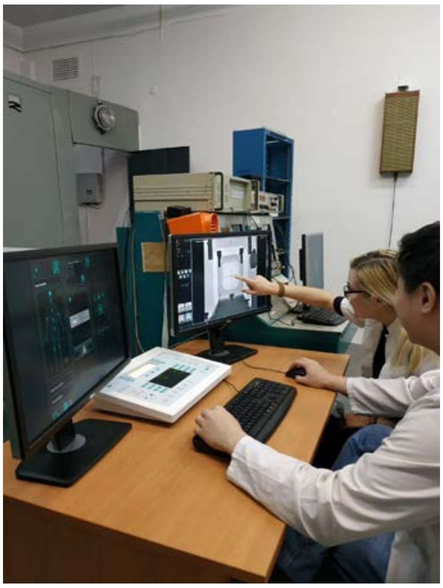

Fig. 6. Operator workstation

3.2. Update of the clinical dosimetry system

In 2018, the clinical dosimetry system was supplemented with a set of dosimetric equipment, which includes a Unidose$^{\text{webline}}$ PTW (Physikalish-Techische Werkstatten) Freiburg GmbH T10021 single-channel dosimeter with built-in firmware for absolute dosimetry of therapeutic and diagnostic beams and ultrasmall PinPoint ionization chambers of the type TM31014 (0.015 cm^3) and TM31015 (0.03 cm^3). This device is included in the register of Rosstandart. The dose measurement range is from 200 μGy to 450 MGy, the dose rate being from 1.2 mGy/min to 7.5 kGy/min simultaneously in three measurement ranges. The dosimeter has the ability to correct readings by entering various corrections. Multiplication by correction factors is done automatically by the instrument. The device is easy to use. Setting up, adding and changing the necessary parameters of the device and detector for the study is rather simple. The device can be controlled remotely with a local personal computer *via* the Internet using the virtual network computing program.

Measurements of the dose of a proton beam with an energy of 1 GeV during the verification of the new system (using Unidose$^{\text{webline}}$) were compared with the results of the existing equipment – thermoluminescence dosimetry (TLD) detectors. The analysis of the data showed that the difference in the dispensed dose does not exceed 5%, which indicates good agreement between the data. Figure 7 shows 2 Gy “dose binding” data using the chambers of clinical dosimeter Unidose$^{\text{webline}}$ and a comparison with the clinical dosimeter, type 27012, with hose ionization chamber, type 70107 (0.05 cm^3). As can be seen from the diagrams, the differences in the absorbed dose for beams 1 and 2 cm in diameter do not exceed 5%. The difference in the dose at a narrow beam with a diameter of 8 mm arises due to different active volumes of the compared ionization chambers.

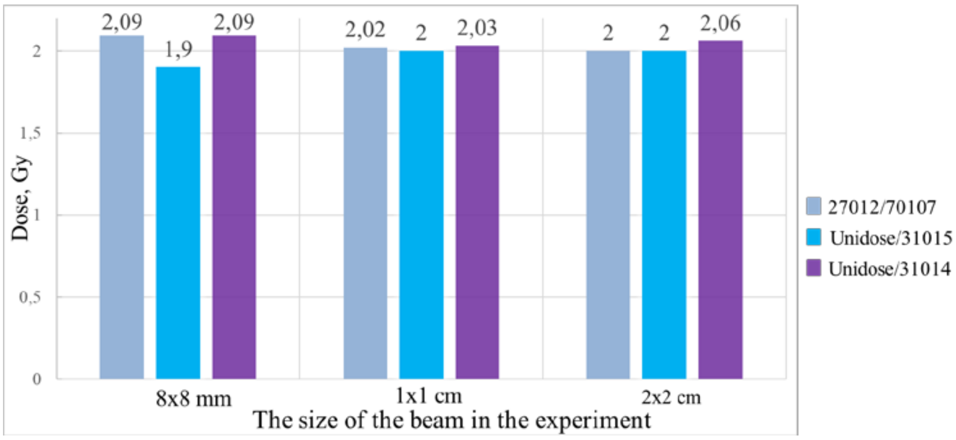

Fig. 7. Comparison of the “dose binding” using PTW Unidose$^{\text{webline}}$ and clinical dosimeter type 27012

3.3. Replacement of the control system, and equipment layout

The third-generation UPST control scheme was created back in 1989. Accordingly, the existing element base has become obsolete over the years and cannot meet the current requirements for ensuring the quality of the proton therapy. In 2014–2016, in order to improve the exploitative characteristics (speed of movement, positioning accuracy) of the electromechanical units and elements of the UPST, unipolar stepper motors were replaced with bipolar ones, which made it possible to significantly improve the dynamic characteristics of the moved units of the UPST and to use the mode of reducing the step of the motors during their movement, which improves the smoothness of movement. Magnetic-modulatory sensors of angular displacements were replaced by optical multidigit sensors “angle–code”. This measure makes it possible to significantly improve the displacement measurement result and the overall safety of the obtained results. The replacement of the equipment required the development of a new hardware and software (see below). Two types of drivers and a power source for controlling the operation of bipolar stepper motors, three two-channel adapter–coordinator–distributors and a manual control panel for electromechanical units of the UPST were developed and manufactured. In order to respond promptly to emergency situations, the control drivers were moved in 2018 from the irradiation room to the control room. On the whole, the synchronization of the system has been simplified: two workstations have been merged into one; the UPST is controlled by a single program, which also receives data from ionization chambers and profilometers.

3.4. Creation of an automated control program for the installation of proton stereotaxic therapy

The development of a program for the automated control of the UPST was required in connection with the replacement of the hardware for controlling the drives of the treatment unit. The first version of the control program “Proton Therapy”, intended to control the patient irradiation system, was developed in 2015. This program was used in conjunction with the previously developed “Profilometer” program, designed to display the data obtained using multiwire proportional chambers that measure the spatial characteristics of the beam online during irradiation. The program “Proton Therapy” had two drawbacks:

- The forced use in conjunction with the “Profilometer” program installed at another workstation, as a result of which it became necessary to involve at least two operators to monitor the irradiation process;
- The development of the program was stopped at the testing stage.

To expand the capabilities of the first version of the program of the control, it was decided to rework it at a new level and to combine it with the program for monitoring the parameters of the proton beam. So, in 2019 a software was created for controlling the UPST with the function of controlling the parameters of the proton beam [4]. The program is designed to automate proton therapy and provides the following modes of operation:

- Manual control of five axes of movement of the UPST;

- Output of information about the beam parameters: beam profiles (size, position), background, statistical parameters, intensity;
- Calculation of the monitor unit per absorbed dose unit;
- Setting exposure parameters or loading patient exposure plans;
- Conducting irradiation according to the given algorithm;
- The ability to interrupt and continue the irradiation process;
- Display of complete information about the course of the irradiation process in the form of 3*D* animation, graphs, tables;
- Generating reports;
- Formation of daily logs of actions of the program and operator, the ability to view the log for any date;
- Editing and storage of the parameters of the movement of the elements of the UPST, setting the parameters for registration of the proton beam.

The developed program has a flexible and understandable interface (Fig. 8). It allows one to manage the UPST in the manual mode as efficiently as possible and to receive complete information about the state of the installation. There is full control over the beam parameters and the possibility of linking to the dose ("dose binding"). The beam profiles are controlled directly in the control program, and not at a separate station. These additions have increased the work efficiency and led to a reduction in the time spent on the commissioning. The irradiation process has become more understandable in terms of visual component and information content, which contributes to the standardization of treatment protocols. The control of the irradiation process (beam profiles) has become automated.

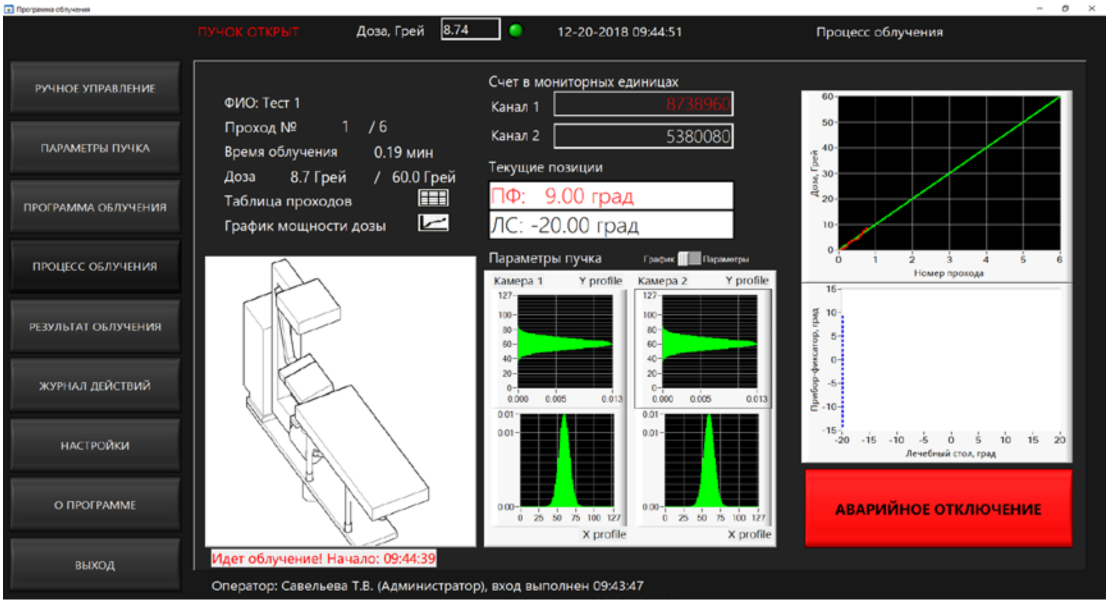

Доза, Грей 8.74

12-20-2018 09:44:51

ФИО: Тест 1
Проход № 1 / 6
Время облучения 0.19 мин
Доза 8.7 Грей / 60.0 Грей

Счет в мониторных единицах
Канал 1 8738960
Канал 2 5380080

Текущие позиции
ПФ: 9.00 град
ЛС: -20.00 град

Идет облучение! Начало: 09:44:39

Оператор: Савельева Т.В. (Администратор), вход выполнен 09:43:47

Fig. 8. Operating window of the stereotactic proton therapy unit control system

3.5. Development of a planning and verification system

A narrow proton beam with 1 GeV energy in combination with a stereotaxic irradiation method makes it possible to form strictly localized and concentrated dose fields. However, to realize this opportunity, it is necessary to carry out preliminary dose-anatomical planning of irradiation. At the first stage of proton therapy (1975–2013), irradiation planning was carried out manually according to experimental data. Dose distributions were obtained in a spherical phantom imitating the patient's head using TLD detectors, which were placed in the phantom in two mutually perpendicular planes with a step of 5 mm in the central region and 10 mm at the periphery. In this way, several tens of isodose maps were obtained and analysed for various irradiation parameters, which were combined into an atlas of dose distributions. As a rule, due to the limited shape and size of formations recommended for proton stereotaxic therapy with 1 GeV protons, the irradiation parameters in most cases did not change. The constructed isodose curves were plotted on a transparent film and superimposed on the magnetic resonance images of patients, performed in the frontal and sagittal planes, at the same scale. Then, the distance from the isocentre to the critical structures was determined. The measured distance was used to calculate the dose load on them. The areas of the target, and of the dose fields were calculated by simple arithmetic calculations. Manual scheduling is currently considered obsolete. Experimental data continue to be used, but only to verify the calculated dose distributions, and not as the main planning method.

The planning system and the verification system, along with the clinical dosimetry system, form the basis of radiotherapy quality assurance. The existing commercial software cannot be applied to the 1 GeV proton beam treatment method, since this method is unique and does not fit into the existing requirements. The work on the creation of a computerized treatment planning system (TPS) ProtoPlan, the algorithm for calculating the predicted dose of which is based on the Monte Carlo method with parameterization of integral properties, was started in 2018. The three-dimensional geometry of the TPS takes into account such features as:

- Energy of 1 GeV;
- Beam size of 6–10 mm at 50% isodose;
- Beam convergence and divergence;
- Lack of a gantry system;
- “On-through” irradiation;
- Change in linear energy transfer along the trajectory;
- Isocentric irradiation technique implemented with the help of the UPST;
- Scattering in the irradiated object;
- “Blurring: of the dose distribution due to secondary particles that are born in the process of interaction of protons with biological tissues.

Due to the uniqueness of the method of irradiation with 1 GeV protons, as well as the system of rotation of the irradiation area relative to the beam axis fixed in space, the main abilities of a non-standard proton therapy planning system became:

- Receiving data from diagnostic devices, support for the format of digital imaging and communications in medicine;
- Reconstruction of images from the original data set;
- Segmentation target volumes and organs of a risk;
- Calculation of the absorbed dose from a given beam and its presentation in the form of two- and three-dimensional isodose distributions superimposed on anatomical images (Fig. 9);
- Construction of “dose-volume” histograms for targets and critical organs;
- Export of the irradiation plan to the control program of the UPST.

One of the complex tasks of the formation of the modern concept of the MPC, along with the planning system, is the verification of the calculated exposure plans. The verification system is designed to compare the actual dose that the patient will receive with the dose calculated in the planning system. This stage of radiation therapy allows to be sure of the exact implementation of the radiation plan and additionally check the correct operation of the planning system for various radiation parameters. The dose distribution measured during the implementation of the verification plan (QA-plan) is compared with the calculated dose distribution using the γ-analysis method, which is currently the global standard. This method combines two criteria:

- Comparison of the percentage difference between the calculated and measured dose values;
- Comparison of the smallest distance from the measurement point to the isodose surface of the calculated dose value corresponding to the measured value.

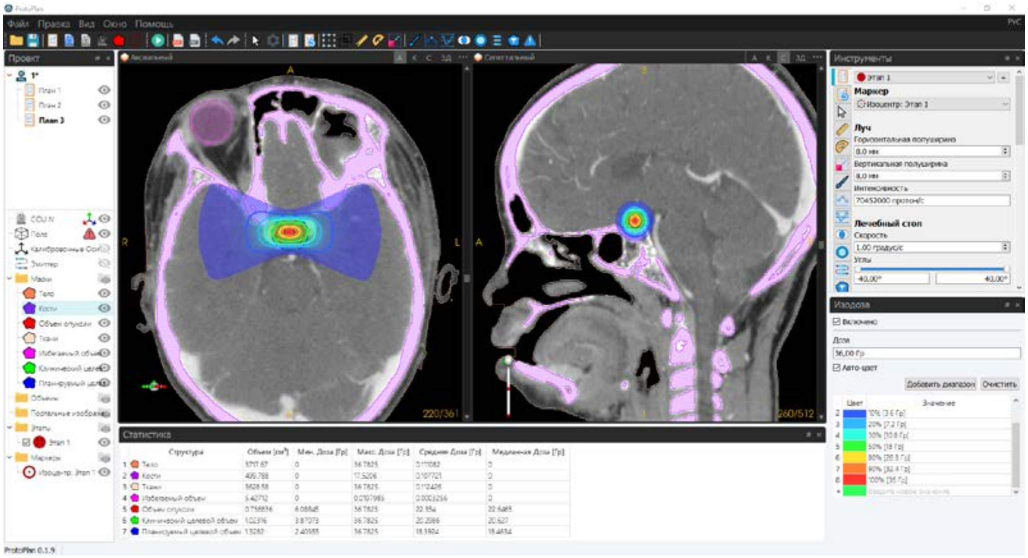

Этап 1
Маркер: Изоцентр: Этап 1
Луч
Горизонтальная полуширина: 8.0 мм
Вертикальная полуширина: 8.0 мм
Интенсивность: 70452000 протон/с
Лечебный стол
Скорость: 1.00 градус/с
Углы: -40.00° 40.00°
☑ Включено
Доза: 36,00 Гр
☑ Авто-цвет

	Цвет	Значение
2	🟦	10% [3.6 Гр]
3	🟦	20% [7.2 Гр]
4	🟦	30% [10.8 Гр]
5	🟩	50% [18 Гр]
6	🟨	80% [28.8 Гр]
7	🟧	90% [32.4 Гр]
8	🟥	100% [36 Гр]

Fig. 9. Isodose curves superimposed on magnetic resonance images of patients in the frontal (*left*) and sagittal (*right*) planes obtained in ProtoPlan

Currently, the work is underway to build up a dosimetric phantom for verification, and a possibility of using radiochromic films as detectors for relative dosimetry is being considered. As a result, the commissioning of a system of planning and verification will make it possible to proceed to the registration of the UPST as a medical device and the resumption of medical activities.

4. Conclusion

On April 17, 2023 it will be 48 years since the start of treatment of patients with proton therapy based on the synchrocyclotron SC-1000. There is no doubt that the unique method of proton radiosurgery for brain diseases using 1 GeV protons should be used with maximum efficiency. To resume proton therapy, it is necessary to obtain a registration certificate for the UPST as a medical device. To this end, a program was launched to modernize the equipment in order to bring the MPC in line with modern quality requirements, as well as to improve the reliability of therapy based on the SC-1000.

As part of the modernization, the main elements of the MPC have been replaced with more modern analogues, including: an *X*-ray centering system, a clinical dosimetry system, a control system, and technical tests of the updated systems were carried out. The last stage of modernization, which made it possible to proceed to the registration of the UPST as a medical device, was the development of a system for dose-anatomical planning and verification of exposure plans. This stage was performed in 2021. By the end of 2022, all planned engineering and technical works have been completed to bring the MPC to modern standards. The proton therapy based on SC-1000 can now be resumed.

References

1. Particle Therapy Co-Operativ Group. https://www.ptcog.ch
2. N.K. Abrosimov *et al*., J. Phys.: Conf. Ser. **41**, 424 (2006).
3. A.M. Granov *et al*., Vopr. Onkol. **59**, 465 (2013).
4. M.R. Kolkhidashvili *et al.*, Preprint NRC "Kurchatov Institute" – PNPI 3040, 11 (2019).